学位論文

Wave Characteristics of Electron Cyclotron Range of Frequency in Dipole Confined Plasmas

(ダイポール閉じ込めプラズマ中の電子サイクロトロン周波数帯波動の特性)

谷塚　英一

新領域創成科学研究科
先端エネルギー工学専攻
学籍番号　４７－６７２０４

平成 20 年 12 月 12 日

Acknowledgments

I would like to acknowledge to Prof. Yuichi Ogawa. He provided me the most worthful opportunities; of course they were experiments on the Mini-RT device. In addition he gave me a number of suggestions not only scientific things but also the behavior as a scientist. I thank Prof. Zensho Yoshida and Associate Prof. Masaru Furukawa. Their excellent attitudes of plasma physics excited me, especially their suggestions at the seminars were essential and valuable.

I appreciates Mr. Junji Morikawa and Dr. Haruhiko Saitoh. Mr. J. Morikawa always told me a number of the fundamental things of experiments, designing an apparatus, drawing drafts, safety of operation, and so on. Dr. H. Saitoh kindly helps our experimental group, and his techniques of experimental setups were valuable to learn. The author also thank Dr. Takuya Goto who told me about the Mini-RT device when I entered this group and about a lot of skills of a computer.

I want to express my acknowledgments to Mr. Daisuke Sakata and Mr. Hajime Kato who help my experiments and re-construction of Mini-RT when it removes from the Hongo campus to the Kashiwa campus. I cannot forget that we assembled the ECH system through the night into the morning. I would also like thank Mr. Kiyotake Kinjo, Mr. Shota Tanaka and Mr. Kenichiro Uchijima who collaborated my research, especially assemblies of diagnostic systems and numerical calculations.

My acknowledgment reaches to all members who belong to Prof. Y. Ogawa's, Prof. Z. Yoshida's and Associate Prof. M. Furukawa's laboratory. And I also want to thank staffs in the University of Tokyo, especially Mrs. Sunami Kojima and Mrs. Nami Tonegawa supported my daily life.

And I have been financially supported by the GCOE Office on Nuclear Education and Research Initiative. In addition, this office provided me a number of interesting opportunities for getting an overview of researches about the atomic energy. Moreover, I was financially

supported by this office when I had participated to international academic conferences at United States and Greece.

I would like to acknowledge to some private companies, Vega Technology Co., Ltd. and Sanyu Engineering Co., Ltd. This work could not be completed without their collaboration, the former one gave our group a lot of knowledges and skills of a microwave, the latter one helped the construction of diagnostic tools.

Finally, I would like to express my appreciation to Mr. Shiichiro Yatsuka, Mrs. Fujiko Yatsuka and Mr. Takumi Yatsuka for their long support.

Contents

Chapter 1

INTRODUCTION

1.1 Nuclear Fusion

1.1.1 Fusion as Atomic Energy

Nuclear fusion is one of the advanced methods for supplying electric power by using atomic energy. The most essential difference between fission and fusion is the nuclear reaction process. Fission is an atomic disintegration of heavy nucleus into light nucleus, e.g.

$$^{235}\mathrm{U} + \mathrm{n} \rightarrow ^{92}\mathrm{Kr} + ^{141}\mathrm{Ba} + 3\mathrm{n}. \tag{1.1}$$

On the other hand, fusion produces heavy nucleus from light nucleus, e.g.

$$\mathrm{D} + \mathrm{T} \rightarrow ^{4}\mathrm{He} + \mathrm{n}. \tag{1.2}$$

The common point of fission and fusion is a source of energy, i.e. a mass defect ($E = \Delta mc^2$), where E, Δm and c denote the produced energy, a total mass difference of before and after a nuclear reaction, and the light speed in vacuum, respectively. It is said fusion has a possibility of the dramatically reduction of high level nuclear wastes. In addition, fuels of a fusion power plant are very abundant, i.e. ocean water involves 33 mg/l of deuterium and 0.2 mg/l of lithium, and tritium can be produced from lithium and neutron.

$$^{6}\mathrm{Li} + \mathrm{n} \rightarrow \mathrm{T} + ^{4}\mathrm{He} + 4.8\mathrm{MeV}. \tag{1.3}$$

$$^{7}\mathrm{Li} + \mathrm{n} + 2.5\mathrm{MeV} \rightarrow \mathrm{T} + ^{4}\mathrm{He}. \tag{1.4}$$

Fusion reaction does not emit green-house effect gas, e.g. CO_2. Therefore, a fusion power plant seems to be an extremely promising method for an electric power supply. Furthermore

applications of fusion power for hydrogen production and so on have been considered [33]. However, fusion reaction needs to overcome the Coulomb potential, thus one should energize fuels, e.g. deuterium and tritium, sufficiently.

1.1.2 Reaction Cross Section

It is necessary for a fusion reaction to approach nucleus in the vicinity enough to work the nuclear force, i.e. ($\sim 10^{-14}$ m), for overcoming the Coulomb repulsive force. A probability of fusion reaction is the function of the kinetic energy of a relative motion of each nucleus. When a particle 1 collides with a particle 2, the rate of fusion reaction per unit volume N [$\mathrm{m^{-3}s^{-1}}$] is written as

$$N = n_1 n_2 \sigma v_{12}, \tag{1.5}$$

where n_1, n_2, σ and v_{12} denote densities of species 1 and 2, the reaction cross section and the relative velocity , respectively. Figure 1.1 shows kinetic energy dependence of fusion cross section σ [4][75][78].

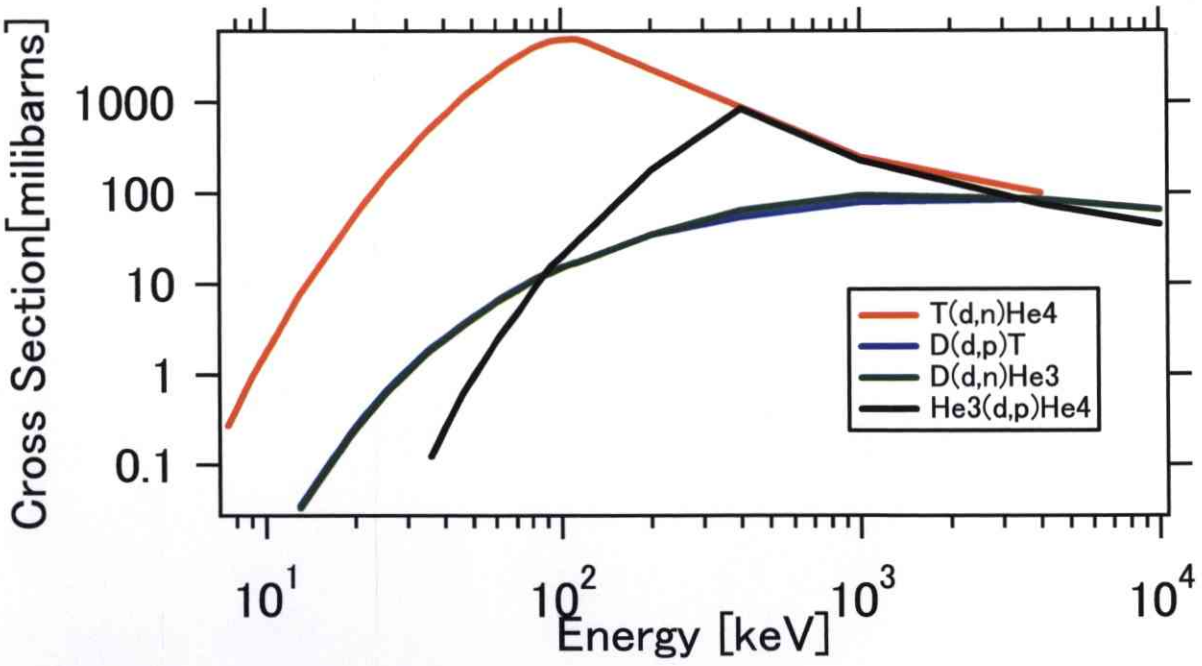

Figure 1.1: Fusion cross sections. The unit of cross section, i.e. millibarn, equals to $10^{-31}\mathrm{m}^{-3}$.

In order to use a fusion reaction as a power plant, the output energy of a fusion reaction must surpass input energy. For example, if we inject deuteron beam to tritium target, energy loss due to an ionization takes place. An ionization cross section can be evaluated to be $10^{-20}\mathrm{m}^2$, i.e. radii of atoms are of the order of 10^{-10} m. As shown in Fig. 1.1, cross sections of fusion reaction, i.e. $< 10^{-27\sim-29}\ \mathrm{m}^2$, are much smaller than that of an ionization. Therefore, fuels should be ionized beforehand, and one has to heat these charged particles, e.g. deuteriums, tritiums and electrons. These cloud of charged particles are referred to plasmas [21]. Moreover, one has to confine a plasma until fusion reaction has been completed.

J. D. Lawson evaluated the criterion for producing a thermonuclear reactor, so-called the Lawson criterion [38]. The plasma confinement time τ is defied as

$$P_L \equiv \frac{3n\kappa T}{\tau}, \tag{1.6}$$

where P_L, n, κ and T denote the energy loss per unit volume and unit time, a plasma density, the Boltzmann constant and plasma temperature, respectively. Energy loss by the Bremsstrahlung per unit volume and unit time is written as

$$P_B = 1.7 \times 10^{-38} Z^2 n^2 (\kappa T)^{1/2} \equiv \alpha Z^2 n^2 (\kappa T)^{1/2} \qquad [\mathrm{W/m^3}], \tag{1.7}$$

where Z denotes the atomic number of an ion [21]. Output power per unit volume from a fusion reactor is, for instance in the case of the D-T fusion,

$$P_T = \frac{n^2}{4} \langle \sigma v \rangle Q_T, \tag{1.8}$$

where σ, v and Q_T denote the D-T fusion cross section, an ion velocity and summation of output energies, i.e. the D-T fusion in a plasma and ^{6}Li-n reaction in a blanket, of 22.4 MeV. In addition, a bracket < > describes the average by a velocity. Let the efficiency of electric power generation be η, whence the electric energy output from a fusion reactor is written as

$$\eta \left(P_T + P_b + P_L \right), \tag{1.9}$$

thus, the Lawson criterion, i.e. balance of loss and output electric energies, is

$$\begin{aligned} P_b + P_L &= \eta \left(P_T + P_b + P_L \right) \\ \alpha n^2 T^{1/2} + \frac{3nT}{\tau} &= \eta \left(\alpha n^2 T^{1/2} + \frac{3nT}{\tau} + \frac{n^2}{4} \langle \sigma v \rangle Q_T \right) \\ n\tau &= \frac{3T}{\frac{\eta}{1-\eta} \frac{Q_T}{4} \langle \sigma v \rangle - \alpha T^{1/2}}. \end{aligned} \tag{1.10}$$

The Lawson criterion is the most fundamental indicator to achieve a fusion power plant. Another indicator is the ignition condition, i.e. balance of the alpha particle heating and loss,

$$P_b + P_L = P_\alpha = \frac{n^2}{4} \langle \sigma v \rangle Q_\alpha, \tag{1.11}$$

where Q_α =17.6 MeV. Equation (1.11) is equivalent to the Lawson criterion when η =0.136. Actual plant is expected to satisfy a condition which lies between the Lawson criterion and the ignition condition.

1.1.3 Types of the Concept of the Fusion Reactor

As mentioned in the previous section, in order to achieve a fusion power plant, Lawson criterion for low η should be satisfied. Two major approaches for achievement of it exist, one is the magnetic confinement and the other is the inertial confinement. Former one is oriented to confine relatively a low density plasma for a long time, whereas the latter one tries to confine extremely a high density plasma for a very short time, i.e. typical parameters of them are $n = 10^{20}$ m^{-3}, τ =1 s for the magnetic confinement and $n = 10^{31}$ m^{-3}, $\tau = 10^{-12}$ s for the inertial fusion.

Magnetic field restricts the motion of charged particles due to Lorentz force, i.e. charged particles receive a force, which is perpendicular to the magnetic field, therefore charged particles move helically around the magnetic field lines. However a plasma cannot be confined by a simple torus magnetic configuration; the guiding centers of electrons and ions drift in the counter direction, which is called ∇B drift and curvature drift, so that the charge separation in the vertical direction occurs, and it causes a radial drift, which is called $\mathbf{E}\times\mathbf{B}$ drift. Therefore a plasma is lost to the radial direction. Presently most progressed devices, such as tokamaks and sterallators, use twisted magnetic field lines to avoid the charge separation. On the other hand, this work treats a dipole magnetic field, like a planet, for the plasma confinement. In this type of configuration, a plasma is not orbitally lost owing to the charge separation because the directions ∇B and curvature drifts are toroidal direction, thus the charge separation does not occur because of the toroidally symmetric property. This configuration has the possibility of extremely high beta plasma confinement by the nature's way [41][88][25][32]. Details are mentioned in Chapter 2.

On the other hand, the concept of inertial confinement is simpler than that of magnetic confinement. Precisely, inertial confinement does not need to confine a plasma. The only

thing we should do is to focus laser beams on a fuel pellet, which is made of deuterium and tritium. Nevertheless, in order to obtain sufficient fusion gain, there are a lot of issues, e.g. the controlling of the waveform of laser pulses.

1.1.4 Issues for the Magnetic Confinement Fusion

Since the magnetic fusion needs a long ($\sim$1 s) energy confinement time, a complex magnetic configuration and high vacuum and so on, there are a lot of physical and technical issues [1][2]. Equilibrium and stability of core plasmas are crucial issues. Transport phenomena affect a plasma confinement, the low confinement to the high confinement (L-H) and the reverse ones (H-L) transition, Edge Localized Mode (ELM) physics, which determines the operation mode of a reactor. Understanding and suppression of disruption should be progressed to commercialize fusion reactors. Edge plasma property is very important because many chemical and physical interactions between an edge plasma and a divertor play important roles for core plasma property due to, for instance, high Z impurities. Physics of energetic ions, e.g. alpha particles, is an innovative and essential theme for ignition. Plasma heating and current drive are crucial to energize and confine a plasma. This work relates to the plasma heating by a radio frequency wave. Many technical issues, e.g. the tritium breeding, the withstanding strong neutron and X-ray from a plasma, fueling, should be also improved for achievement of a fusion reactor.

1.2 Difficulty of a High Beta Plasma Production and Heating

The beta value is defined as the ratio of a plasma pressure and a magnetic pressure

$$\beta = \frac{\sum_s n_s \kappa T_s}{\frac{B^2}{2\mu_0}}, \tag{1.12}$$

where subscript 's' denotes the species and κ is the Boltzmann constant. High beta means relatively high density and temperature plasma is confined by a weak magnetic field. Therefore coils can be small, and we can suppress cyclotron radiation from a plasma.

Recently high beta plasma studies have been carried out , for instance, Spherical Torus (ST), Field Reversed Configuration (FRC) and Reversed Field Pinch (RFP) and so on. Espe-

cially, in order to utilize the small aspect ratio property, heating without the Ohmic heating (center solenoid coil) is achieved [42]. The local absorption characteristic of a radio wave in a plasma allows local heating, local current drive. However the heating only by a radio wave has a difficulty due to the cutoff. The cutoff density is proportional to the square of the magnetic field strength, so that high beta plasma, i.e. plasma with weak magnetic field, cannot be heated by the conventional radio wave heating. On the other hand, radio wave heating and current drive without density limit, i.e. Electron Bernstein Wave heating and current drive, are actively investigated [15][37][20][62][72][58][26]. Electron Bernstein Wave heating and current drive are expected to be one of the most promising methods to heat and to drive a current for a high beta plasma or remarkably for a high density plasma.

1.3 Backgrounds of Researches on the Electron Bernstein Waves

Inserting antennas enables one to investigate waves in plasma directly. At the end of 1960's, various kinds of waves in linear and uniform plasmas were investigated [5]. Wavenumber is a good quantum number in the uniform plasmas, so that dispersion relations, i.e. the relation between angular frequency and wavenumber, were investigated to identify the waves excited in plasmas. P. J. Barrett *et al* investigated dispersion relations in the cylindrical plasma, and compared them with calculations of the dispersion relation [5]. Experimental data coincided accurately with the wide range of the density.

As well known and mentioned in the Sec. 3.2, the Electron Bernstein Wave (EBW) is an electrostatic mode, directly radio frequency electromagnetic field measurement is expected to provide information about EBW, which cannot be excited in vacuum, i.e. from outside the plasma. S. Gruber and G. Bekefi investigated longitudinal (electrostatic) waves in the linear device [23]. They observed the dramatically changing of wavelengths were observed when the magnetic field strength was increased. H. Sugai experimentally verified that a short-wavelength wave which was excited around the UHR was a mode-converted Electron Bernstein Wave [70]. Wavelengths satisfied the dispersion relation of an EBW, and the mode conversion efficiency approximately obeyed a theoretically predicted value [10]. Therefore, fundamental experiments showed existence of electrostatic EBWs in a plasma.

As mentioned in the Sec. 3.2, EBW is a backward wave, so that phase profile is expected

to provide important informations about an EBW excitation. The Ion Bernstein Wave has similar property, i.e. a backward wave [18][59]. M. Ono $et\ al$ showed the backward property of the IBW from the directions of a phase velocity and an energy flux [54]. F. Leuterer $et\ al$ identified EBWs from dispersion relation and directly measured the backward characteristic [14][39][40]. They obtained the direction of the phase velocity by steady injection experiments, and obtained the group velocity from the following two methods. First, they determined the group velocity from a dispersion relation, second they injected a very short pulse ($\sim$20 ns) microwaves and measured the direction of the propagation of a wave packet. Recently, such directly experiments were carried out on torus devices, e.g. the WEGA Stellarator [56][57]. They showed the mode conversion from the ordinary mode (O-mode) to extraordinary mode (X-mode) around a cut-off layer and the phase jump around UHR [68]. They carried out multi-component experiments in the WEGA stellarator, where the amplitude and the phase of ECRF electric and magnetic field were investigated with an rf-probe and ceramic-coated loop antennas. However, in their analyzing method, phase profiles were evaluated from Lissajous figures whose horizontal and vertical axis are channel and reference signals. Thus, the value of the phase is between 0 and π. A real phase behavior can be speculated physically, but the direction of the phase propagation cannot be distinguished.

On the other hands, there are a lot of works, in this decade, related to EBWs with the Electron Cyclotron Emission (ECE) diagnostic, which is an untouched diagnostic method. P. C. Efthimion $et\ al$ proposed the method to investigate EBWs with ECE diagnostics [16]. This is one of the most popular methods of the evaluation of the mode-conversion efficiency experimentally [74][35][55][66]. By using this method, B. Jones, et al. verified the almost complete conversion efficiency in the CDX-U device [27]. Therefore, the EBW heating and current drive are recently considered as a crucial method of heating and current drive, especially at high density plasma in helical devices and at high beta plasma such as spherical tori. In these devices the detection of the mode-converted EBWs in a plasma is tried by using ECE diagnostics, which enable the evaluation of mode-conversion from outside plasmas.

1.4 Outline of This Research

This work is concerned with waves in a dipole confined plasma, e.g. plasma production by an Electron Cyclotron Heating (ECH), the heating property and direct diagnostics of the Electron Cyclotron Range of Frequency (ECRF) electric field. Chapter 2 describes concepts of the dipole confinement and mentions about Mini-RT. Chapter 3 provides the theoretical basis of waves in plasmas, which are especially focused on the Electron Bernstein Wave (EBW). Chapter 4 shows experimental setups, that contains plasma production, density and temperature measurements. Calibration and mutual comparison among diagnostic systems are also mentioned in this chapter. Chapter 5 denotes the heating property in Mini-RT that means density and temperature profile, effect of the levitation of the internal coil and the magnetic configurations. Chapter 6 describes the development of the ECRF electric and magnetic field measurement system. Chapter 7 describes the experimental results of ECRF electric and magnetic field measurements. In addition, the discrepancies between experiments and theories are discussed. Finally, conclusions are summarized in Chap. 8.

Chapter 2

Dipole Confined Plasmas

2.1 Background and Motivation

High beta plasmas were observed around the Jovian magnetosphere by a planetary exploration satellite Voyager [34]. The plasma density in the Jovian magnetosphere is around $10^2 - 10^3 \mathrm{m}^{-3}$, and the ion and electron temperature is around 30 keV. The magnetic field strengths are 10 nT at $r \sim 50 R_j$ and 4 nT at $r \sim 100 R_j$, then they correspond $\beta \sim 0.1 - 0.2$ and $\beta > 0.5$, respectively.

Although space plasmas are not controlled, they are not relaxed to the state of maximum entropy. As well known, irreversible variation in an adiabatic system increases the entropy of this system. This principle is so-called the second law of thermodynamics. If a plasma reaches the maximum entropy state, density and temperature may be uniform. However an actual plasma has its own structure, thus one should consider that there is another relaxed state. A restriction enables a system to relax to a state that is different from the simple maximum entropy state. This is dealt with a variational principle with restrictions. D. Montgomery *et al* proposed a statistical theory of an organized state of the maximum entropy state with restrictions of the magnetic energy and the magnetic helicity [45].

A famous example of self-organization of an experimental plasma is force-free configuration (Taylor state or single Beltrami state). Taylor state is described as a minimum energy state with conservation of the magnetic helicity [73]. The magnetic helicity is defined as

$$K \equiv \int \mathbf{A} \cdot \mathbf{B} \mathrm{d}^3 x, \tag{2.1}$$

where $\mathbf{A}$ and $\mathbf{B}$ denote the vector potential and the magnetic field strength, respectively. Let

the Lagrange multiplier be μ, the variation of the magnetic field energy should be zero,

$$\delta(E - \mu K) = 0, \tag{2.2}$$

where $E = \int B^2 \mathrm{d}^3x$, and the magnetic field is normalized appropriately. Then

$$\nabla \times \mathbf{B} = \mu \mathbf{B} \tag{2.3}$$

is obtained, and this is so-called a force-free condition.

In addition, a flowing plasma relax to the minimum energy state with conservation of magnetic and generalized helicity (Double Beltrami state). This is an extended Taylor state; recently, S. M. Mahajan and Z. Yoshida have developed a relaxation theory of flowing plasma, which predicts a possibility of an extremely high beta plasma confinement (see Fig. 2.1) [41][88]. If this is achieved, one may be able to realize an advanced fusion reactor like a D $-^3$ He one.

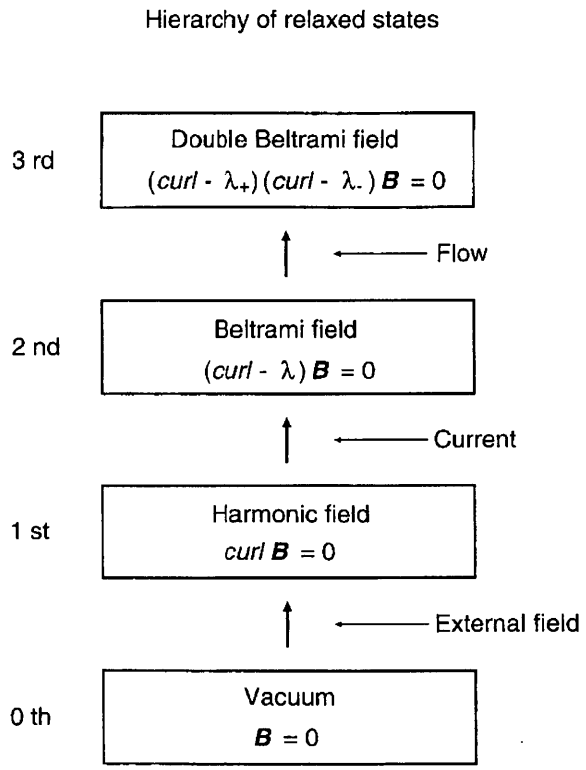

Figure 2.1: Hierarchy of relaxed states. The absolute minimum energy state is the vacuum. In supplying a magnetic field, current and flow to the plasma, the energy of the system rises successively with the harmonic, the first and the second Beltrami fields [87].

2.2 Two Fluids Relaxation Theory

In this section, two fluid magnetohydrodynamics (MHD) is described and the Beltrami/Bernoulli condition is derived. The fluid equation of the motion of electrons is

$$m_e n_e \frac{\mathrm{d}\mathbf{v}_e}{\mathrm{d}t} = -en_e(\mathbf{E} + \mathbf{v}_e \times \mathbf{B}) - \nabla p_e, \tag{2.4}$$

where m_e, n_e, $\mathbf{v}_e$, e, $\mathbf{E}$, $\mathbf{B}$ and p_e denote the electron mass, an electron density, an electron velocity, the elemental charge, an electric field, a magnetic field and an electron pressure, respectively. Here one can neglect an electron inertia, so that

$$\mathbf{E} + \mathbf{v}_e \times \mathbf{B} = -\frac{1}{en_e}\nabla p_e. \tag{2.5}$$

Similarly ion's one is

$$m_i n_i (\frac{\partial \mathbf{v}_i}{\partial t} + \mathbf{v}_i \cdot \nabla \mathbf{v}_i) = en_i(\mathbf{E} + \mathbf{v}_i \times \mathbf{B}) - \nabla p_i, \tag{2.6}$$

where valuables ,e.g. mass, are replaced from electron's to ion's ones, moreover the convection term can be represented as

$$\mathbf{v}_i \cdot \nabla \mathbf{v}_i = \frac{1}{2}\nabla v_i^2 - \mathbf{v}_i \times (\nabla \times \mathbf{v}_i), \tag{2.7}$$

then Eq. (2.6) can be written as follows:

$$\frac{\partial \mathbf{v}_i}{\partial t} - \frac{e}{m_i}\mathbf{E} - \mathbf{v}_i \times \left(\frac{e}{m_i}\mathbf{B} + \nabla \times \mathbf{v}_i\right) = -\frac{1}{m_i n_i}\nabla\left(p_i + \frac{m_i n_i v_i^2}{2}\right). \tag{2.8}$$

Let length, time, magnetic field and pressure be normalized by the ion skin depth $\lambda_i \left(= \frac{c}{\omega_{pi}} = \frac{V_A}{\Omega_i}\right)$, an ion cyclotron frequency $\Omega_i = \left(\frac{eB}{m_i}\right)$, typical magnetic filed strength B_0 and $p = \frac{B^2}{2\mu_0}\hat{p}$, respectively. Then electric scalar potential and velocity are normalized by $\phi = \frac{m_i V_A^2}{e}\hat{\phi}$ and $\mathbf{v} = V_A\hat{\mathbf{V}}$, respectively, where V_A, V_T and n_0 denote the Alfvén velocity, a thermal velocity and a typical density, respectively. By using the following relationships $\mathbf{E} = -\frac{\partial \mathbf{A}}{\partial t} - \nabla\phi$, $\mathbf{v}_i \sim \mathbf{v}$, $\mathbf{v}_e = \mathbf{v} - \frac{\mathbf{j}}{en}$ and $\mathbf{j} = \mu_0^{-1}\nabla \times \mathbf{B}$, Eqs. (2.5) and (2.8) are normalized as

$$\frac{\partial \mathbf{A}}{\partial t} - (\mathbf{v} - \nabla \times \mathbf{B}) \times \mathbf{B} = \nabla\left(\frac{1}{2}p_e - \phi\right) \tag{2.9}$$

$$\frac{\partial(\mathbf{A} + \mathbf{v})}{\partial t} - \mathbf{v} \times (\mathbf{B} + \nabla \times \mathbf{v}) = -\nabla\left(\frac{1}{2}v^2 + \frac{1}{2}p_i + \phi\right), \tag{2.10}$$

where A denotes the vector potential.

Moreover, minimization of an energy with restraints of the magnetic helicity and the generalized helicity lead to the double Beltrami state. The magnetic and the generalized helicity are defined as

$$\frac{1}{2}\int \mathrm{d}^3x \mathbf{A}\cdot\mathbf{B}, \tag{2.11}$$

$$\frac{1}{2}\int \mathrm{d}^3x (\mathbf{A}+\mathbf{v})\cdot(\mathbf{B}+\nabla\times\mathbf{v}), \tag{2.12}$$

respectively. Then double Beltrami state is written as follows

$$\mathbf{B} = a(\mathbf{v}-\nabla\times\mathbf{B}), \tag{2.13}$$

$$(\mathbf{B}+\nabla\times\mathbf{v}) = b\mathbf{v}, \tag{2.14}$$

where a and b are constants. As the result, Eqs. (2.9) and (2.10) can be written as

$$\frac{1}{2}p_e - \phi = \mathrm{Const.}, \tag{2.15}$$

$$\frac{1}{2}v^2 + \frac{1}{2}p_i + \phi = \mathrm{Const.}. \tag{2.16}$$

By summing these two equations, following relationship is obtained

$$v^2 + \beta = \mathrm{Const.}, \tag{2.17}$$

where β is defined in Eq. (1.12). Therefore one can realize a Alfvénic flow enables one to confine a plasma whose beta value is of the order of unity.

2.3 Procedures and Issues

The goal of the ring trap (RT) project is to verify high beta plasma confinement in an experimental device with Alfvénic flow. Figure 2.2 shows the brief summary of the procedures of the ring trap project. In Proto-RT, fundamental physics of a dipole confined plasma, e.g. driving flow by biasing internal coil [49] and formation of electric field structure of electron plasma [63] were investigated. The principle of the levitation of the coil was verified on FB-RT (Feed Back Ring Trap) experimentally [46]. The pull-up method has been adopted for the levitation. Feed back controlling of the levitation coil enables one to levitate magnets stably. In Mini-RT, a number of engineering issues have been verified for constructing a relatively large dipole plasma experimental device RT-1, especially cooling of the superconducting coil and

excitation of a persistent current are crucial ones [51][43][80][81][47]. The RT-1 device has already been constructed for investigating the possibility of high beta plasma confinement [89]. High beta plasmas with the order of 10% were experimentally obserbed and it is considered due to high energy electrons which are produced by the electron cyclotron heating [90].

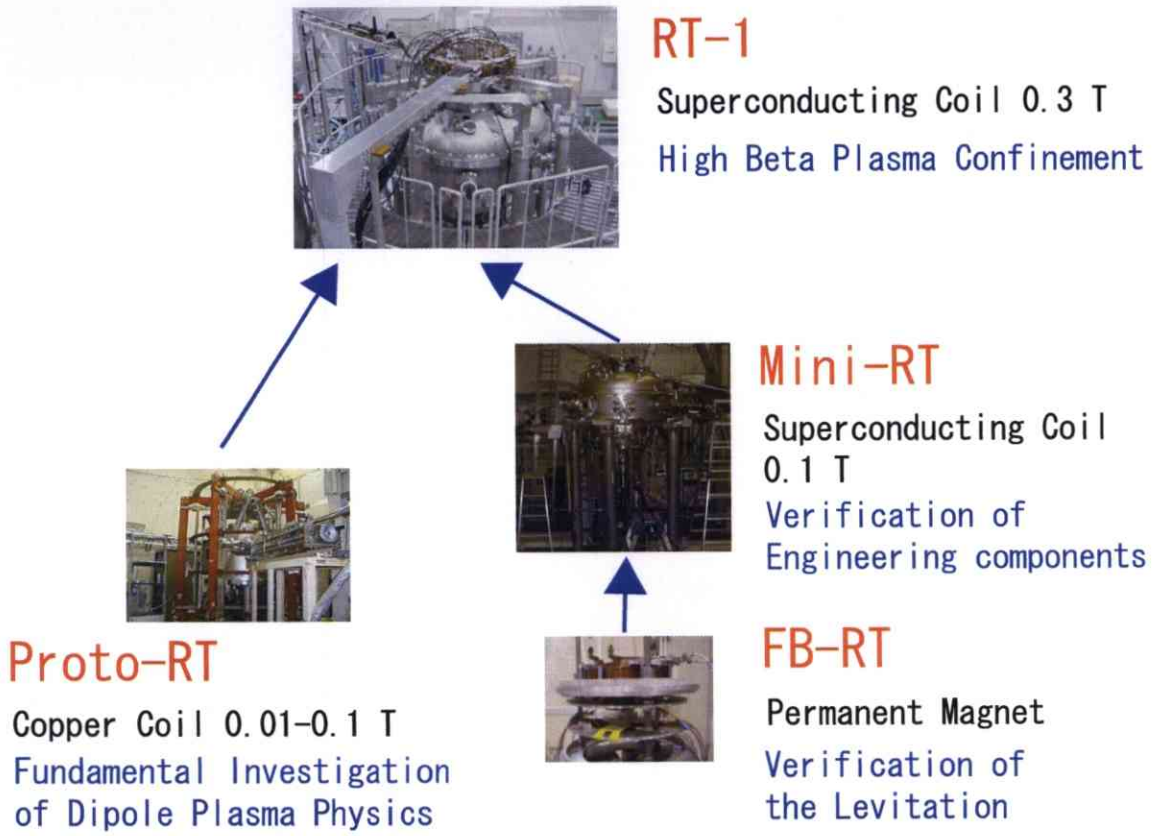

Figure 2.2: The procedures of Ring Trap (RT) project.

2.4 The Mini-RT Device

2.4.1 Overview of the Mini-RT Device

The Mini-RT device is an internal coil device that has High Temperature Superconducting (HTS) coil [50]. Figure 2.3 shows the cross sectional view of Mini-RT. The specifications of vacuum vessel and coils are shown in Table 2.1 and 2.2, respectively. The internal coil,which generate a magnetic field for a plasma confinement, is the main coil in this device. It is made of high temperature superconductor, i.e. Bi-2223 tape, and has 150 and 210 mm of a major and outer radius of the coil shell, respectively, and has 16.8 kg of total weight. It is cooled and

charged a persistent current at the bottom of the vacuum vessel. After that it is moved to the mid-plane by three mechanical support legs, and can be levitated by applying the levitation coil current. The levitation coil, which controls the vertical location of the internal coil, lies at the top of (and outside) the vacuum vessel. It is made from copper and be water-cooled. The pull-up method is adopted for the magnetically levitation method. Construction of the saddle coils is planned for the robust controlling of the tilting of the internal coil. Actually this plan has verified experimentally in the FB-RT [28]. In addition, construction of the vertical (Helmholtz) coils is planned for the controlling of a plasma confinement region. Currently this role is partially played by the levitation coil, i.e. it is possible to control a plasma confinement region by the levitation coil current (the location of the separatrix) if the internal coil is not levitated. Construction of toroidal coils are planed for applying a magnetic shear. It is expected that one can investigate the effects of it for the transport phenomena. Two turbo-molecular pumps with 350 litter/s are used for vacuuming; hereby a typical base pressure is 1.0×10^{-5} Pa. The working gases are hydrogen or helium, and their pressure is controlled by a valve.

Table 2.1: Specification of vacuum vessel of Mini-RT

Diameter	1.0m
Height	0.7m
Base Pressure	1.0×10^{-5}Pa

2.4.2 Internal Coil

For the material of the wire rod of the internal coil on the Mini-RT device, Bi-2223 tape was adopted. The reason why this material was adopted was as follows.

- A low temperature superconductor (LTS) needs cooling by liquid helium, whereas a high temperature superconductor (HTS) can be used with several 10 K of a temperature.
- Thermal likelihood of an HTS is larger than that of an LTS.
- Workability of the Bi-2223 is better than that of the YBCO.

However, there are some demerits of an HTS. Current density of an HTS is lower than that of an LTS, and an HTS is more expensive than an LTS.

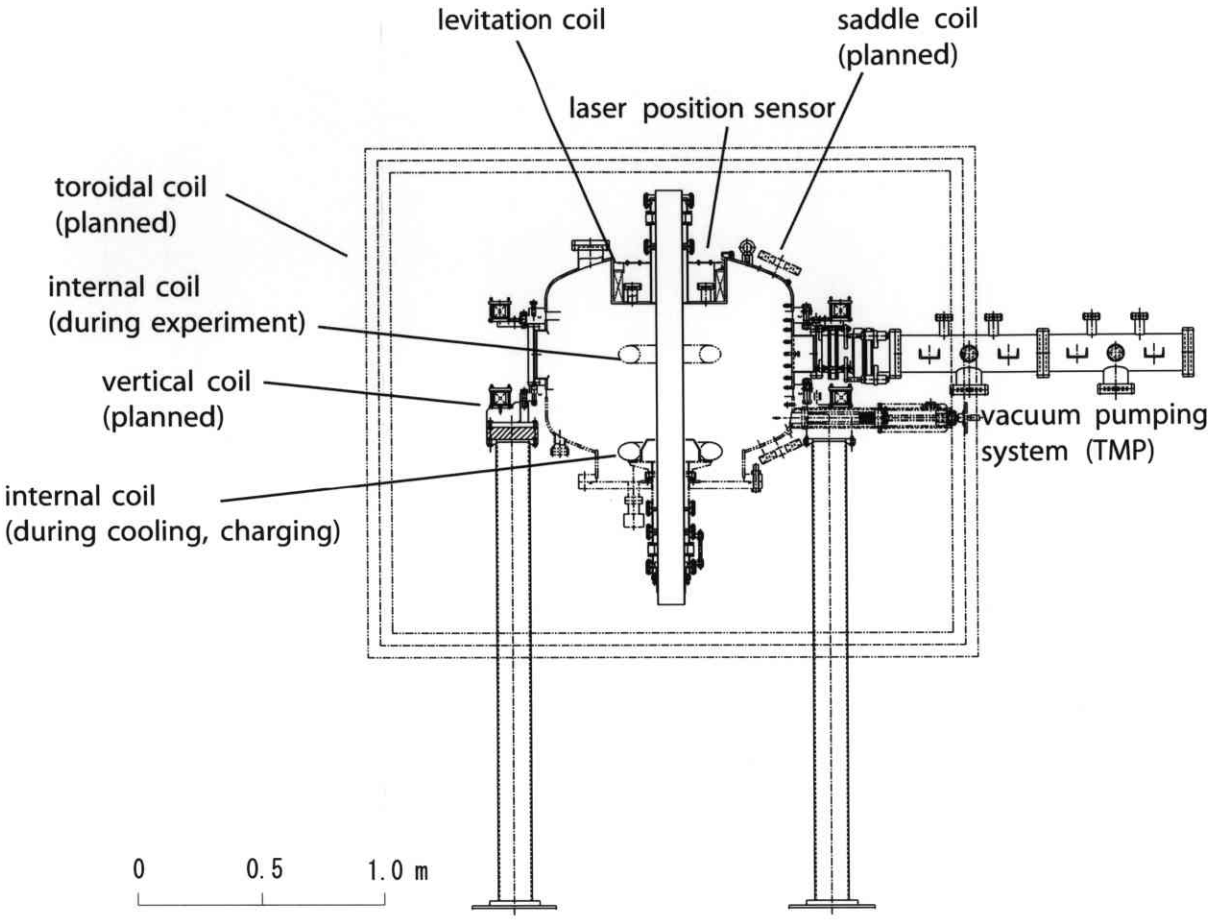

Figure 2.3: The cross section of the Mini-RT device.

Since an HTS coil does not need the cooling by liquid helium, the direct cooling by helium gas was adopted for cooling an HTS coil on Mini-RT. Cooling by a helium gas needs shorter time than that by a thermal conduction. It is hard for the thermal conduction method to balance cooling and the thermal insulation. A direct cooling method needs detachable transfer tubes and a seal construction to avoid a leak of helium gas into the vacuum vessel from an inlet of a transfer tube.

A direct charging method by using a persistent current switch (PCS) was adopted on Mini-RT. The induction charging needs an induction coil with more than 100 kA of current and a large power supply of an induction coil to charge the 50 kA of current to the internal coil, whereas the direct charging method needs less than a power supply with 2 kW. In addition, direct charging method needs detachable current lead.

Figures 2.4 and 2.5 show the cross section and top view of the internal coil, respectively.

Table 2.2: Specification of coils

Internal Coil (F-Coil)	
Material	Bi-2223 tape
Major Radius	150mm
Outer Radius of Coil Shell	210mm
Inner Radius of Coil Shell	122mm
Turn Number	428
Total Current	50kA
Total Weight	16.8kg
Inductance	0.0876H
Stored Energy	598J
Levitation Coil (L-Coil)	
Material	Copper(water-cooled)
Major Radius	208.75mm
Turn Number	68
Total Current	27kA

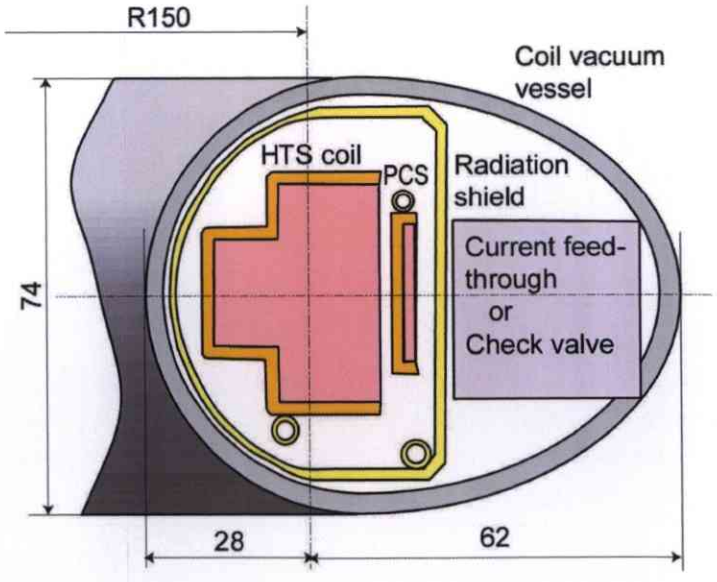

Figure 2.4: Cross section of the internal coil.

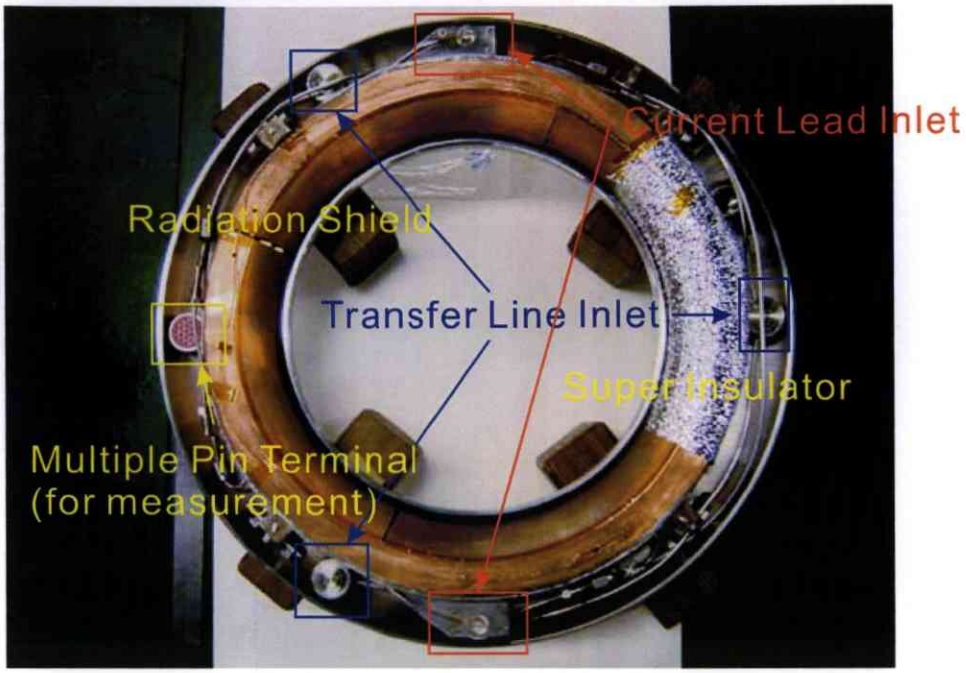

Figure 2.5: Top view of the internal coil.

An HTS coil and a PCS are covered with a Copper radiation shield. An HTS coil is supported by the five folded tubes to decrease the thermal load into the radiation shield by keeping distance between the shell of the internal coil and the radiation shield. Structure and a photograph of a five folded tube is shown in Fig. 2.6.

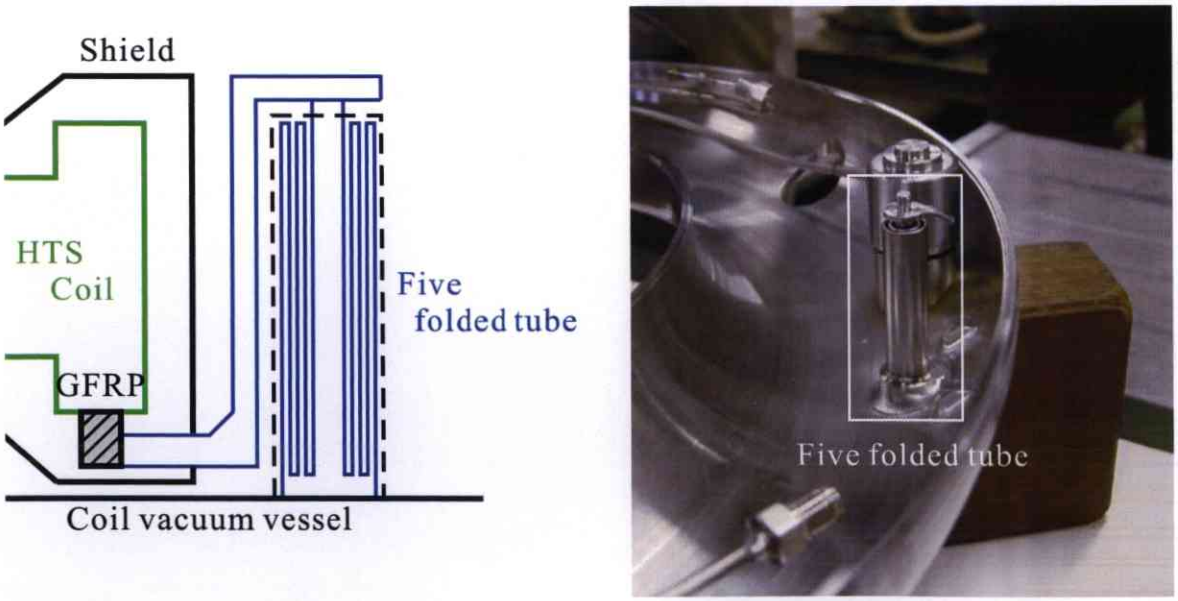

Figure 2.6: Structure and a photograph of a five folded tube.

2.4.3 Cooling System of the Internal Coil

The cooling system of the internal coil in Mini-RT is shown in Fig.2.7. Two GM refrigerators are used for the cooling of helium gas. The cooled helium gas is compressed to 1 MPa and fed to the internal coil through a transfer tube. Since it is necessary to control temperatures of an HTS coil and a PCS independently, there are two recovery transfer tubes.

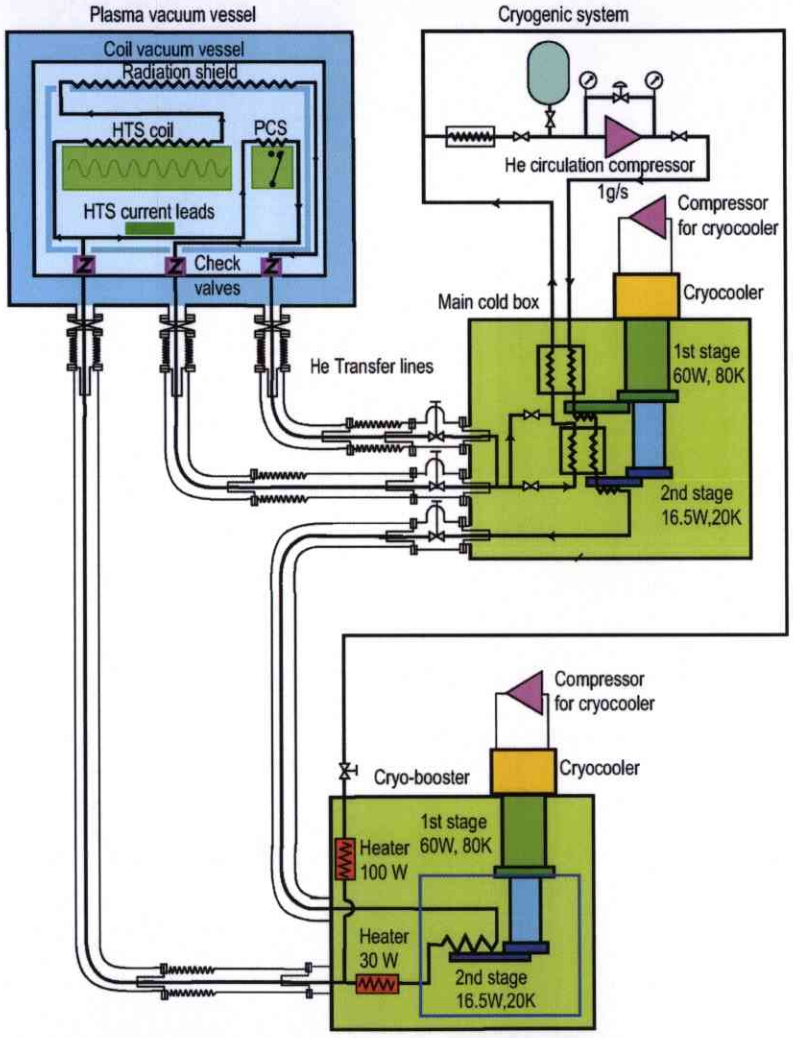

Figure 2.7: Internal coil cooling system on the Mini-RT device.

The head of transfer tube is shown in Fig.2.8. Projection from the center of transfer tube head opens check valve, whose diameter is 30 mm. Six holes are the paths of the helium gas flow, and right outside of it is Kel-F packing that hardly shrink to avoid leak of helium gas into the vacuum vessel. Fastening the screw at the edge of a transfer tube head applies pressure at the seal section and this screw fixes a transfer tube to the internal coil mechanically.

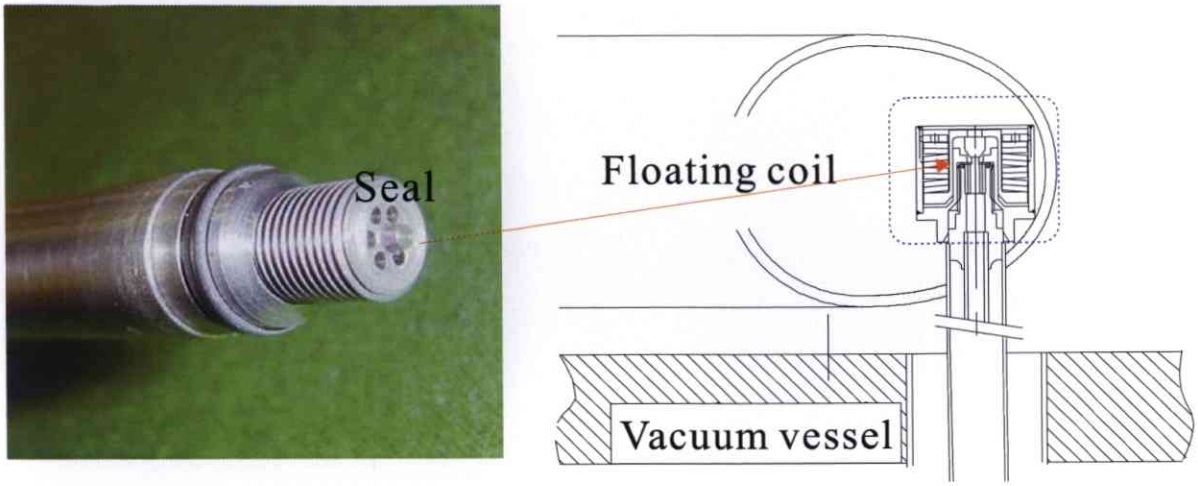

Figure 2.8: Photograph and a drawing of a detachable transfer tube.

2.4.4 Excitation of a Persistent Current in Mini-RT

The schematic view of the charging system is shown in Fig.2.9. The charging sequence is as follows.

1. Connect the current leads for applying a current to the HTS coil and a PCS heater.
2. Heat the PCS to ~130 K by using a PCS heater (0.8A, 140V). After that, the PCS is not a superconducting state.
3. Apply a current to the HTS coil.
4. Cool down the PCS. Then the PCS is also a superconducting state.
5. Decrease an applying current. Then the magnetic flux conservation leads to switching a current from the HTS coil power supply into the PCS.

Figure 2.10 shows the current feed-through, which is made from copper electrode, on the Mini-RT device. In order to reduce the penetration of a heat from the current leads to the superconducting coil, liquid nitrogen is used for the cooling of the electrodes. This made us increase the superconducting current from around 50 A to 120 A (maximum) without quenching of a crossover cable, which is made from a gold.

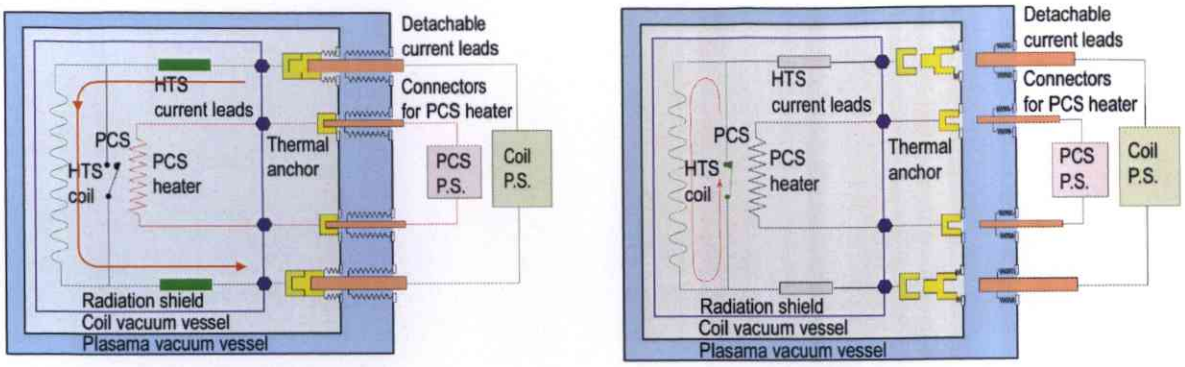

Figure 2.9: Schematic view of the charging system.

Figure 2.10: Photograph of the head of a detachable current lead.

2.4.5 Levitation Control of the Internal Coil

After the excitation, the floating coil is lifted up to the mid-plane by three mechanical legs, and be levitated by the feed back of the levitation coil current. The height of the internal coil is detected by three laser distance sensors (Keyence LK-500 (sensor head), LK-2500 (amplifier unit)). Obviously, a rigid body has 6 degrees of freedom as shown in Fig. 2.11. If we need to control tilting and sliding motions, saddle coils are necessary. The rotational motion cannot be controlled; however, it is not severe for producing the dipole magnetic field because of its axisymmetric characteristic.

As mentioned above, the pull-up method was adopted for the levitation of the internal coil on Mini-RT. Figure 2.12 shows the measurement method of the height of the internal coil. There are three laser position sensors, so that the height and the tilting can be measured by

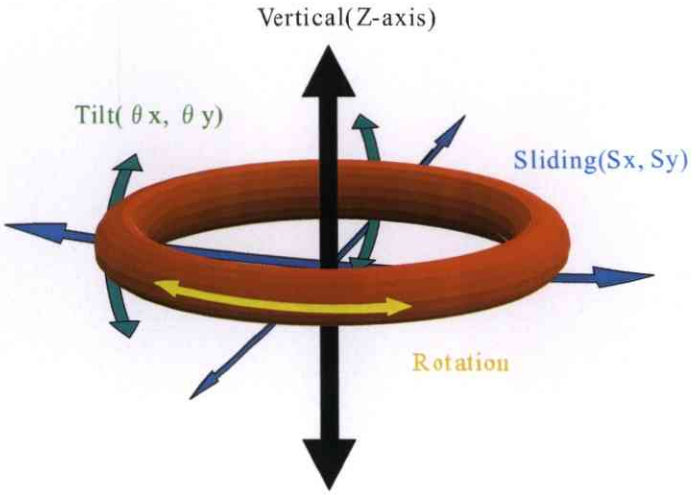

Figure 2.11: Degrees of freedom of the internal coil.

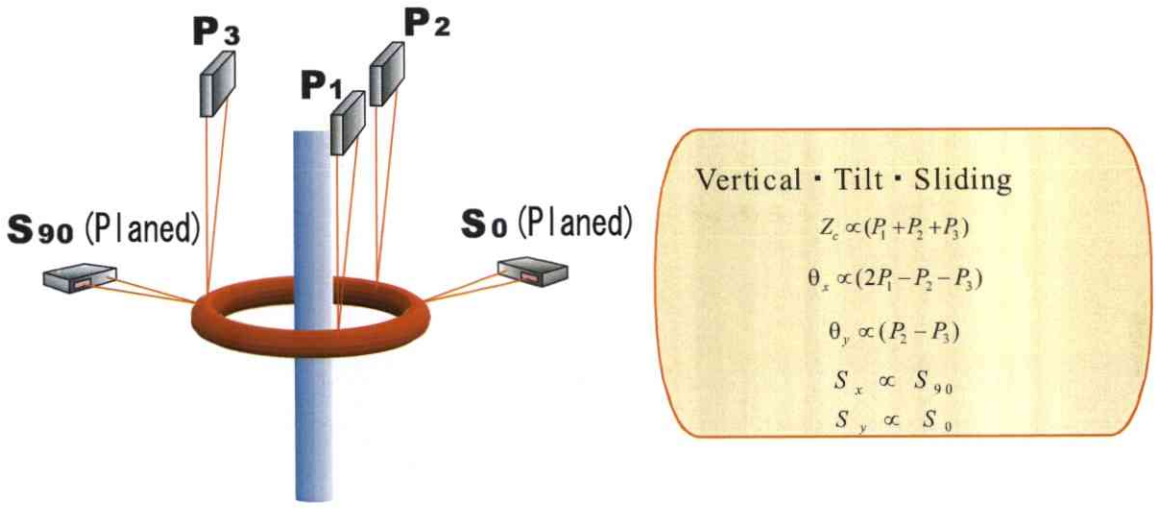

Figure 2.12: Measurement method of the height of the internal coil on Mini-RT.

the present system. Planned two sensors which measure the height of the internal coil from two horizontal directions will measure the sliding of the internal coil. Figure 2.13 shows the top of the vacuum vessel of Mini-RT at which components of levitation is collected.

The tilting stability was discussed and the result is shown in Fig. 2.14. The internal coil does not tilt by the magnetic field itself. Thus the tilting is determined only by the geometry of the magnetic field created by the levitation coil. The ratio of the radii of the levitation coil and the internal coil determines the geometry at the surface of the internal coil. In Fig. 2.14, the radius of the levitation coil and coordinates of it are normalized by the radius of the internal coil. On Mini-RT device, the levitation coil lies around the boundary between the stable and unstable regions.

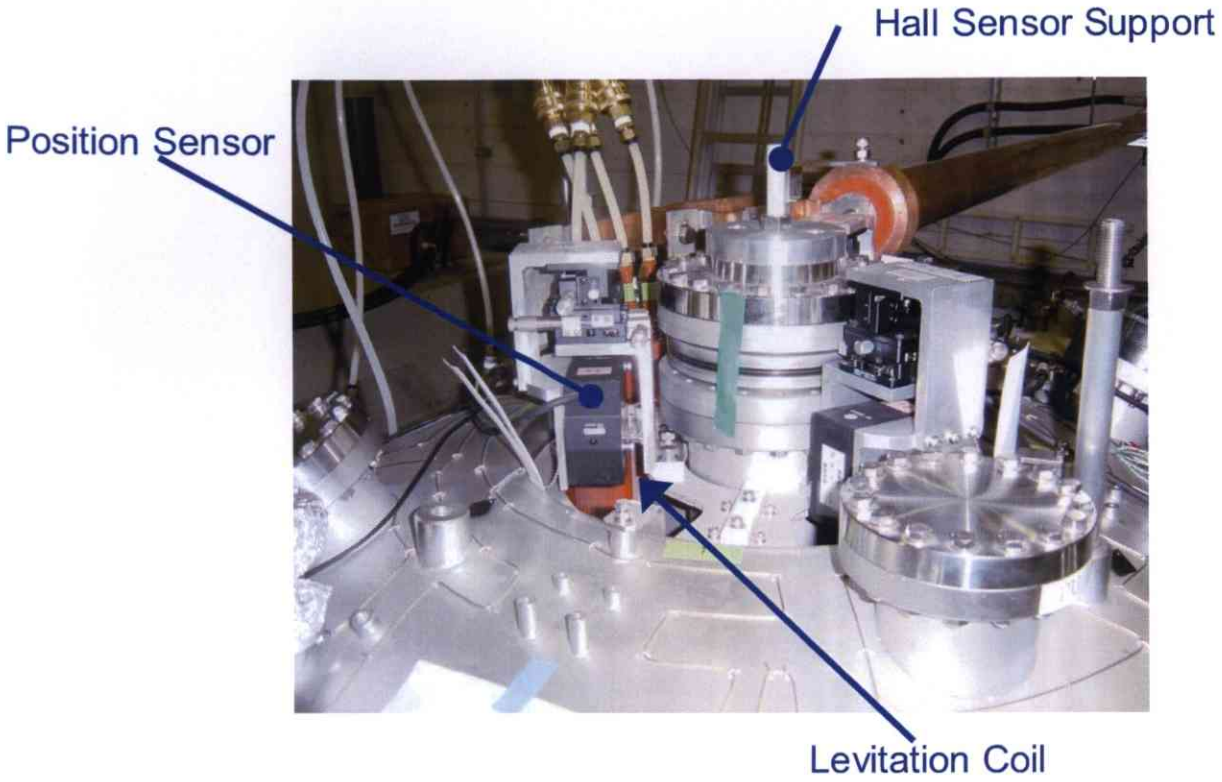

Figure 2.13: Photograph of the top of vacuum vessel of the Mini-RT device.

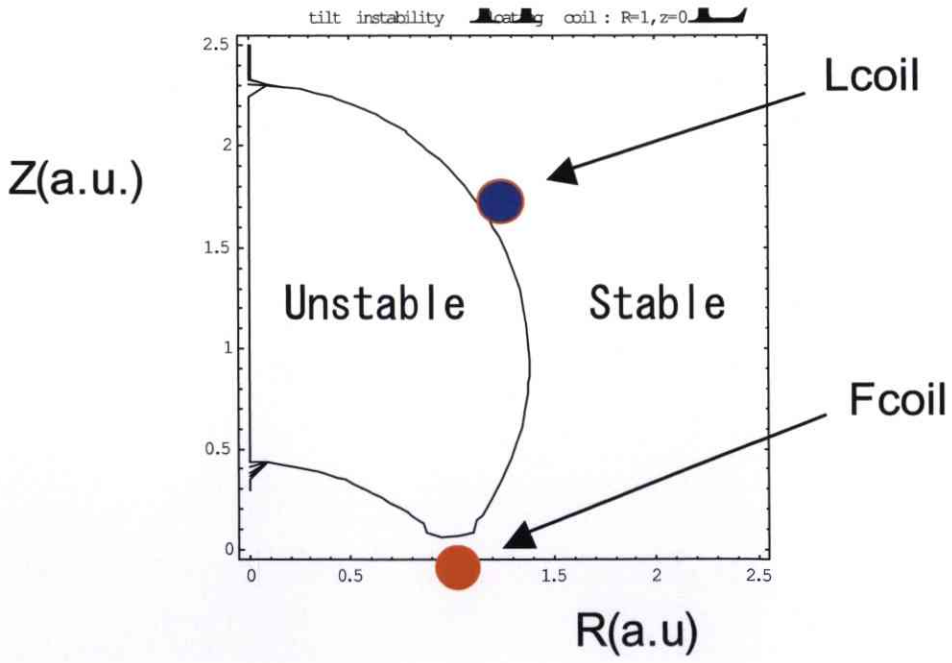

Figure 2.14: The stability of the tilting. Red and blue points denote the locations of the internal coil (F-coil) and the levitation coil (L-coil), respectively. L-coil locates around the boundary between the stable and unstable regions.

2.4.6 Magnetic Configurations

There are two types of the magnetic field configurations, one is the simple dipole configuration (the internal coil must be supported) and the other is the separatrix configuration. Moreover, a separatrix configuration involves both conditions of an experiment with the supported and the levitated internal coils. Figures 2.15 and 2.16 show the simple dipole and the separatrix configuration, respectively.

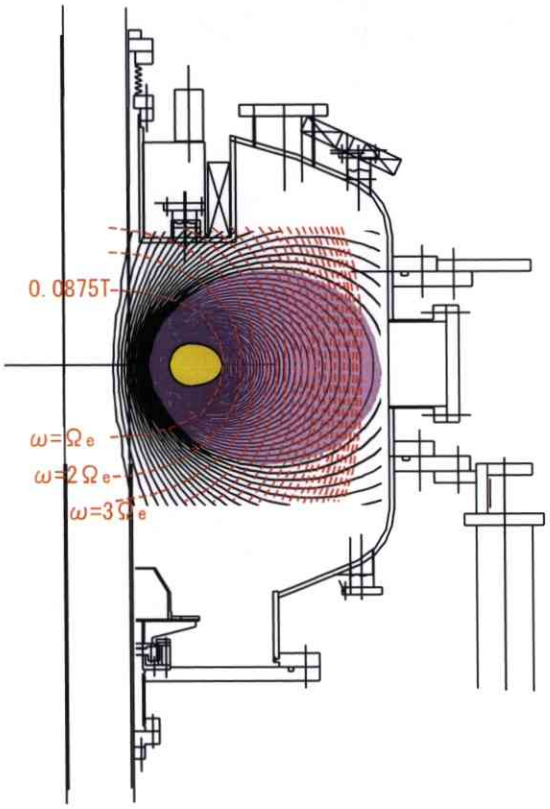

Figure 2.15: The dipole configuration. Solid and dotted lines show the magnetic flux surfaces and contours of the magnetic field strength, respectively. Each contour represents the nth harmonic electron cyclotron resonance layer (n=1,2,...,20).

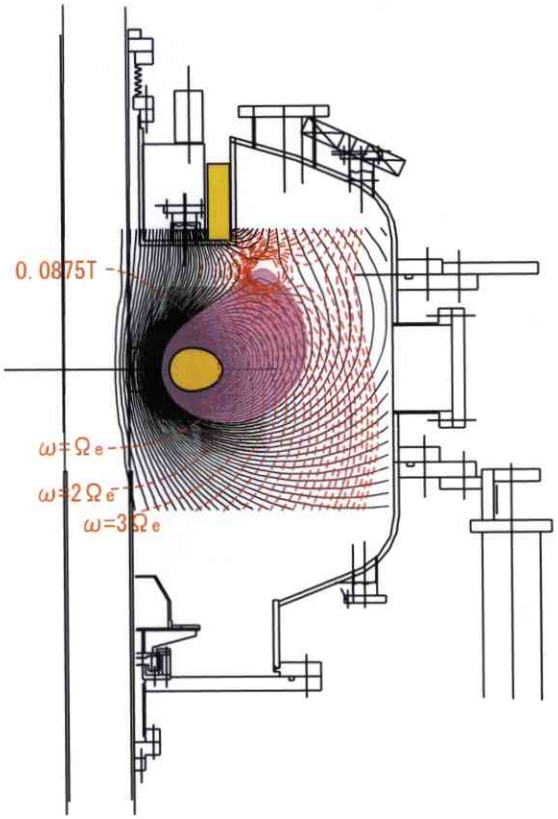

Figure 2.16: The separatrix configuration. Solid and dotted lines have the same meaning of them in Fig. 2.15. The plasma confinement region is determined by the separatrix. Location of the separatrix is determined by the ratio of the internal coil current to the levitation coil one.

Figure 2.17: A photograph of a plasma with the simple dipole configuration.

Figure 2.18: A photograph of a plasma with the separatrix configuration.

A plasma is produced by the Electron Cyclotron Heating (ECH), and details about the heating system is described in Chap. 4. Figures 2.17 and 2.18 show photographs of plasmas with the simple dipole and the separatrix configurations, respectively. One can realize from the emission of visible lights that a plasma is produced in the closed magnetic flux surfaces, i.e. separatrix.

2.5 Other Concepts of a Dipole Confinement

In the 1970's, there are dipole and multipole devices, which are oriented to investigate the MHD stability. The magnetic well and the magnetic shear effects were shown by experiments on internal coil devices. Representative example of those devices are Octapole [52], Levitron [12], Spherator [91]. Especially, levitated version Spherator achieved extremely long confinement time of articles, i.e., $\tau_p >\sim 300\tau_B$ [92], where τ_B is the Bohm diffusion time. However, most of the internal coil devices were shut down due to difficulties in applications to fusion reactors.

A. Hasegawa proposed another relaxation theory, i.e. the kinetic relaxation under the conservation of a magnetic moment μ and a second adiabatic invariant J [25]. He predicted the equilibrium plasma that has a steep pressure gradient is stable against low frequency instabilities for local beta exceeding unity. Furthermore J. Kesner proposed a fusion power source which was based on an alternative fuel cycle "helium catalyzed D-D" [32]. A dipole magnetic field may have the capability of excellent energy confinement with low particle confinement, whereas conventional fusion devices have good energy confinement with good particle confinement. To identify these concepts, the Levitated Dipole eXperiments (LDX) was constructed [19].

Chapter 3

Characteristics of Electron Bernstein Waves

3.1 Plasma Heating and a Wave with an Electron Cyclotron Range of Frequency

Plasma heating and current drive are closely related. Heating means giving energy to a plasma, while current drive does giving momentum to it. Since a plasma is a cloud of charged particles, it has the electric conductivity. In other words, since a plasma has electrical resistivity, a plasma current heats plasma itself by the Joule heat. Conversely, a high temperature (low collisionality) plasma drives a current, which is known as Bootstrap current, by itself. One can easily understand plasma heating and current drive are taken place complementary.

One can categorize the methods of plasma heating and current drive as following three things.

1. Ohmic Method
2. Neutral Beam Injection (NBI)
3. Radio Frequency (RF) Wave Launching

This work is concerned with the third one "Radio Frequency Wave Launching". The Electron Bernstein Wave (EBW) is a kind of RF waves with an Electron Cyclotron Range of Frequency (ECRF). Figure 3.1 describes the relationships between physical models of waves in plasmas with an Electron cyclotron Range of Frequency. The most general picture is the hot plasma

wave model. If an electron Larmor radius is much greater than a wavelength, plasma is no-longer magnetized, so that unmagnetized plasma model is valid. Furthermore zero density limit leads to remove the density effect, i.e. shielding of the electromagnetic field by the motion of charged particles, then it goes to the vacuum limit. If an electron Larmor radius is much smaller than a wavelength, the locations of electrons may treat as their guiding center, thus the cold plasma approximation is adequate. In most cases, waves in plasma can be treated as the cold waves, e.g. $\rho_e \sim 1\mathrm{mm}$ when $T_e \sim 10\mathrm{eV}$ and $B \sim 0.05\mathrm{T}$, whereas the wavelength of the corresponding ECRF wave in vacuum is around 200 mm. The cold plasma approximation is invalid around the resonance regions. If the Larmor radius is as long as a wavelength, one can easily derive that the polarization of it is an electrostatic (longitudinal) mode. Moreover an electrostatic wave which propagates perpendicular to the magnetic field is called an electron Bernstein wave.

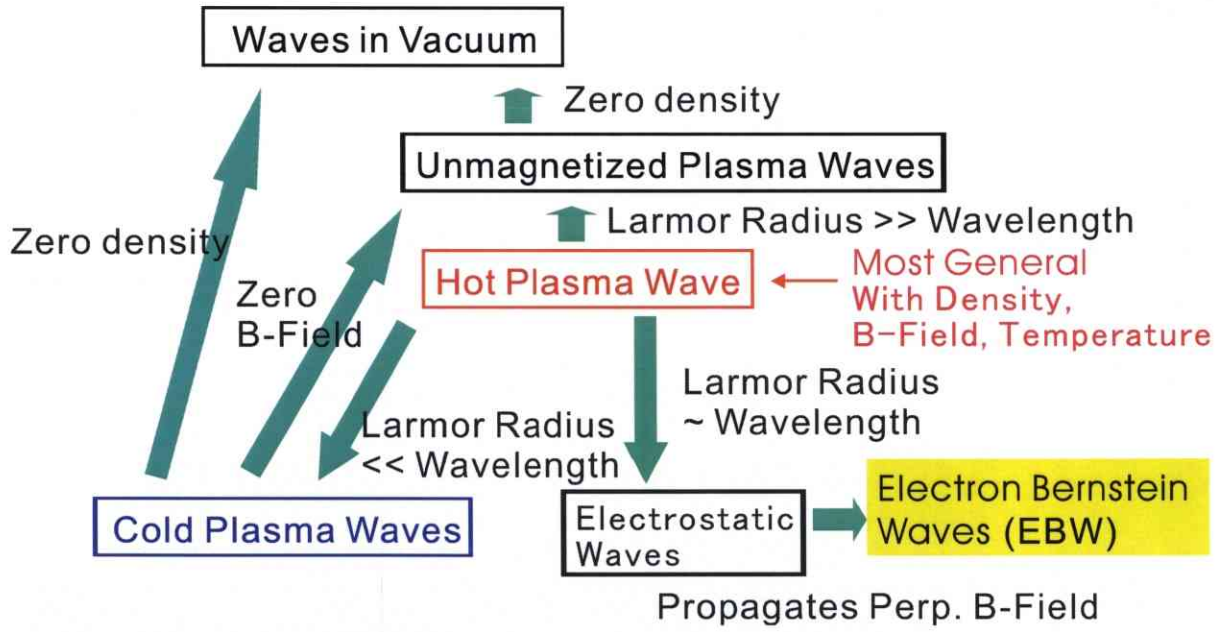

Figure 3.1: The relationships of the physical models of waves in plasmas with an Electron Cyclotron Range of Frequency.

3.2 Dispersion Relation of an Electron Bernstein Wave

The Electron Bernstein Wave (EBW) is an electrostatic mode propagating perpendicular to the magnetic field [7]. If the electric field varies as longitudinal wave, Maxwell equations lead to the Poisson equation and the charge continuity equation. As defined in Eq. (A.10),

the first order perturbed current is time derivation of the polarization vector. The right hand side of the Poisson equation is equal to be 0, and the electric field can be expressed by the scalar potential φ:

$$\nabla \cdot (\overleftrightarrow{K} \cdot \nabla\varphi) = 0. \tag{3.1}$$

We obtain

$$N_x^2 K_{xx} + N_y^2 K_{yy} + N_z^2 K_{zz} + N_x N_y (K_{xy} + K_{yx}) + N_x N_z (K_{xz} + K_{zx}) + N_y N_z (K_{yz} + K_{zy}) = 0. \tag{3.2}$$

Let the direction of the magnetic field and the wavenumber vector be the z direction and in the x-z plane, respectively, Eq. (3.2) can be simplified as

$$N_x^2 K_{xx} + N_z^2 K_{zz} + 2N_x N_z K_{xz} = 0. \tag{3.3}$$

Moreover, the dispersion relation for an electrostatic wave propagating perpendicular to the magnetic field, i.e. Bernstein wave, is resolved to be

$$K_{xx} = 0. \tag{3.4}$$

The xx component of a specific dielectric tensor of the hot plasma wave is derived in Eqs. (A.167) and (A.178), here we assumed a plasma has isotropic Maxwellian distribution function without a flow, so that Eq. (3.4) is represented as

$$1 + \sum_s \frac{\omega_{ps}^2 \mathrm{e}^{-\lambda_s}}{\omega k_z v_s} \sum_{l=-\infty}^{\infty} \frac{l^2 I_l(\lambda_s)}{\lambda_s} Z(\zeta_s) = 0, \tag{3.5}$$

where $Z(\zeta_s)$ is the plasma dispersion function [17]. In this case, the z component of a wavenumber vector goes to zero, so that the parameters ζ_{sl} are infinity. Therefore the plasma dispersion function $Z(\zeta_{sl})$ can be expanded by the asymptotic form:

$$Z(\zeta_{sl}) = \mathrm{i}\sqrt{\pi}\,\mathrm{sgn}(k_z)\exp(-\zeta_{sl}^2) - \frac{1}{\zeta_{sl}} - \frac{1}{2\zeta_{sl}^3} - \cdots. \tag{3.6}$$

Usually one can neglect the first term of Eq. (3.6). From Eqs. (3.5) and (3.6), and neglecting contributions from ions, the dispersion relation of EBW is obtained:

$$1 - \frac{2\omega_{pe}^2 \mathrm{e}^{-\lambda_e}/\lambda_e}{\Omega_e^2} \sum_{l=1}^{\infty} \frac{l^2}{q^2 - l^2} = 0, \tag{3.7}$$

where $q \equiv \dfrac{\omega}{\Omega_e}$ and $\omega \sim \Omega_e >> \Omega_i$.

The characteristics of an EBW can be discussed conveniently by definition of new parameter $\alpha(q,\lambda)$, and hereafter λ means λ_e if not otherwise specified:

$$\alpha(q,\lambda) = 2\sum_{l=1}^{\infty} \mathrm{e}^{-\lambda} I_l(\lambda) \frac{l^2}{q^2 - l^2}. \tag{3.8}$$

Equation (3.7) can be rewritten as

$$\frac{\Omega_e^2}{\omega_{pe}^2} = \frac{\alpha(q,\lambda)}{\lambda}. \tag{3.9}$$

The cutoff occurs when $N_\perp = 0$, i.e. $\lambda = \frac{1}{2} k_\perp^2 \rho_e^2 = 0$, is satisfied. The series expansion of α with respect to λ is [69]

$$\alpha(q,\lambda) = \frac{\lambda}{(q^2 - 1^2)} + \frac{1 \cdot 3\lambda^2}{(q^2 - 1^2)(q^2 - 2^2)} + \frac{1 \cdot 3 \cdot 5\lambda^3}{(q^2 - 1^2)(q^2 - 2^2)(q^2 - 3^2)} + \cdots, \tag{3.10}$$

therefore one can easily show a cutoff occurs when

$$\omega = \omega_{UH} \tag{3.11}$$

or

$$\omega = n|\Omega_e| \qquad n = 2, 3, \cdots. \tag{3.12}$$

is satisfied. On the other hand, resonance occurs when $\lambda \to \infty$.

$$\alpha(q,\lambda) \to \frac{2}{\sqrt{2\pi\lambda}} \sum_{l=1}^{\infty} \left[\frac{1^2}{q^2 - 1^2} + \frac{2^2}{q^2 - 2^2} + \cdots \right], \tag{3.13}$$

therefore resonance occurs

$$\omega = n|\Omega_e| \qquad n = 1, 2, \cdots. \tag{3.14}$$

Figure 3.2 shows $\alpha(q,\lambda)/\lambda$ versus q with several λ [7]. By changing the value of λ, one can graphically obtain a solution of Eq. (3.9) at any value of q.

The solution of the dispersion relation is drawn in Fig. 3.3 [13][36]. Resonances occur at any harmonic ECR layer, and cutoffs occur at same location. In addition, there are infinite branches of EBWs. Parameters in Fig. 3.3 is the ratio of the square of an electron plasma frequency and an electron cyclotron frequency; i.e. $(\omega_{pe}/\Omega_e)^2$. As mentioned above, the UHR is the sole exceptional instance of the location of a cutoff, and the branch which involves the UHR corresponds to an EBW which is excited from an electromagnetic mode, hereafter let one call this branch as excitation branch. If the location of the UHR lies between the fundamental and the second harmonic ECR, there are no turning point $(\mathrm{d}\omega/\mathrm{d}k)$ in this branch. On the

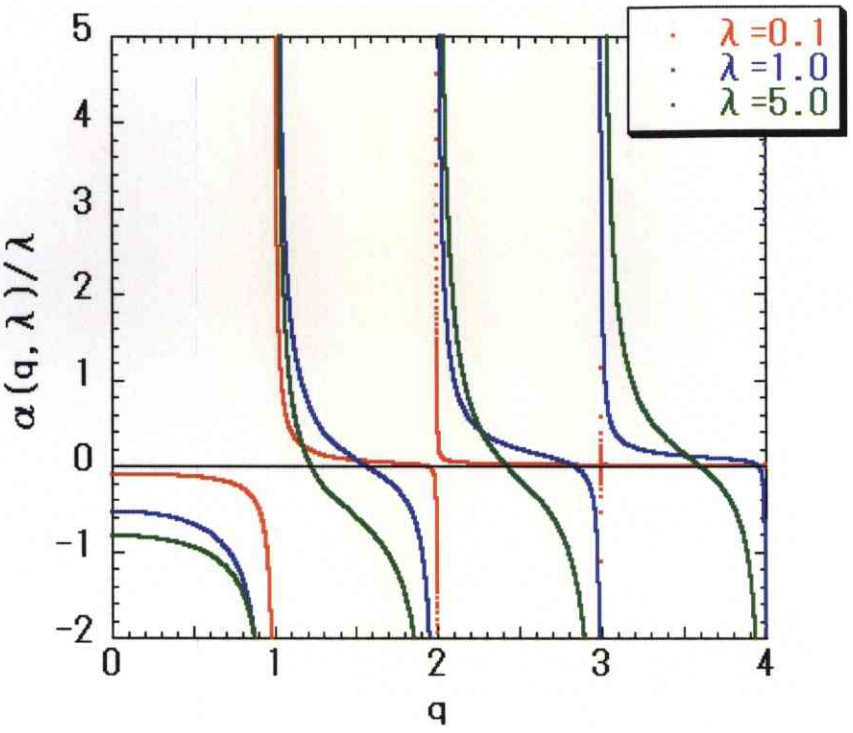

Figure 3.2: Plots of $\alpha(q, \lambda)/\lambda$ vs q.

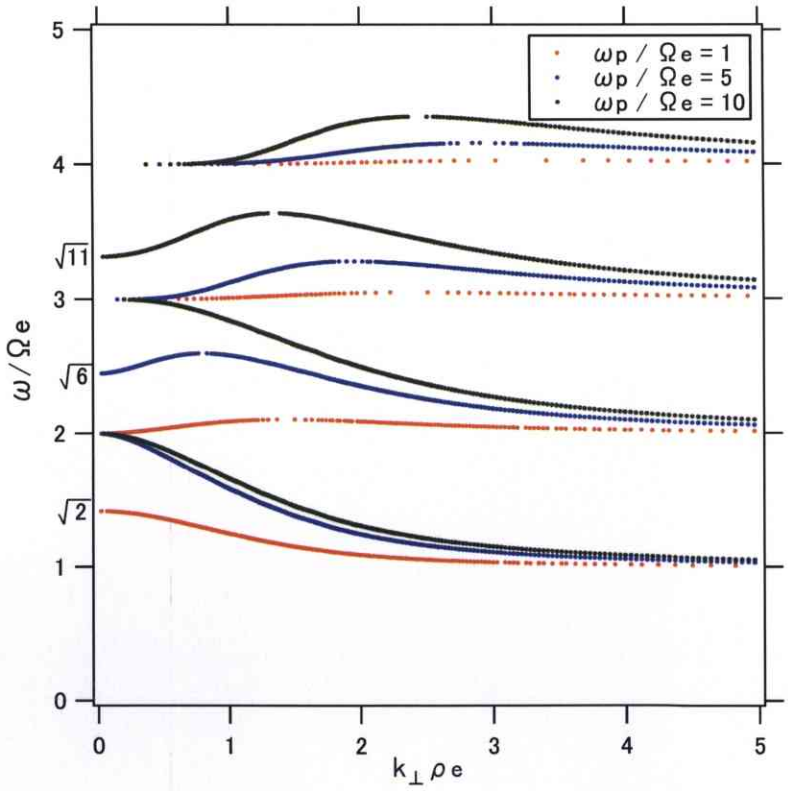

Figure 3.3: The dispersion relation of EBWs.

other hand, if the UHR locates at lower field side, there is a turning point in excitation branch. One can see the group velocity $\mathrm{d}\omega/\mathrm{d}k$ is negative (backward wave) except for the region between the cutoff and turning point. From the gradient of Fig. 3.3,

$$\frac{\omega}{\Omega_e}/(k_\perp \rho_e) = \frac{v_{g\perp}}{v_{th,e}} \tag{3.15}$$

is obtained, where $v_{th,e}$ denotes an electron thermal velocity, i.e. it represents the ratio of a group velocity to an electron thermal velocity. One can easily realize a typical value of a group velocity of an EBW is of the order of an electron thermal velocity.

In reality, the electrostatic mode is invalid when the refractive index is of the order of unity or less. In such a region, one should go back to a more general case, i.e. the hot plasma wave model. Figure 3.4 compares three models of the dispersion relation, i.e. a cold plasma, a hot plasma and an EBW. Here we assumed $100 v_{th,e} = c$ is satisfied. In the hot wave model, Maxwell equation of a perpendicularly propagating wave is solved; i.e.

$$K_{xx}(K_{yy} - N^2) - K_{xy}K_{yx} = 0, \tag{3.16}$$

where K_{xx}, K_{xy}, K_{yx}, K_{yy} and N denote xx, xy, yx, yy components of a specific dielectric tensor (Eqs. (A.167), (A.177)-(A.179)) and a refractive index, respectively. One can easily show $K_{xz} = K_{zx} = K_{xy} = K_{yx} = 0$ if the parallel component of a wavenumber vector equals to zero, so that the dispersion relation is simplified as Eq. (3.16). This is an extraordinary wave; on the other hand, $K_{zz} = 0$ corresponds to the dispersion relation of an ordinary wave. As shown in Fig. 3.4, the solutions of Eq. (3.16) coincide the solution of the cold plasma model when a refractive index is small, whereas they coincide the solution of the EBW when a refractive index is high. Moreover, one can see that a cold X-wave continuously varies to an EBW around the UHR. Therefore one can understand it is necessary to reach X-wave to the UHR for the mode-conversion into the EBW in a plasma.

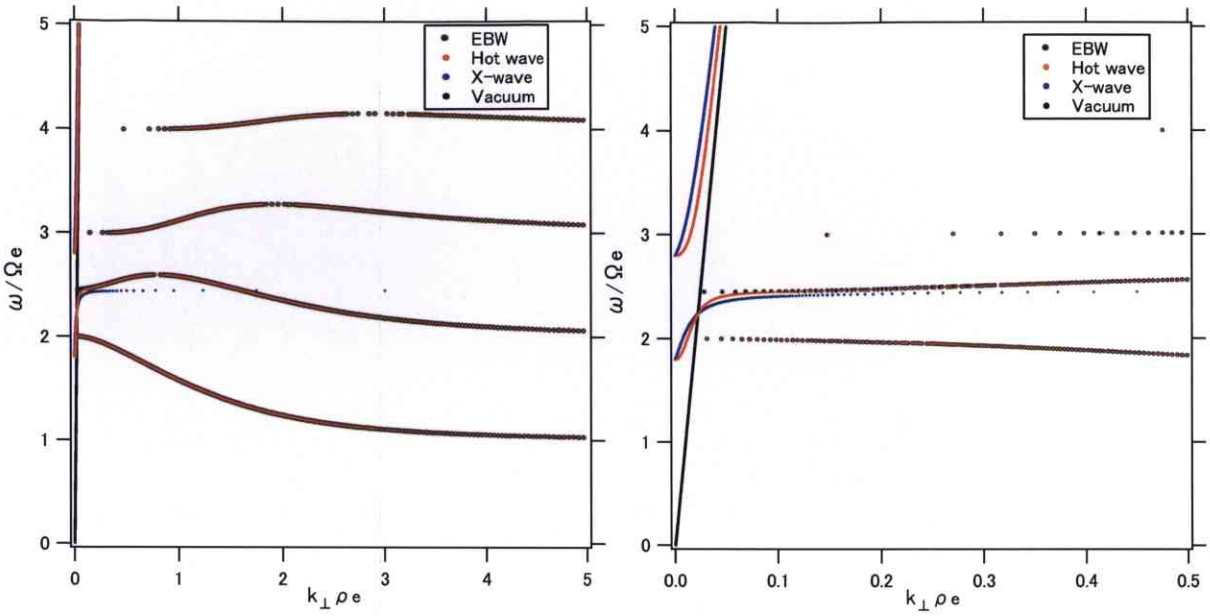

Figure 3.4: (a) The comparison between three models of the dispersion relation of waves in a plasma. (b) The expansion of (a).

3.3 Spacial Profiles of Refractive Indices in Mini-RT

As shown in the previous section, the dispersion relation of an EBW is a function of the magnetic field strength, an electron density and an electron temperature. Thus, by using these profiles, one can calculate refractive index profiles of a cold X-wave and an EBW.

Figure 3.5 shows refractive index profiles with typical parameters in the Mini-RT device. Here simple dipole configuration is assumed, and the profiles of a magnetic filed strength and an electron density on the mid-plane of the device are shown in Fig. 3.6. Electron density is assumed to be 10 eV and spatially uniform, which are approximately coincide the actual measurement by a triple probe (see Chap. 5) [82]. In addition, 1.0 GHz of a frequency is considered in Fig. 3.5. In this case, mode-conversion occurs around $R = 0.328$ m, which lies between 3rd and 4th harmonic electron cyclotron resonance (ECR) layers. An excited EBW is expected to propagate towards the 3rd ECR layer and to be damped there. Since the location of the UHR depends on a magnetic field strength and an electron density, a density profile affects the location at which the mode-conversion occurs. Especially in a dipole device, there is quite a steep magnetic field gradient, so that a lot of harmonic ECR layers exist in a plasma. Therefore the locations where an EBW is excited and damped may vary owing to the change or fluctuation of an electron density.

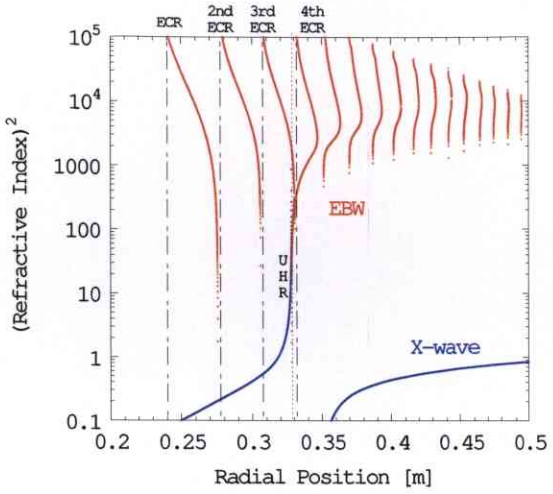

Figure 3.5: Refractive index profiles of an X-wave and an EBW on the simple dipole configuration. Dotted and dashed lines denote the locations of the UHR and ECR, respectively.

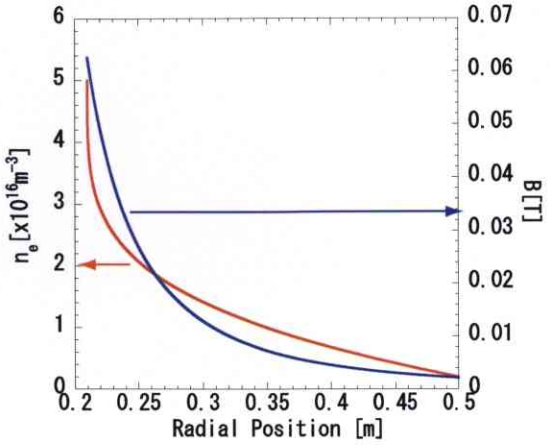

Figure 3.6: Assumed density and magnetic field profiles on the simple dipole configuration.

On the separatrix configuration, a density profile is localized, so that mode-conversion around the lower ECR layer can be expected. Figures 3.7 and 3.8 show the refractive index profiles and assumed parameters, respectively, on the separatrix configuration. Here we assumed the location of the separatrix is $R = 0.32$ m. For comparison with the result on the simple dipole configuration, similar shape of a density profile is assumed. Mode conversion is expected to occur between 2nd and 3rd harmonic ECR layers. In this configuration, electron density goes to zero around the separatrix, therefore if a plasma has a steep density gradient at the edge region, mode-conversion always occur around the separatrix. Figures 3.9-3.12 show the refractive index profiles and examples of a density profile. The magnetic field strength is fixed and a density profile is varied in this calculation. One can see that although electron density differs twice, the location at which mode-conversion occurs is almost same. As described in Chap. 5, actual density profile on the separatrix configuration is similar to Figs. 3.10 and 3.12 rather than Fig. 3.8, i.e. there is a steep density gradient around the separatrix.

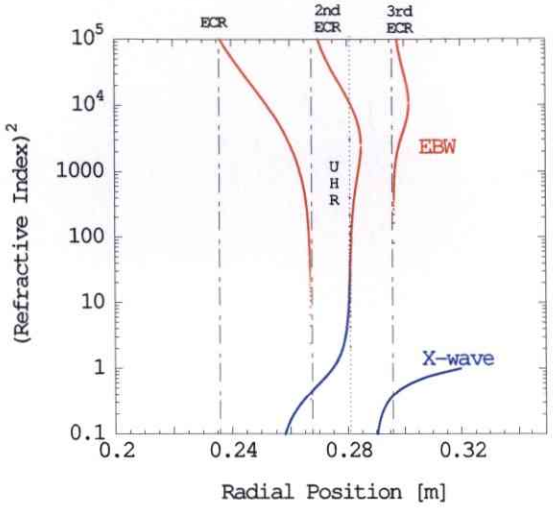

Figure 3.7: Refractive index profiles of an X-wave and an EBW on the separatrix configuration.

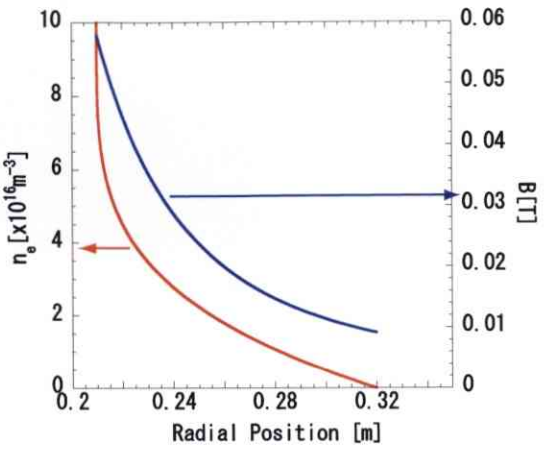

Figure 3.8: Assumed density and magnetic field profiles on the separatrix configuration.

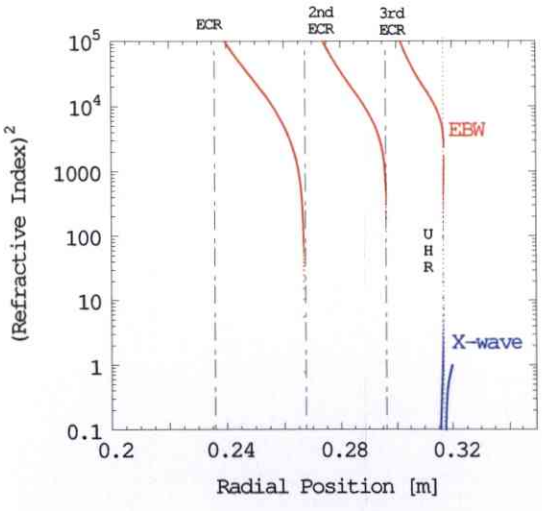

Figure 3.9: Refractive index profiles when the steep density gradient lies around the separatrix.

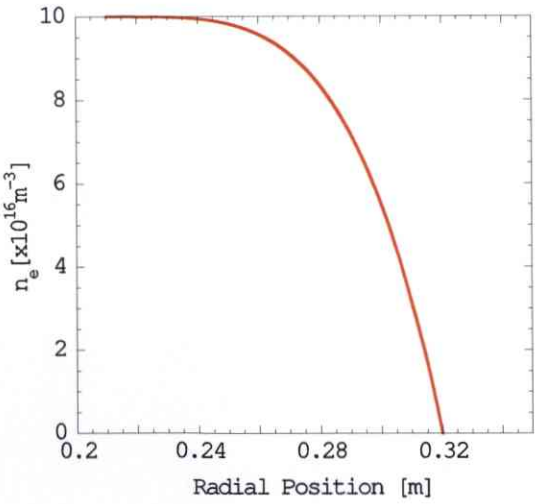

Figure 3.10: Assumed density profile on the calculation of Fig. 3.9.

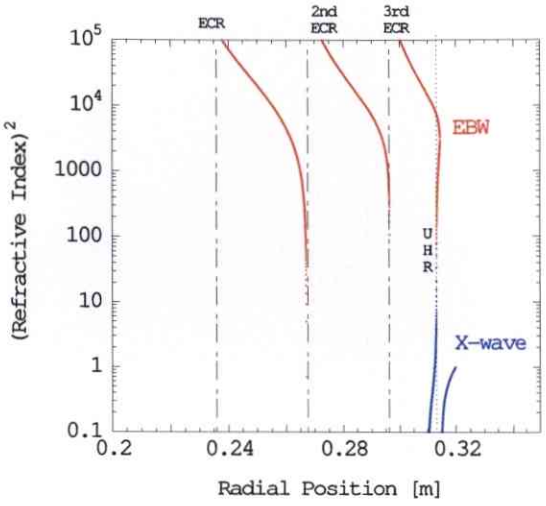

Figure 3.11: Refractive index profiles when the electron density profile halves from Fig. 3.9.

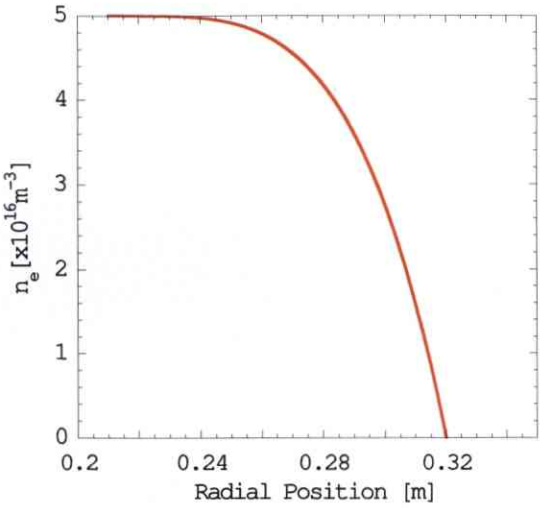

Figure 3.12: Assumed density profile on the calculation of Fig. 3.11.

3.4 Mode Conversion

Since the EBW is an electrostatic wave having a wavelength of the order of the electron Larmor radius, it cannot propagate in vacuum. Thus some method to convert from electromagnetic wave (EMW) into EBW is necessary.

3.4.1 Principle of Mode Conversion into an Electron Bernstein Wave

It is well known that there are three methods to convert EMW to EBW.

- Perpendicular injection of X-Wave from high field side (SX-B Conversion)
- Perpendicular injection of X-Wave from low field side (FX-SX-B Conversion)
- Oblique injection of O-Wave from low field side (O-X-B Conversion)

Figure 3.13 is the CMA diagram which shows the normal surface of the wave (This figure is quoted from Ref. [44]). In this figure, the horizontal axis corresponds to the square of a plasma frequency (density) normalized by incident wave's frequency. The vertical axis denotes the electron cyclotron frequency (magnetic field strength) normalized by incident wave's frequency.

Solid (dotted) lines represent various resonance (cutoff) layers. If the incident wave is launched from outside the plasma, initial position of the incident wave on the CMA diagram is a spot on the vertical axis. The difficulty of reaching X-wave to the UHR is overcoming the evanescent region, which lies low field and low density side of the UHR.

Figure 3.14 shows the schematic drawing of the SX-B conversion. By this method, one can reach X-wave to the UHR without passing the evanescent region. This is the simplest method in principle, however this method is technically difficult. Moreover, this method has an upper limit of density, i.e. the Left Hand Cutoff layer reflects the incident wave.

The FX-SX-B conversion is an available method, which is drawn in Fig. 3.15. First, launched fast X-wave propagates from low field side to high field side and approaches to the Right Hand Cutoff (R-Cutoff). If the evanescent region is sufficiently thin, i.e. density or magnetic field varies steeply, the incident fast X-wave tunnels the evanescent region. A portion of energy of tunneling wave is converted into an EBW. Remains, which corresponds to a slow X-wave, reaches to the Left Hand Cutoff (L-Cutoff). Finally, slow X-wave is reflected backward to the UHR, at which slow X-Wave converted into an EBW as well as the SX-B conversion.

The O-X-B conversion is also an available method, which is drawn in Fig. 3.16. Launched slow O-wave propagates from low field side to high field side and this wave passes through the R-Cutoff and the UHR and reaches to the Plasma Cutoff (P-Cutoff). If the locations of P-Cutoff and L-Cutoff overlapped, the mode conversion from O-Wave to X-Wave occurs. Finally converted X-Wave propagates to UHR and is converted into an EBW. Note that, in this case, L-Cutoff is written as

$$n_{\parallel}^2 = L, \tag{3.17}$$

where L is defined in Eq. $(\mathrm{A}.45)$. It means an X-wave cannot propagate to high field side along magnetic field at which Eq. (3.17) is satisfied. Thus the parallel component of a refractive index at the cutoff layer should be optimized as

$$n_{\parallel opt}^2 = \frac{\Omega_e}{\omega + \Omega_e}. \tag{3.18}$$

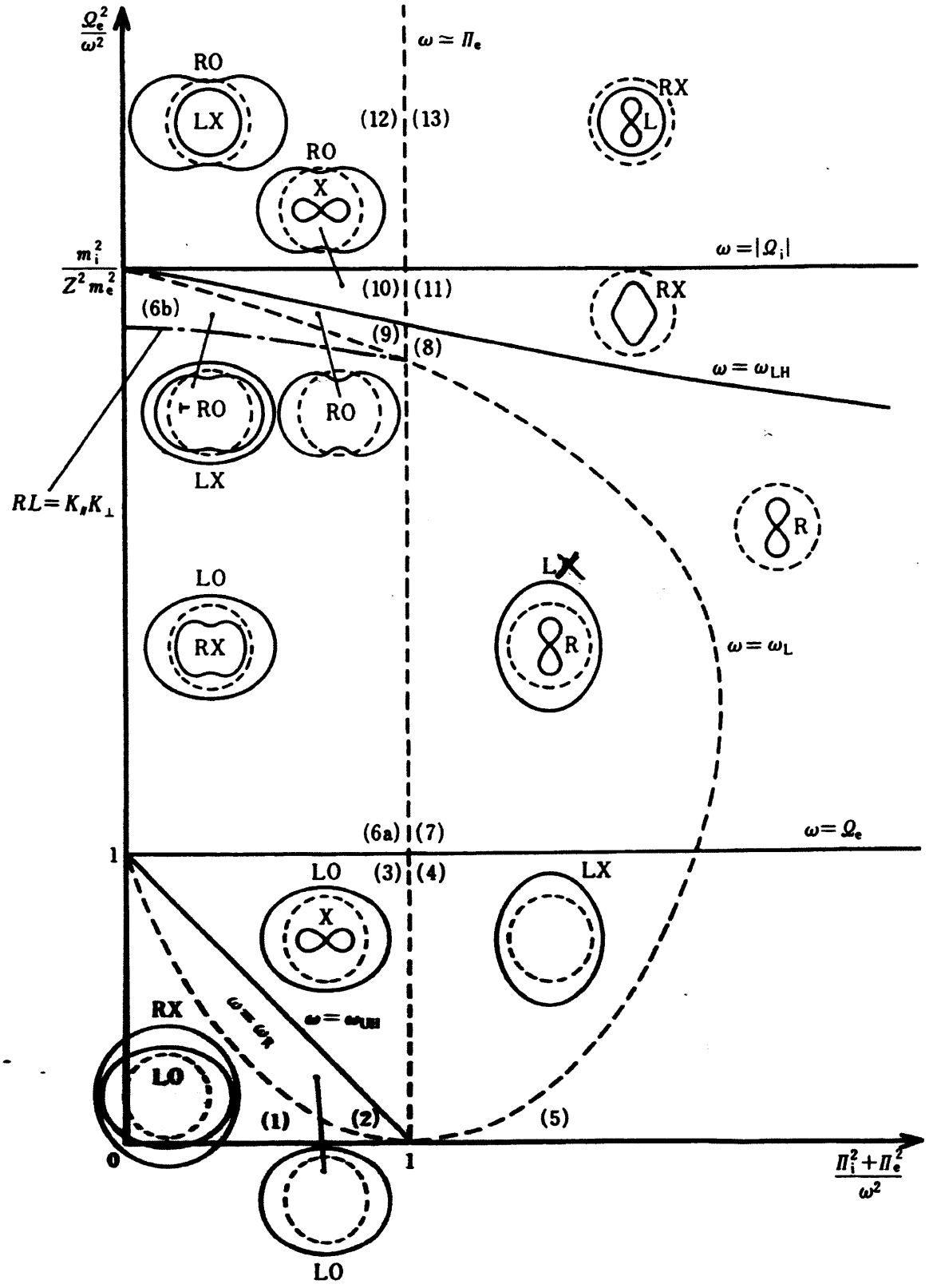

Figure 3.13: CMA Diagram.

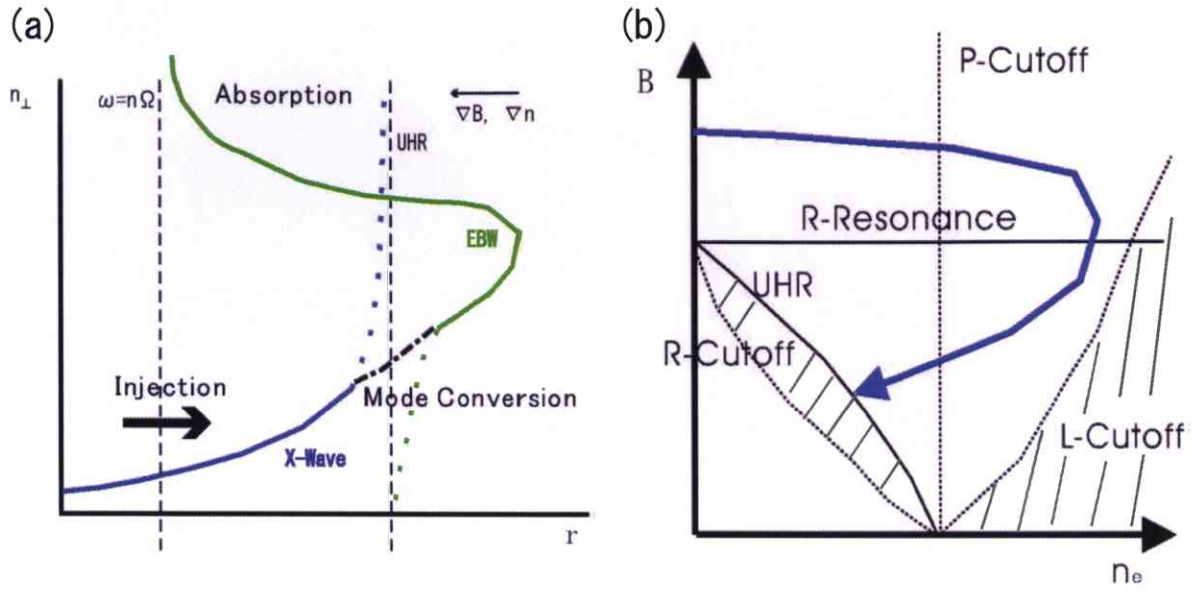

Figure 3.14: Schematic drawing of the SX-B conversion. (a) Incident wave can directly reach the UHR, and be mode-converted into EBW. (b) Trajectory of the wave on the CMA diagram. The gray lines denote the evanescent regions of an X-wave.

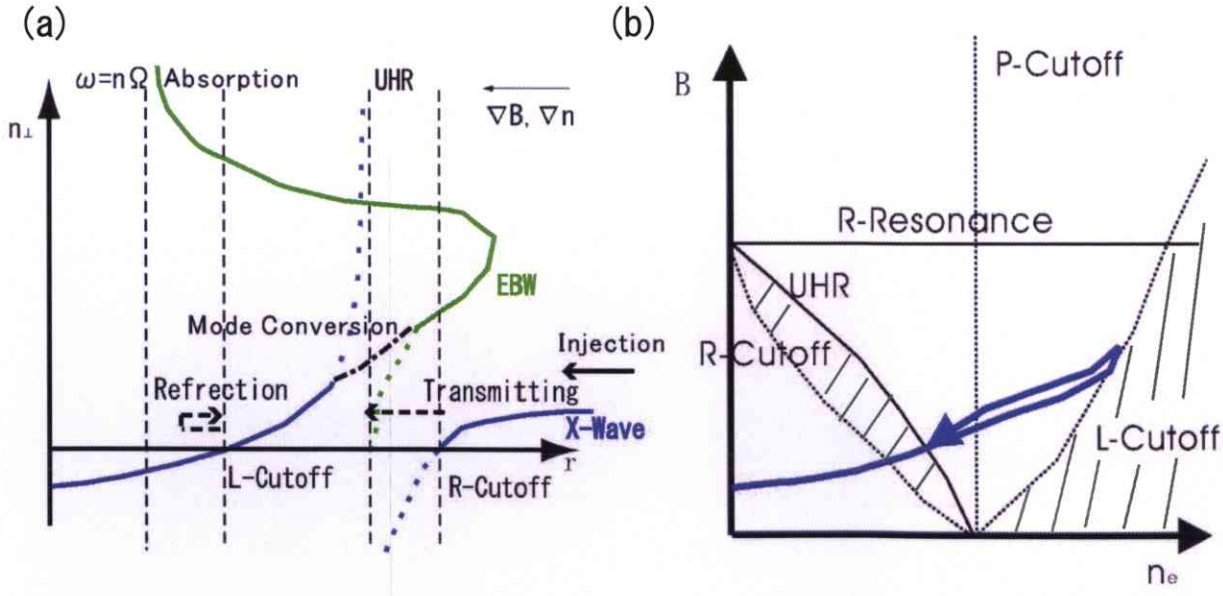

Figure 3.15: Schematic drawing of the FX-SX-B conversion.

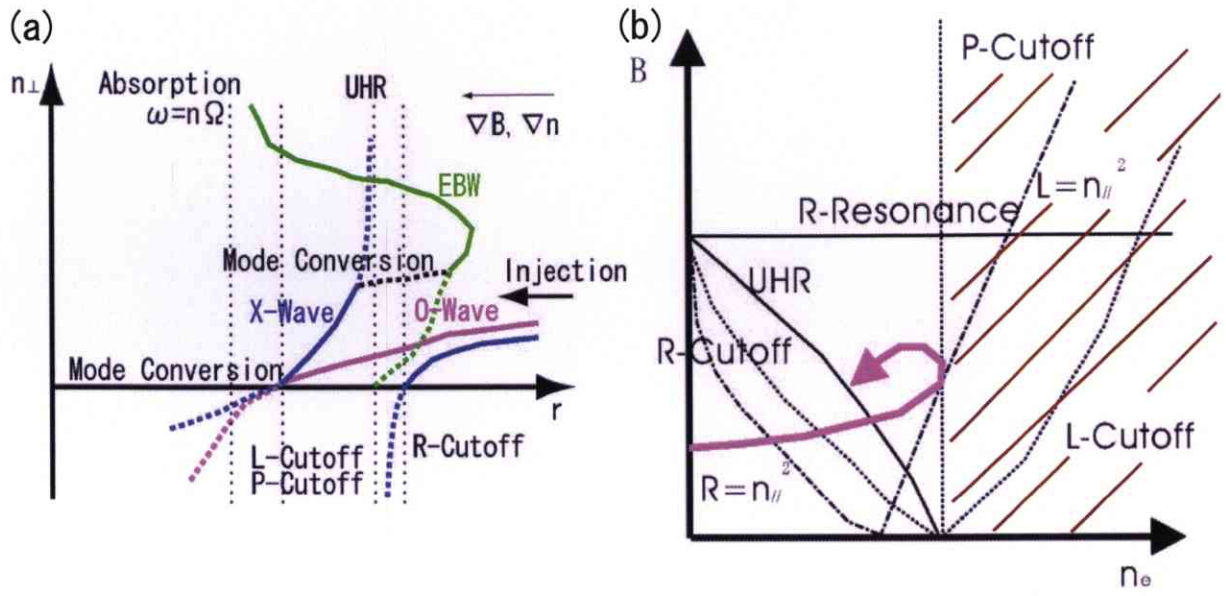

Figure 3.16: Schematic drawing of the O-X-B conversion. The brown lines represent an evanescent region of an O-wave.

3.4.2 Conversion Efficiency

An X-wave injection from low field side, i.e. FX-SX-B method, seems to be the most promising method for the mode-conversion into an EBW because of a steep density gradient around the separatrix. The mode conversion efficiency of the FX-SX-B method is

$$C(\eta, \phi) = 4\mathrm{e}^{-\pi\eta}(1 - \mathrm{e}^{-\pi\eta})\cos^2(\phi/2 + \theta). \tag{3.19}$$

Here θ is the phase of $\Gamma(-i\eta/2)$ and ϕ is determined by all of the location of the R and L-Cutoff and the UHR. The tunneling parameter η is important for mode conversion, and it is written as

$$\eta = \frac{\Omega_e L_n}{c} \frac{\alpha}{\sqrt{\alpha^2 + 2(L_n/L_B)}} \left(\frac{\sqrt{1+\alpha^2} - 1}{\alpha^2 + (L_n/L_B)\sqrt{1+\alpha^2}} \right)^{1/2}, \tag{3.20}$$

where $\alpha \equiv \frac{\omega_{pe}}{\Omega_e}$, $L_n \equiv \frac{n}{|dn/dr|}$ and $L_B \equiv \frac{B}{|dB/dr|}$ [61]. However Eqs. (3.19) and (3.20) is invalid if reflection at the L-cutoff does not occur. As shown in Fig. 3.17, there is not the L-cutoff layer at the mid-plane of the Mini-RT device for the 2.45 GHz, which corresponds to the frequency of a heating microwave, injection and a typical electron density profile (but as shown in Fig. 3.18, if an electron density is sufficiently high, the L-cutoff appears in a plasma). The wall of the vacuum vessel may behave as the cutoff layer, so that one can

expect Eq. (3.19) can be used. But for simplicity, the reflecting effect is neglected in the following discussions and the factor 4 in Eq. (3.19) is dropped. We used the model in K. G. Budden's work (see Chap. A.5). By using a typical parameters in the Mini-RT experiments, i.e. $L_n = 39$ mm, $L_B = 43$ mm, $B_{UHR} = 0.032$ T and $n_{e,UHR} = 6.5 \times 10^{16}$ m^{-3}, one can evaluate that a mode conversion efficiency in the Mini-RT device is 24 %. Here as mentioned above, the mode conversion efficiency is evaluated by K. G. Budden's expression:

$$C(\eta, \phi) = \mathrm{e}^{-\pi\eta}(1 - \mathrm{e}^{-\pi\eta}). \tag{3.21}$$

For a consideration, the evaluation of a mode-conversion efficiency when the one of the three parameters in η, i.e. L_n, L_B and α, is changed. Figures 3.19-3.21 show the result of them. The circles in figures represent an actual value of each parameter. One can realize the scale length of a density gradient is most important for the mode-conversion in a typical experiment in the Mini-RT device.

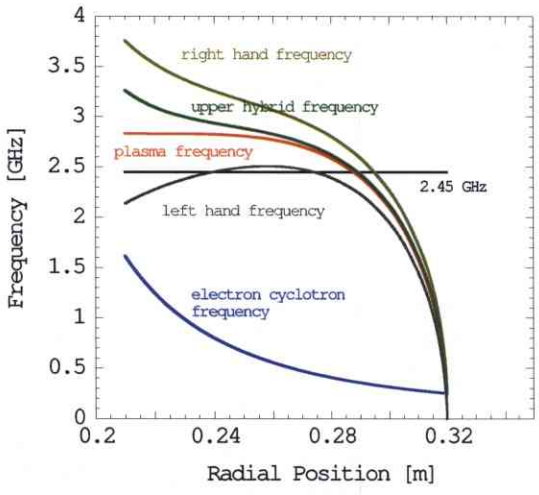

Figure 3.17: Various frequencies profile when the density profile is like Fig. 3.12.

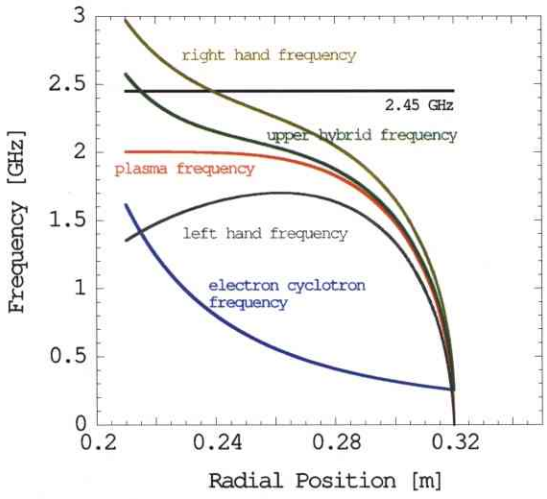

Figure 3.18: Various frequencies profile when the density profile is like Fig. 3.10.

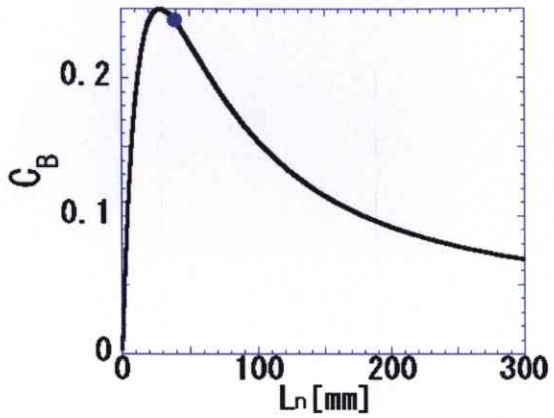

Figure 3.19: Mode-conversion efficiency if the scale length of a density gradient varies.

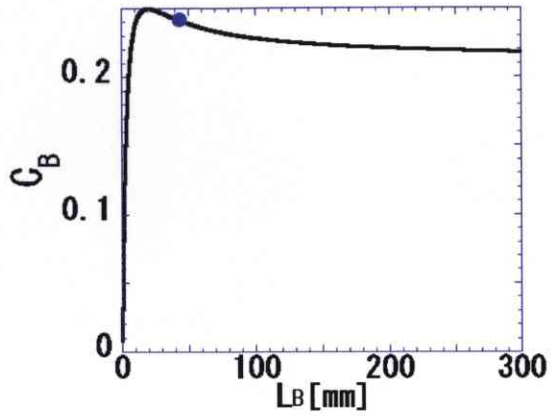

Figure 3.20: Mode-conversion efficiency if the scale length of a magnetic field gradient varies.

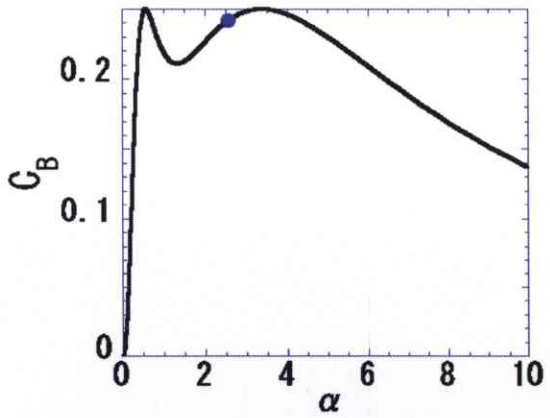

Figure 3.21: Mode-conversion efficiency if the ratio of the plasma frequency to the electron cyclotron frequency at the UHR varies.

Chapter 4

Experimental Setup on Mini-RT

4.1 Plasma Production

In Mini-RT, a plasma is produced by the Electron Cyclotron Heating (ECH) by a continuous 2.45 GHz, 2.5 kW magnetron. Microwaves generated in a magnetron are sent to an isolator, which prevents the reverse flow of reflected microwaves. Injected and reflected power can be monitored by directional couplers. The transmission mode is the TE_{10}, which is the fundamental mode in a rectangular waveguide. An electric field directs the narrow side of the rectangle, so that the launching polarization (O or X) is determined by the direction of a waveguide. In Mini-RT, a straight (stepping) waveguide is used for the O (X) mode injection. Figures 4.1 and 4.2 are photographs of a straight and a stepping rectangular waveguides. An E-H tuner decreases the reflection microwave power from a plasma. Before launching a microwave into the vacuum chamber, the transmission mode is converted to the TE_{11} mode of a circular waveguide. A horn antenna is used for launching. Figure 4.3 shows the diagram of plasma production.

Electron's gyro motion resonates with the 2.45 GHz electric field when the magnetic field strength is 0.0875 T. The cutoff density of the ordinary mode for the 2.45 GHz injection is $7.4\times10^{16}\mathrm{m}^{-3}$. Working gas is hydrogen or helium, and a typical pressure of it is $10^{-3}-10^{-1}$ Pa with the base pressure of 10^{-5} Pa. Typically, the degree of ionization is 1 % when the floating coil is supported by mechanical structures, whereas more than 10 % when it is magnetically levitated.

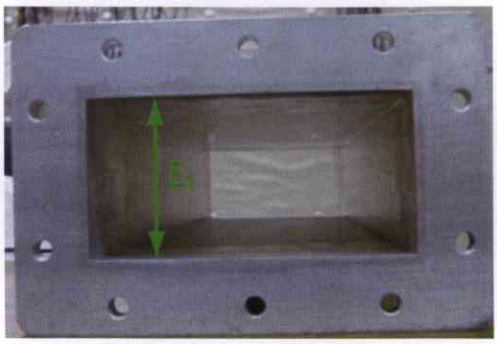

Figure 4.1: Waveguide for O-mode injection.

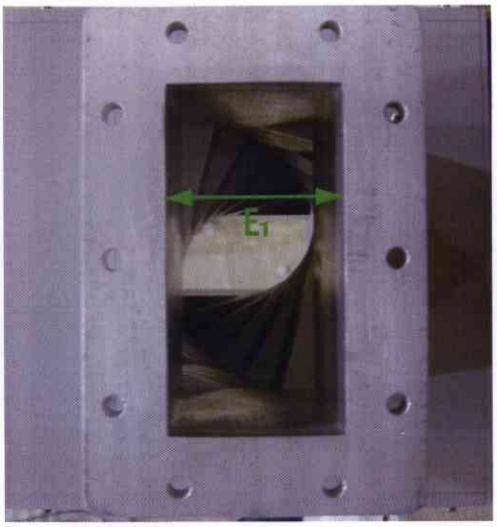

Figure 4.2: Waveguide for X-mode injection.

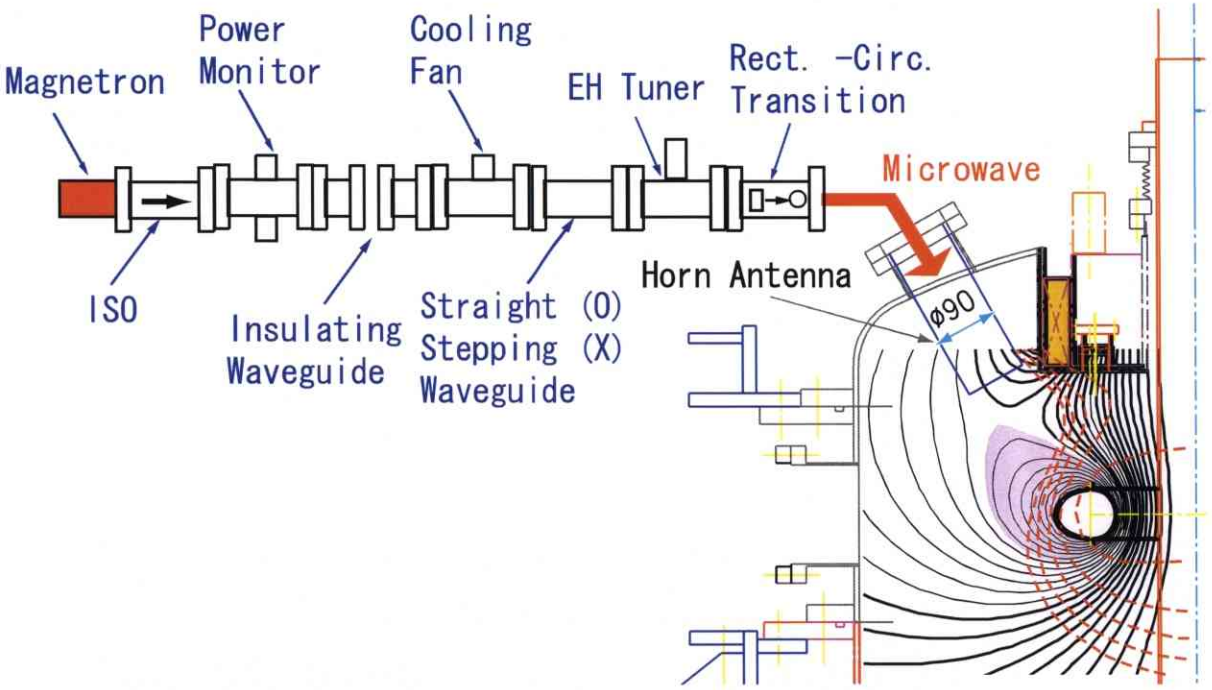

Figure 4.3: Schematic diagram of the plasma production system in the Mini-RT device.

4.2 Allocation of Detectors

Figure 4.4 shows the allocation of detectors in the Mini-RT device. Profiles of electron density and electron temperature are measured by a triple probe. Line integrated electron density is measured by a transmitting interferometer whose frequency is 75.308 GHz. ECRF electric fields are measured by interferometry with three antennas, and frequency of it (1-2.1 GHz) separates from the heating microwave (2.45 GHz). Antennas and a triple probe are fixed

to a fast moving manipulator, that is activated by a compressed air with a scanning speed of 300 mm/s (maximum). This fast scanning system is similar to the reciprocating probes [6]. The positions of antennas fixed to manipulator are measured by a slide-contact potentiometer (see Fig. 4.5). Contact probes are used for an electrical connection of a triple probe, and co-axial cables with BNC connectors are used for probing antennas. Antennas for excitation of an ECRF electric field for diagnostics are allocated at $R = 450mm$ with 22.5 degrees of toroidal deviation from the probing antennas. The horn antenna for plasma production and heating is located at toroidally opposite side of the probing antennas.

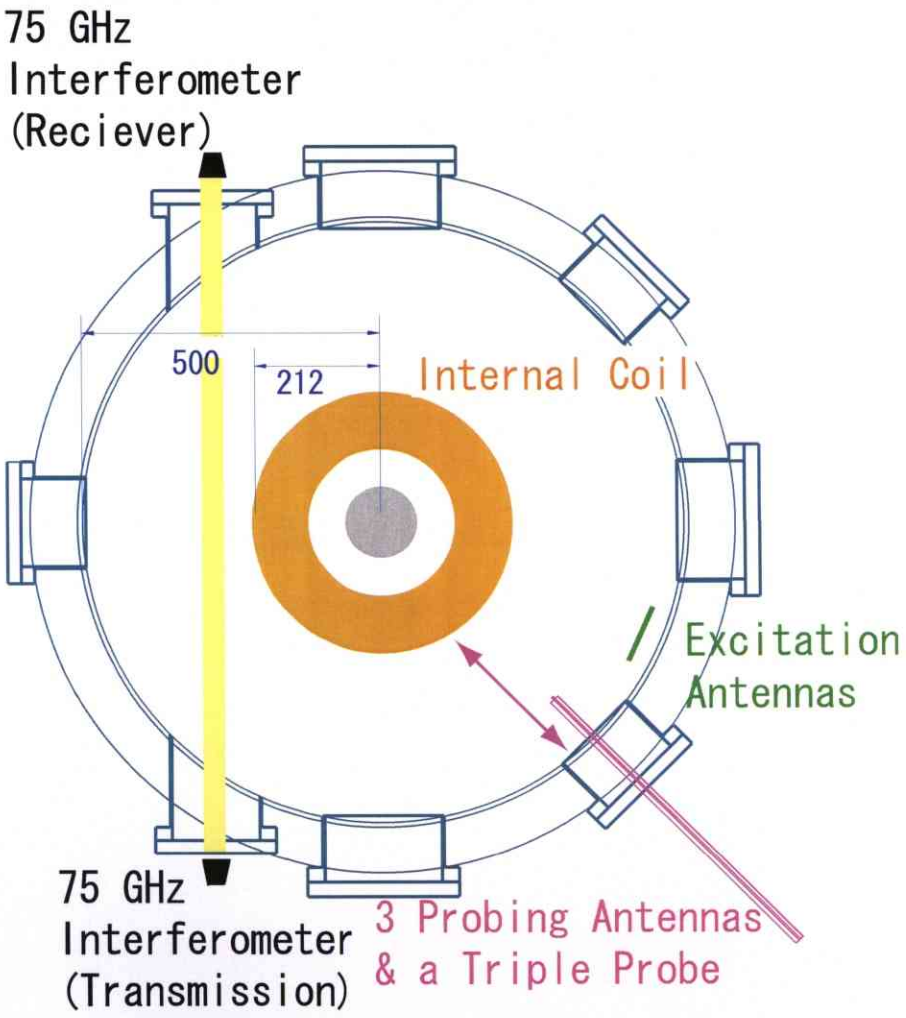

Figure 4.4: The allocation of detectors in the Mini-RT device. Profiles of electron density and electron temperature are measured by a triple probe, and line integrated electron density is measured by a transmitting interferometer, and ECRF electric fields are measured by the interferometry in a plasma.

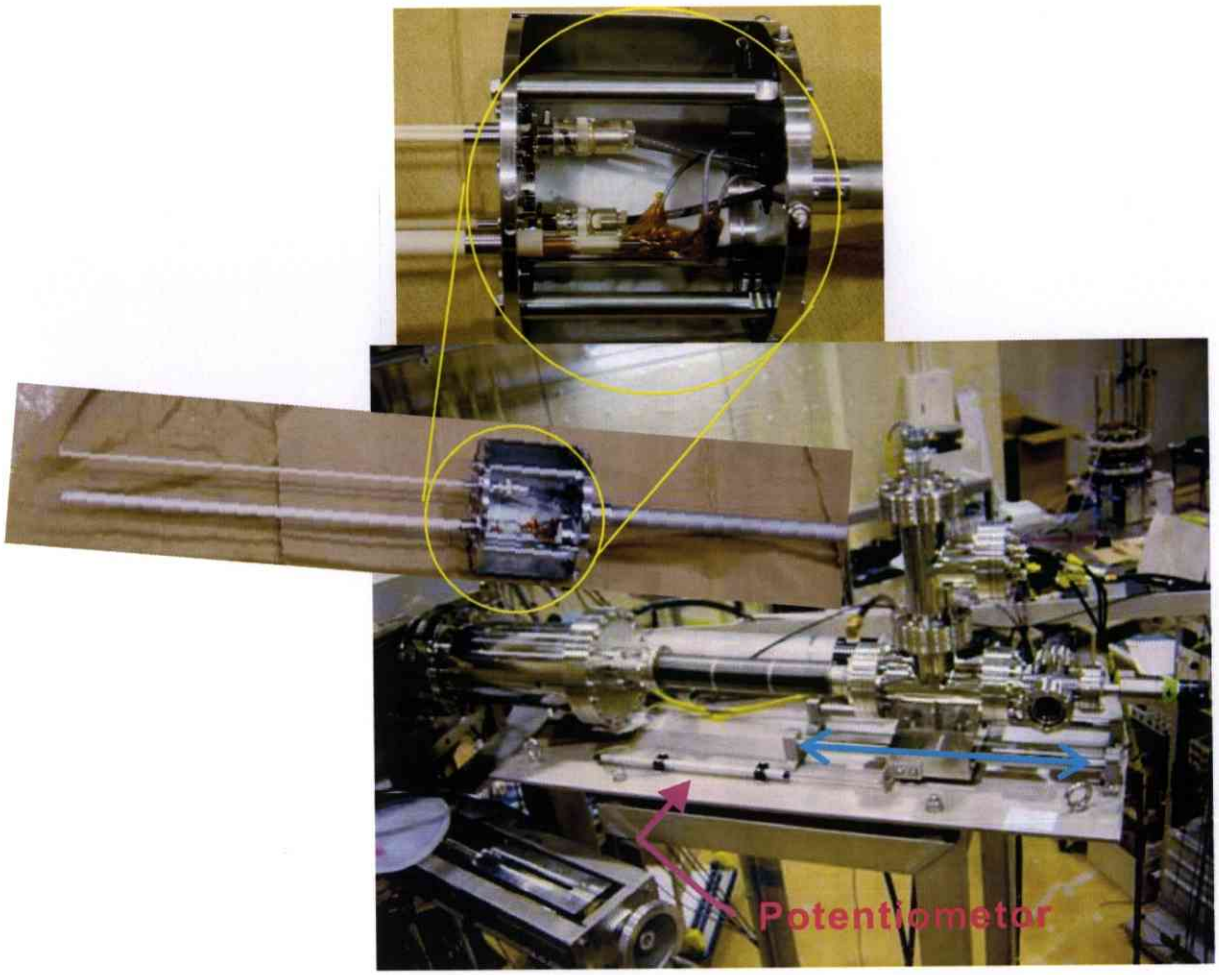

Figure 4.5: The fast scanning system. Antennas and a triple probe moves radially, and the position of them can be measured by a slide-contact potentiometer.

4.3 Density and Temperature Measurements

Profiles of electron density and electron temperature can be measured by a triple probe; however, probe measurements are based on a number of physical assumptions [11]. Thus accuracy of probe measurements should be checked carefully. On the other hand, the transmitting interferometry method is based on the variation of a refractive index owing to an electron density. We can obtain a line integrated electron density by the transmitting interferometry, but Abel inverse-conversion is necessary to know the shape of a density profile precisely.

4.3.1 Triple Probe

The triple probe is one of the Langmuir (electrostatic) probes, and it enables one to obtain electron temperature and density without a voltage sweeping. Table 4.1 denotes the typical

physical values concerned with Langmuir probe measurements. As well known, if a material with an electrical potential which is different from that of a plasma is inserted into a plasma, charged particles in a plasma may neutralize this potential difference. As the result, a sheath is formed around the surface of an inserted material. The characteristics of a sheath is determined by temperature, density and potential difference between a material and a plasma. Thus, by investigating the relationship between current and applied voltage to material, we can obtain the temperature and density [48][24]. Triple probe measures the one part of a current-voltage characteristic, so that many physical assumptions are necessary.

Table 4.1: Typical parameter in Mini-RT

Electron Density	$5.0 \times 10^{16}\mathrm{m}^{-3}$
Electron Temperature	10 eV
Ion Temperature	0.5 eV
Magnetic Field	0.05 T
Debye Length	1.1×10^{-4} m
Electron Larmor Radius	2.1×10^{-4} m
Ion Larmor Radius	2.0×10^{-3} m
Ion Sound Speed	3.1×10^{4} m/s

Since the sheath region is not electrically neutralized, if the probe potential is lower than that of a plasma, a sheath repels low energy electrons and accelerates ions. Figure 4.6 shows the schematic view of a potential profile around a probe electrode. An ideal i-v characteristic is shown in Fig. 4.7, where ideal means a flat-plate probe with a thin sheath, magnetic field can be neglected and having the Maxwellian velocity distribution function. Since electrons have more mobility than ions, we can assume electron density obeys the Boltzmann distribution

$$n_e = n_0 \exp\left(-\frac{-e(\phi - \phi_0)}{\kappa T_e}\right), \tag{4.1}$$

where n_0 and ϕ_0 denote density and electric potential at the sheath edge. Electron current can be evaluated as

$$\begin{aligned} j^- &= -e\int_{-\infty}^{\infty} \mathrm{d}v_z \int_{-\infty}^{\infty} \mathrm{d}v_y \int_{-\infty}^{0} \mathrm{d}v_x f_M(\mathbf{v}) v_x \\ &= -en_0 \exp\left(\frac{e(V_p - V_s)}{\kappa T_e}\right)\sqrt{\frac{\kappa T_e}{2\pi m_e}}, \end{aligned} \tag{4.2}$$

where V_p and V_s denote the probe and the space potential, and f_M is written as

$$f_M(\mathbf{v}) = n_0 \left(\frac{m_e}{2\pi\kappa T_e}\right)^{3/2} \exp\left(-\frac{-e(\phi-\phi_0)}{\kappa T_e}\right) \exp\left(-\frac{\frac{1}{2}m_e(v_x^2+v_y^2+v_z^2)}{\kappa T_e}\right). \quad (4.3)$$

If the probe potential is higher than the space potential, electrons are accelerated to probe. In the steady state, an electron flux $n_e v_e$ is uniform because of the particle continuous equation in the slab geometry

$$\frac{\partial n_e}{\partial t} + \nabla \cdot (n_e v_x) = 0, \quad (4.4)$$

so that electron current is independent to an applied voltage. This electron current is called the electron saturation current

$$j^- = j_{es} = -en_0\sqrt{\frac{\kappa T_e}{2\pi m_e}}. \quad (4.5)$$

If the shape of a probe is not a plate, the particle continuous equation should be changed adequately, thus electron current varies due to the increasing of a collecting area. This effect is crucial when the area of a sheath edge is much larger than the area of a probe surface.

Ion current behaves similarly to the case of an electron current. For simplicity, we assume the ion temperature is much smaller than the electron temperature, i.e. $T_i << T_e$. Then, if the probe potential is higher than the space potential, the ion current equals to zero. And the ion current is a constant (ion saturation current) when the probe potential is lower than the the space potential. In this case, electron density profile plays an crucial role to the ion current, whereas the electron saturation current is determined only by the electron itself. The reason why there is an essential difference between the electron current and the ion current is due to the difference of the mobility (small mass) and the assumption of the low ion temperature. So-called Bohm's criterion determines sheath edge potential and ion velocity at sheath edge:

$$|\phi_0| \geq \kappa T_e/2e, \quad (4.6)$$

$$v_{i,0} \geq \frac{\kappa T_e}{m_i} = C_s, \quad (4.7)$$

where C_s is called the ion sound velocity [67]. Therefore, the i-v characteristic is summarized as

$$I = I_+ + I_- = \begin{cases} -0.61Sen_e\sqrt{\dfrac{\kappa T_e}{2\pi m_e}} & (V_p > V_s) \\ 0.61Sen_e\left(\sqrt{\dfrac{\kappa T_e}{m_i}} - \exp\left(\dfrac{e(V_p-V_s)}{\kappa T_e}\right)\sqrt{\dfrac{\kappa T_e}{2\pi m_e}}\right) & (V_p < V_s) \end{cases}, \quad (4.8)$$

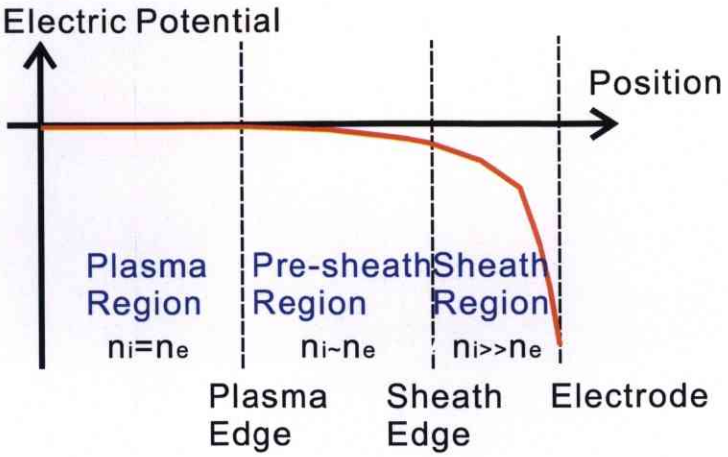

Figure 4.6: An example of a potential profile around a probe electrode. The non-neutral region is assumed to be much smaller than the plasma region. The sheath thickness is generally of the order of the Debye length.

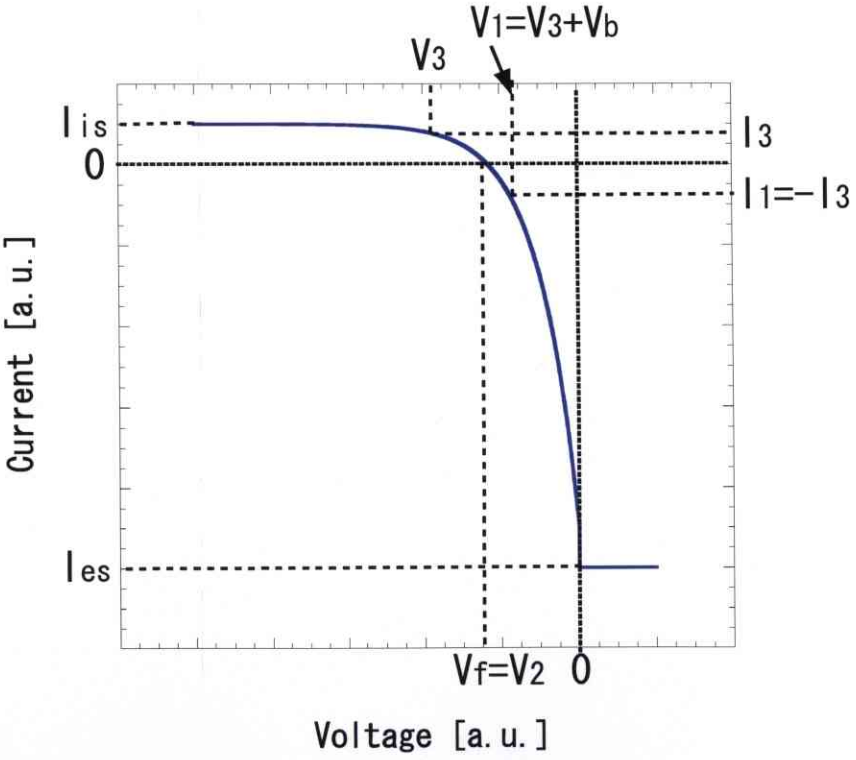

Figure 4.7: A typical Current-Voltage characteristic of a probe. The plasma potential is V_s, which is measured from a base potential. The voltage V_f is called the floating potential that means the ion current cancels the electron current. The voltages V_1, V_2 and V_3 correspond to the potentials of each probe tip of a triple probe. The voltage V_b is the bias voltage between the tips 1 and 3.

where S and n_e denote the area of a probe and electron density in a plasma region, respectively.

A triple probe is electrically floated, thus total currents into three probes are zero. One of the three probes is connected to the base potential through a high impedance resistor. Figure 4.8 shows the circuit for the triple probe measurement in Mini-RT. This high impedance resistor has 1 $\mathrm{M}\Omega$. Other two probes are also floated, and DC 90 V is biased between two probes. Since high impedance register is used, current into probe tip 2 is very small, so that $V_2 = V_f$. Similarly, the current into tip 1 coincides the opposite sign of that into tip 3

$$I_2 = I_1 + I_3 = 0. \tag{4.9}$$

Let the zero of the electric potential be the space potential, and the ratio of the electric potential energy of probes $V_{1,2,3}$ to the mean kinetic energy of electron be $\phi_{1,2,3}$, i.e.

$$\phi_k = \frac{-eV_k}{\kappa T_e}, \tag{4.10}$$

where k=1,2 and 3, the electron current can be written as

$$I_{e,k} = I_{es}\mathrm{e}^{\phi_k}. \tag{4.11}$$

Therefore, Eq. (4.9) is summarized as

$$I_{is} + I_{es}\mathrm{e}^{\phi_2} = 0, \tag{4.12}$$

$$2I_{is} + I_{es}(\mathrm{e}^{\phi_1} + \mathrm{e}^{\phi_3}) = 0. \tag{4.13}$$

These equations can be represented as

$$\frac{1}{2} = \frac{\mathrm{e}^{\phi_2}}{\mathrm{e}^{\phi_1} + \mathrm{e}^{\phi_3}} = \frac{\mathrm{e}^{-(\phi_1-\phi_2)}}{1 - \mathrm{e}^{-\phi_b}} \sim \mathrm{e}^{-(\phi_1-\phi_2)}. \tag{4.14}$$

Here we assumed the bias voltage is sufficiently large to repel electrons at the probe 3. Thus,

$$\kappa T_e = \frac{e(V_1 - V_2)}{\ln 2}. \tag{4.15}$$

is obtained. Moreover, current into probe 3 should be the ion saturation current, so that electron density can be derived from the first term of Eq. (4.8) with $V_p < V_s$.

A probe tip should not be sputtered by plasma, tungsten (W), molybdenum (Mo) and tantalum (Ta) are usually employed for probe tips. We adopted the tungsten tips whose length and diameter are 5 mm and 1.5 mm, respectively. Each tip except for probe head is coated by a ceramic tube. Figure 4.9 is a photograph of a triple probe and antennas for ECRF electric field measurements.

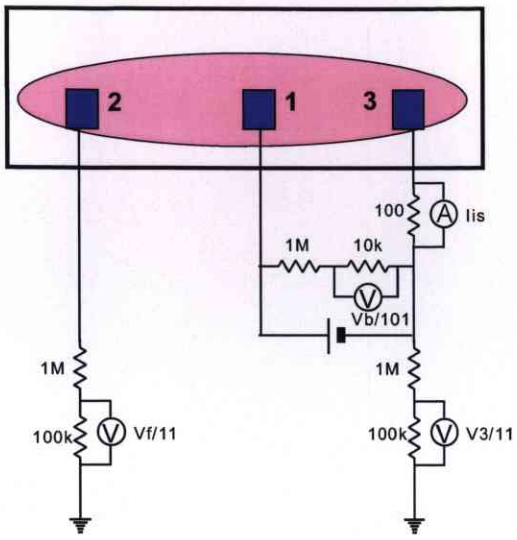

Figure 4.8: The circuit for triple probe measurements.

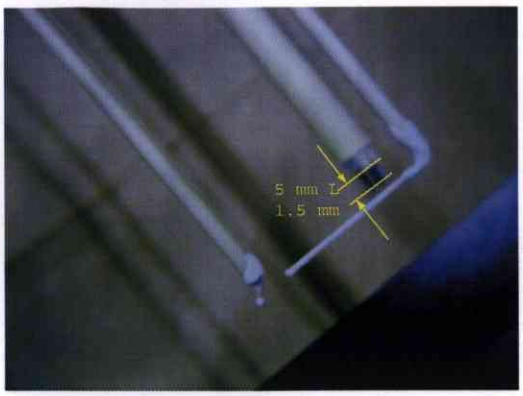

Figure 4.9: A photograph of the triple probe head. Lengths and diameters are 5 and 1.5 mm, respectively.

4.3.2 Transmission Interferometry

Microwave interferometry is untouched method to measure average electron density. Thus, this diagnostic has merit of avoiding perturbation to a plasma. A launching frequency must be sufficiently high not to reflect in a plasma. As shown in the previous chapter, a plasma has permittivity, so that an optical length of a plasma is different from the physical length of it. The variation of the optical length owing to a plasma density can be measured by the variation of the phase, which can be measured by comparison between the phase of the signal wave and that of the reference wave. A refractive index of a plasma for perpendicular propagating wave is written as Eq. (A.61). If the transmitting frequency is much greater than the electron plasma frequency, the ordinary and the extraordinary mode have approximately same refractive index:

$$N^2 = 1 - \frac{\omega_{pe}^2}{\omega^2}. \tag{4.16}$$

And a variation of the optical length is

$$\Delta L = \int \mathrm{d}s(1-N) \sim \int \mathrm{d}s \frac{\omega_{pe}^2}{2\omega^2}, \tag{4.17}$$

where s is a spatial coordinate. Since the square of the electron plasma frequency is proportional to the electron density, the phase variation is proportional to the electron density, i.e.

$$\Delta L = \lambda \frac{\Delta\phi}{2\pi} = \int \mathrm{d}s \frac{e^2 n_e}{8\pi^2 f^2 \epsilon_0 m_e}, \tag{4.18}$$

where $\Delta\phi$ and f denote the phase variation and the transmission frequency. As the result, the line integrated electron density is written as

$$\int \mathrm{d}sn_e = \Delta\phi \frac{4\pi c^2 \epsilon_0 m_e}{e^2 \lambda}, \tag{4.19}$$

where c denotes the speed of the light.

We employed a Mach-Zehnder type interferometry system with 75.308 GHz [22]. The cutoff density of 75.308 GHz wave is $7 \times 10^{19}\mathrm{m}^{-3}$, which is much greater than the electron density in the Mini-RT device. Figure 4.10 shows the block diagram of the interferometry system in the Mini-RT device. This system contains the main, transmission and receiver unit and a mixer for signals. In the main unit, a quarter frequency (18.752 GHz) wave is excited and it is separated into the transmission (signal) and the reference waves. By using this frequency, one can send transmission and reference wave by a co-axial cable. The frequency of the transmission wave is up-converted into 18.827 GHz, i.e. we employed the heterodyne method. Photographs of a main unit are shown in Figs. 4.11 and 4.12. At the transmission unit, frequency multiplier quadruples the transmission frequency, i.e. 75.308 GHz, and it is transmitted by a rectangular waveguide. A horn antenna that has 29 dBi of gain is used for the transmission and the width of it is 60 mm (see Fig. 4.13). The reference wave and the transmission wave are mixed at the receiver unit by a doubler harmonic mixer, and the output signal has 300 MHz. Figure 4.14 is a photograph of the receiver unit. This down-converted (300 MHz) signal is mixed with another reference signal, and the output signal of the interferometer system is written as

$$A\cos(\Delta\phi + \phi_0), \tag{4.20}$$

where A and ϕ_0 denote the amplitude and the initial phase of a signal.

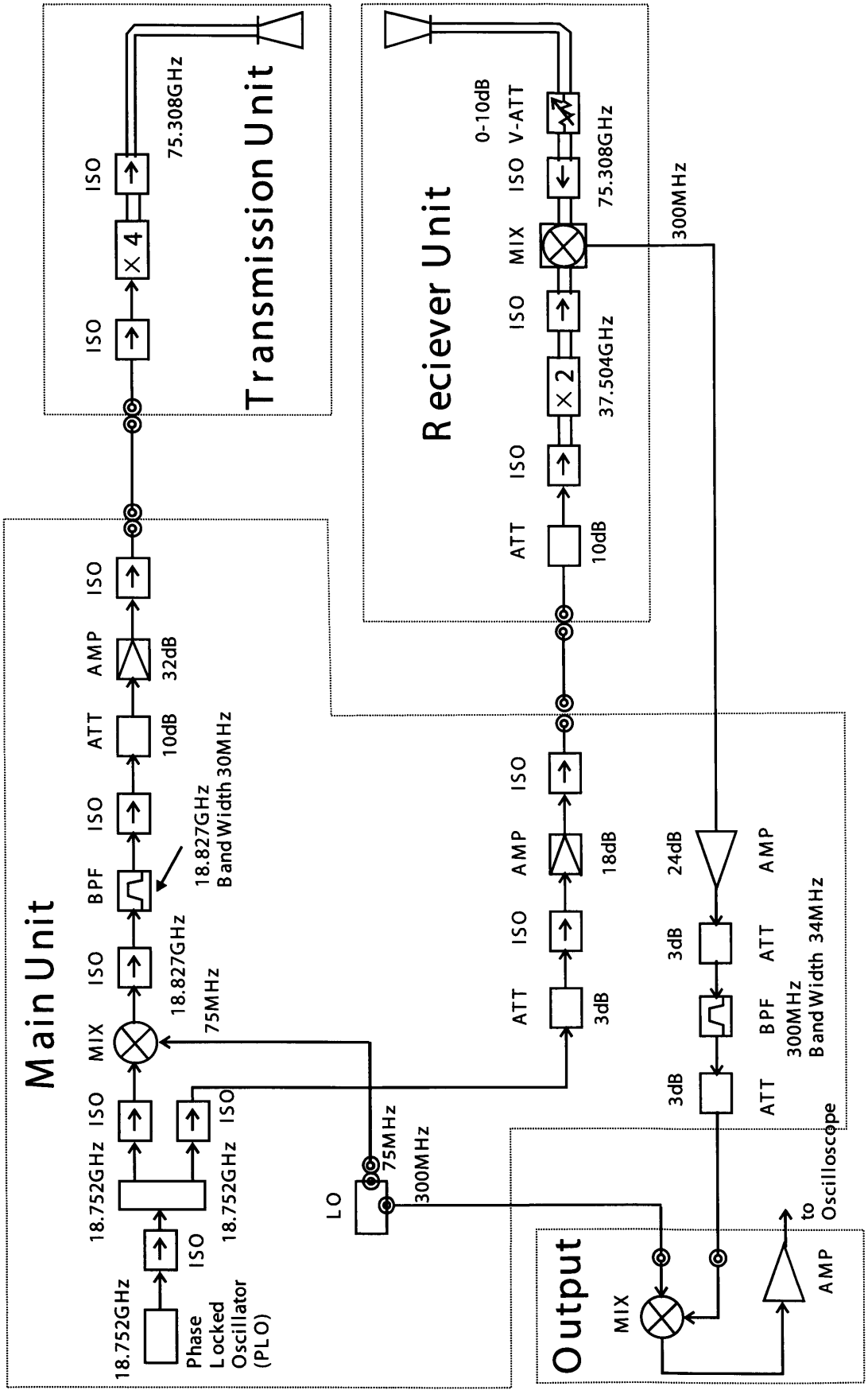

Figure 4.10: The block diagram of the transmitting interferometry circuit.

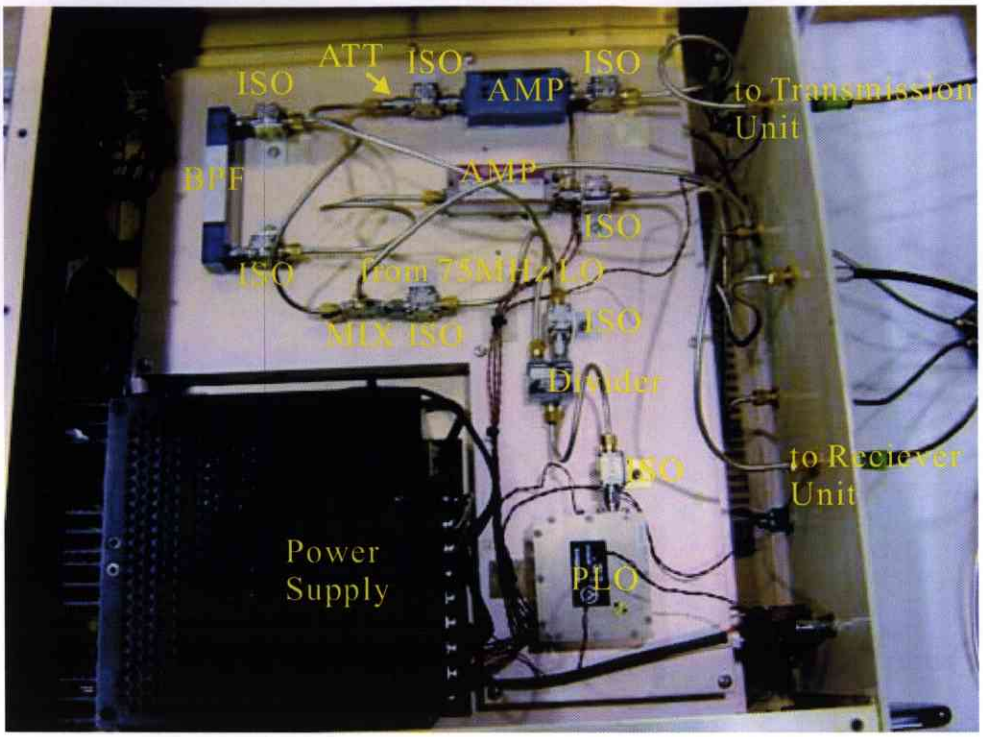

Figure 4.11: Upper side of the main unit.

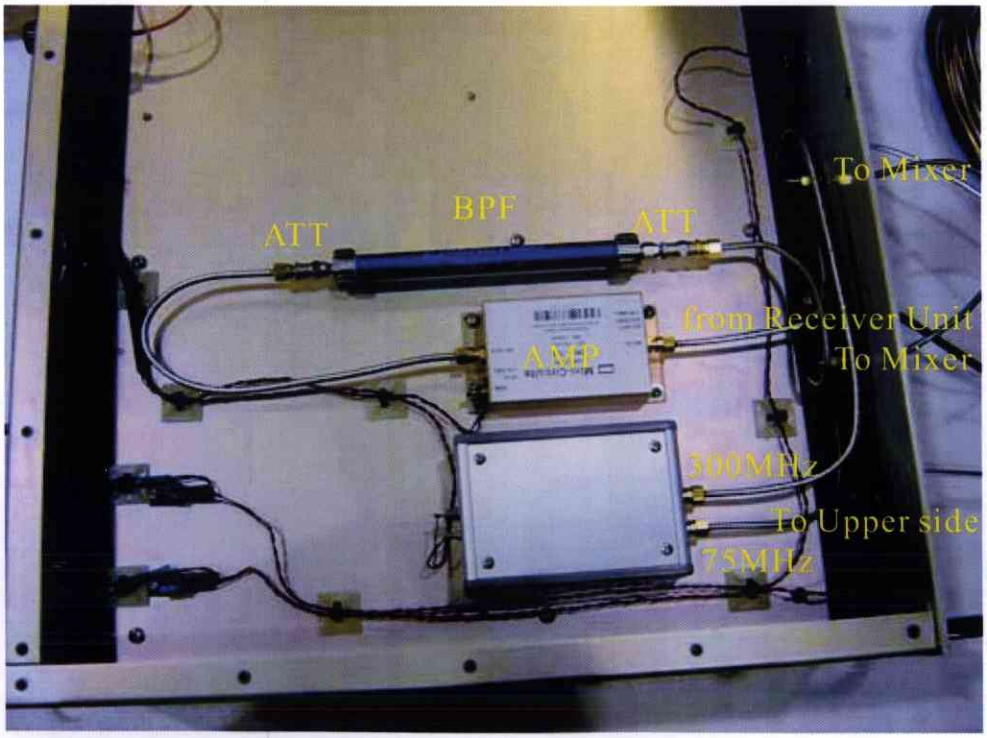

Figure 4.12: Under side of the main unit.

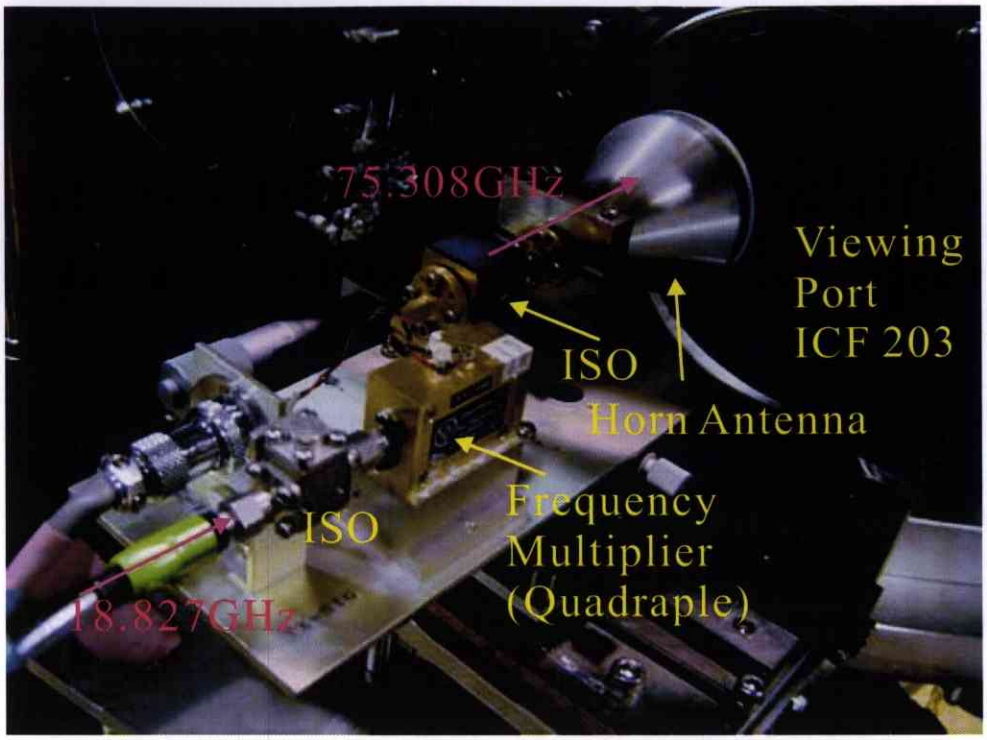

Figure 4.13: A photograph of the transmission unit.

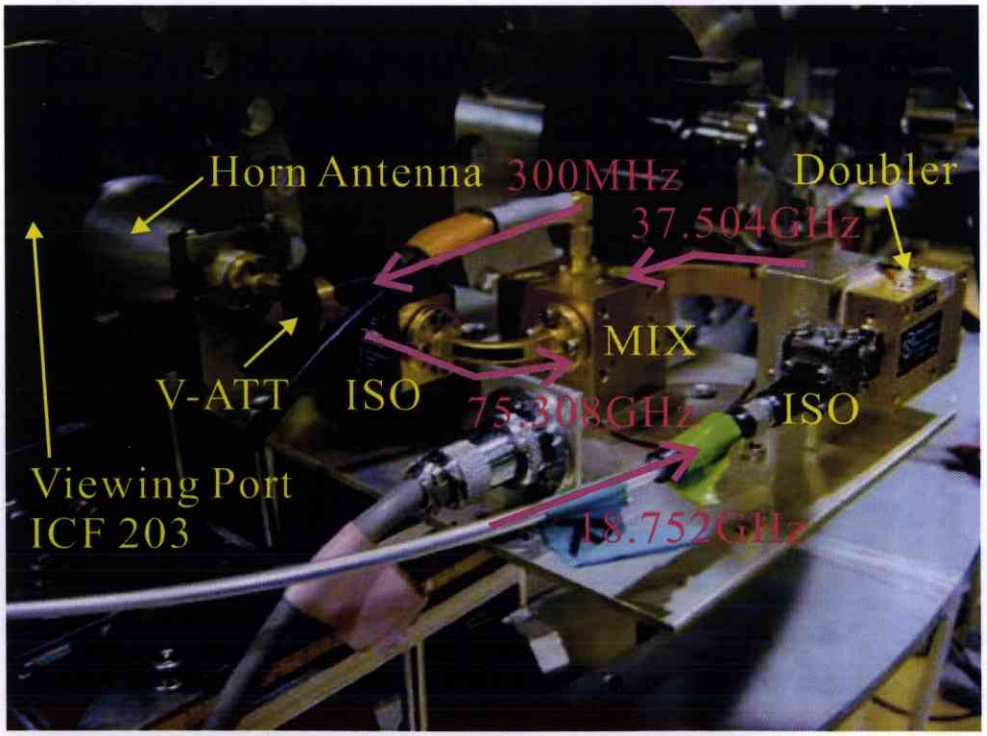

Figure 4.14: A photograph of the receiver unit.

In order to obtain the phase variation experimentally, the amplitude should be investigate before experiments, so that we compared a signal when a plasma is produced with it in vacuum. Figure 4.15 shows an example of output data, which shows that the amplitude is 201 mV and wavelength is 4.0 mm, i.e. this coincides the wavelength of a 75 GHz electromagnetic wave in vacuum. Figure 4.16 shows a typical data for interferometer measurements; electron density is decreased when a triple probe and antennas are inserted deeply in plasma. About 10% of a density decrement does not seem to affects essentialy to the plasma confinement.

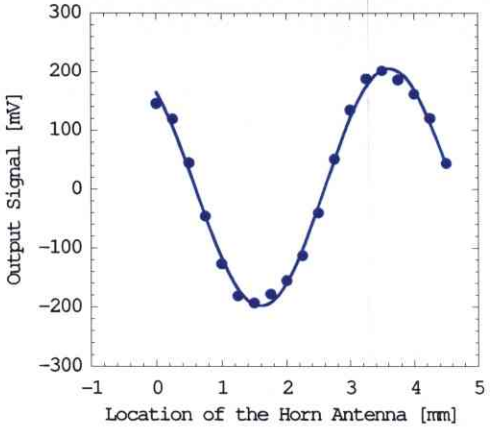

Figure 4.15: Relationship between output signals and the location of the horn antenna.

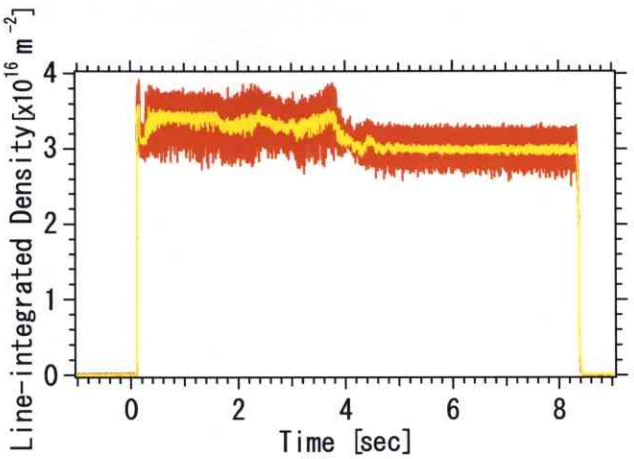

Figure 4.16: An example of line-integrated electron density measurement data.

4.3.3 Comparison between the Triple probe and the Transmitting Interferometry Measurements

Density measurements by a triple probe was compared with the interferometry ones. Density profiles are integrated through the interferometry paths by assuming plasma densities are toroidally symmetric. Fig. 4.17 shows the integral scheme of electron density, i.e.

$$\int n_e \mathrm{d}x = 2 \sum_i [\{\frac{n_e(\theta_i) + n_e(\theta_{i-1})}{2}\}\{r_{i-1}\cos(\theta_{i-1}) - r_i \cos(\theta_i)\}], \qquad (4.21)$$

where r_i denoted the radial position at which a triple probe measured.

Figures 4.18 and 4.19 compare the line integrated electron density that were measured by an interferometer and a triple probe with the simple dipole configuration and the separatrix configuration, respectively. The horizontal axises denote the radial position of the interferometry paths at the mid-plane. The legend 'triple probe' means an electron density integrated

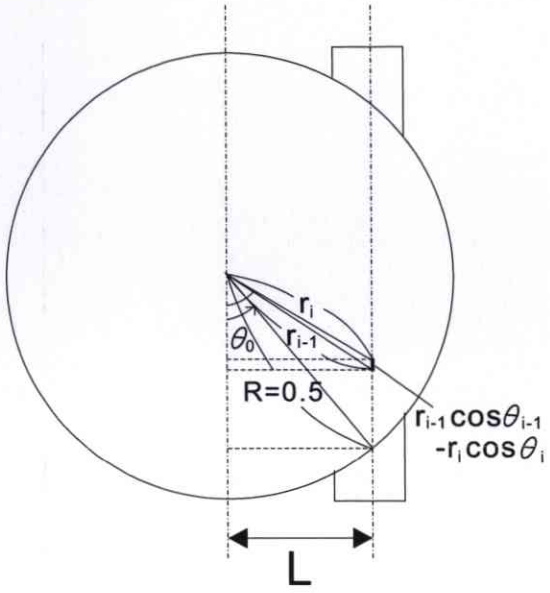

Figure 4.17: The scheme of the integral of density profiles through a path of the interferometry.

on each corresponding interferometry path. In both configurations, electron density which is measured by interferometry tends to greater than that by a triple probe. The discrepancies of them is up to 50%.

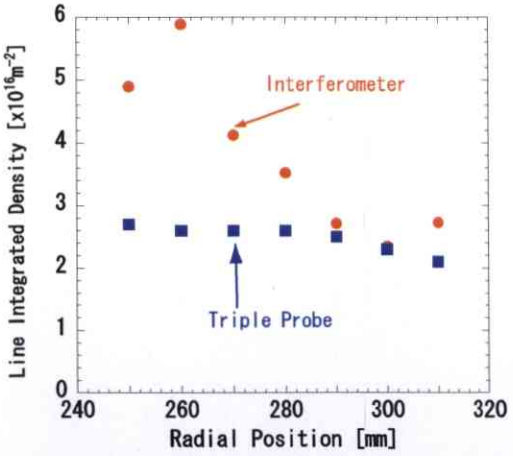

Figure 4.18: Electron density measurements with the simple dipole configuration.

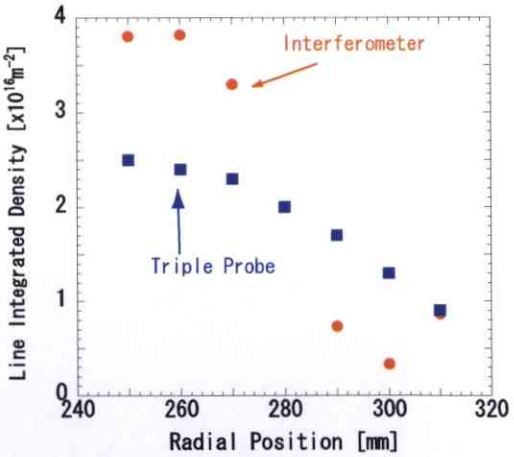

Figure 4.19: Electron density measurements with the separatrix configuration.

The reasons why there are such discrepancies have not been verified yet; there are a number of possibilities of it. The toroidal asymmetry may cause this discrepancy, e.g. the mechanical

support structures locally cool plasma, and the ECH launcher for a plasma production lies above the interferometry paths. The distribution function also affects the electron density measurements because a triple probe measures a part of i-v characteristics. If high energy electrons are produced, electron density may look like smaller because the apparent electron density increases and the apparent ion saturation current decreases. Figure 4.20 shows the i-v characteristics of signal (red line) and double (blue one) temperature plasma. It was assumed the temperature and fraction of high energy electrons are $10T_e$ and 10%, respectively. The shape of triple probe tips also affects the ion saturation current due to the increasing of collection area with the bias voltage, i.e. this effect may increase the apparent electron density of probe measurements.

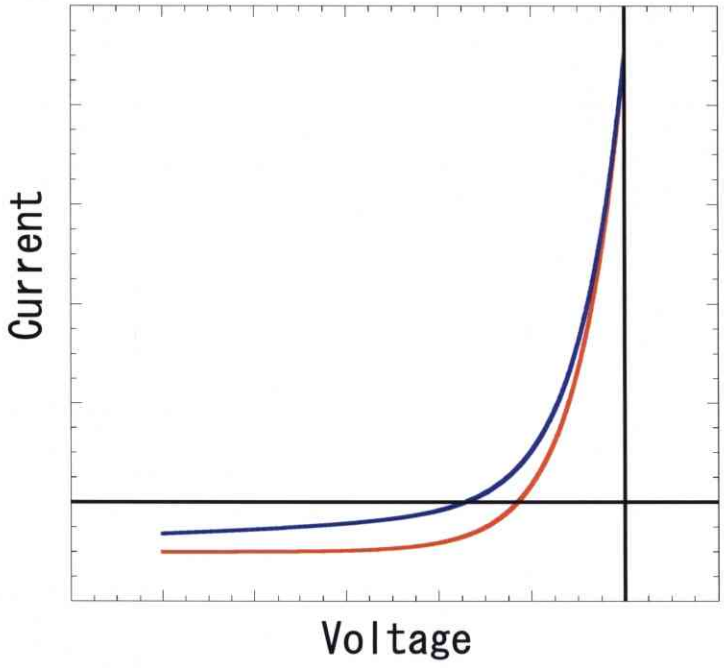

Figure 4.20: Current voltage characteristics with a single temperature plasma and a double temperature plasma. The red line corresponds to the plasma with temperature of T_e, whereas the blue one corresponds to the plasma which contains 10 percents of hot ($10T_e$) electrons.

Although a triple probe and an interferometer do not provide consistent results, hereafter, electron density profiles measured by a triple probe and line integrated electron density measured by interferometer are used without correction. One should remind these results do not exhibit absolute values.

Chapter 5

Heating Property on Mini-RT

5.1 Experiments when the Internal Coil is Supported

5.1.1 The Magnetic Field Configurations

Magnetic field configurations determine the location of the separatrix, which restricts a plasma confinement region. Figures 5.1-5.3 show the profiles of an electron density, a bulk electron temperature and a bulk electron pressure. Heating power is 2.5 kW, filling gas pressure is 44 mPa and the internal coil current is 34 kA, respectively. The shape of electron density profile is spread when the levitation coil current is decreased. The density gradient scale length is almost a constant, i.e. 20 mm inside the separatrix and 50 mm outside the separatrix. A typical value of bulk electron temperature is increased when a plasma confinement region shrinks. As the result, a bulk electron pressure has a local peak around the separatrix.

Here let the pressure profiles be normalized, i.e. pressure is normalized by the local peak value that lies around the separatrix, and the radial coordinate is replaced by the normalized flux surface coordinate, which is defined as

$$\tilde{\psi} = \frac{\psi_1 - \psi}{\psi_1 - \psi_2}, \tag{5.1}$$

where ψ, ψ_1 and ψ_2 denote a flux surface coordinate, it at the surface of the floating coil and it at the separatrix, respectively. A flux surface coordinate ψ is defined by

$$\psi = rA_\phi(r, z), \tag{5.2}$$

where A_ϕ is a vector potential, and this form of ψ can be used in the toroidally symmetric systems. Figure 5.4 shows the normalized pressure profiles when the levitation coil current has

various values. One can see the shape of them are essentially similar and the density gradient scale lengths change at $\tilde{\psi} = 1$, which corresponds to the separatrix. The position of the separatrix is determined from the vacuum magnetic field.

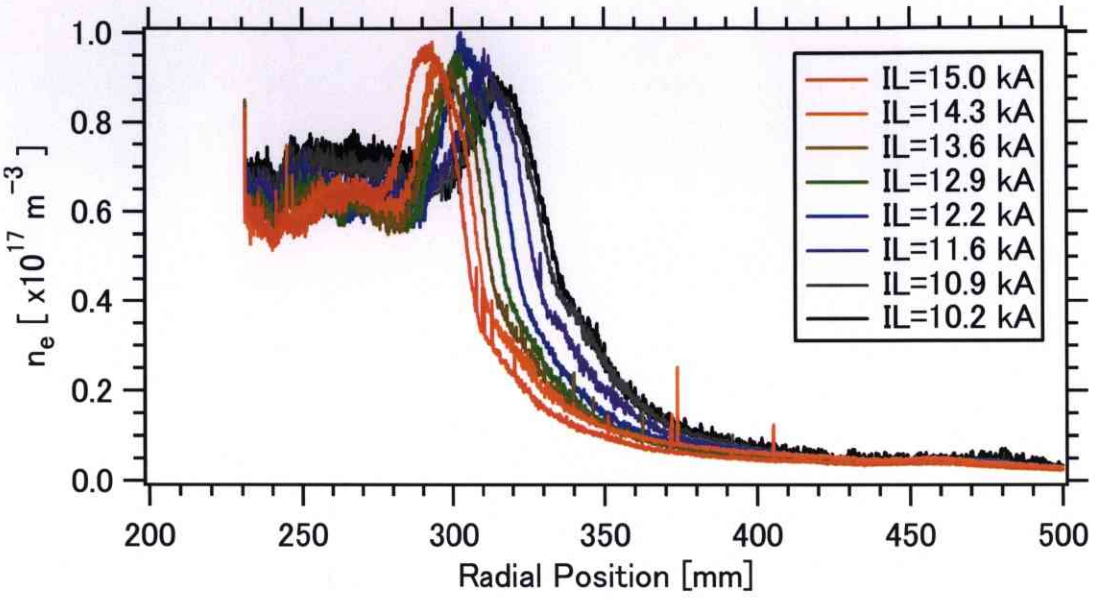

Figure 5.1: Configuration dependence of an electron density profile. There is a steep density gradient region around the separatrix.

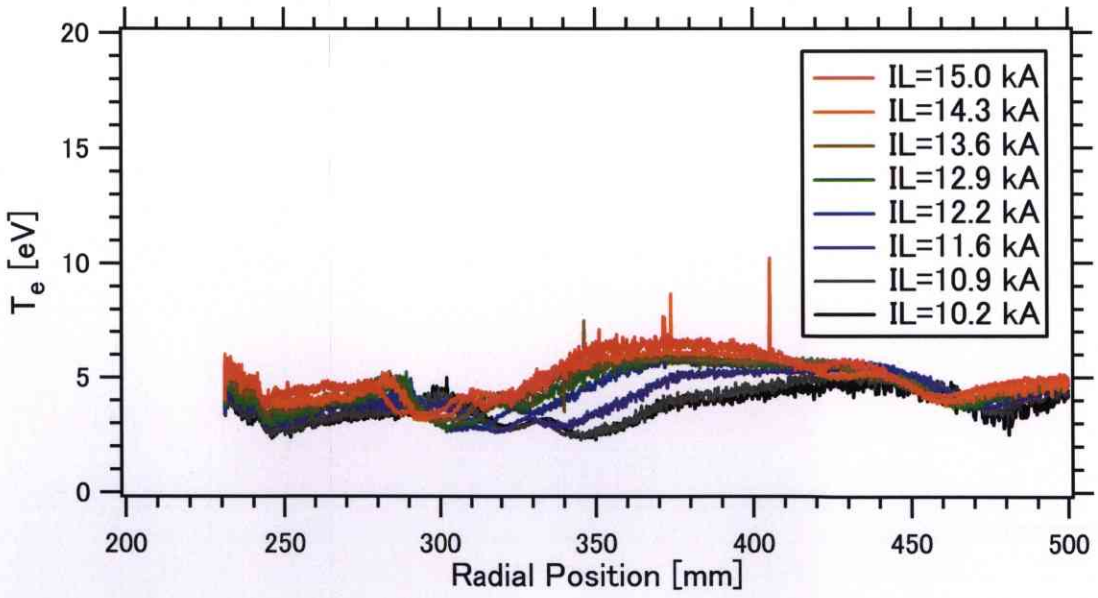

Figure 5.2: Configuration dependence of a bulk electron temperature profile. It is approximately uniform and increases with the shrinking of the plasma confinement region.

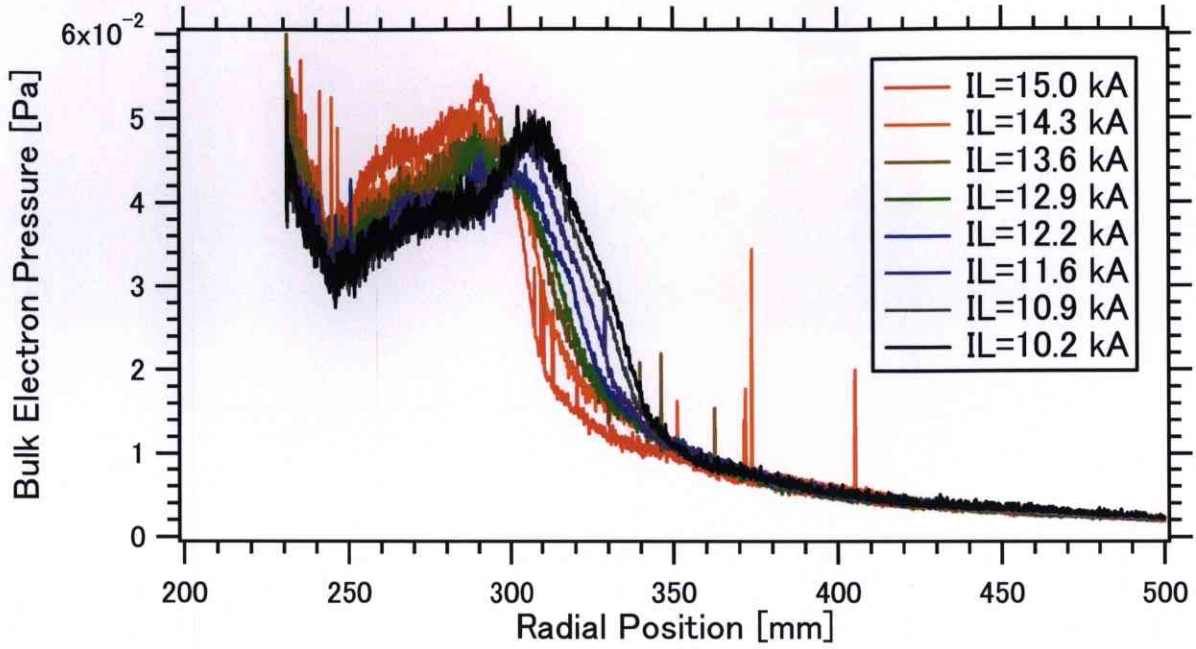

Figure 5.3: Configuration dependence of a bulk electron pressure profiles. Similarly to density profiles, there are steep gradient regions around the separatrix.

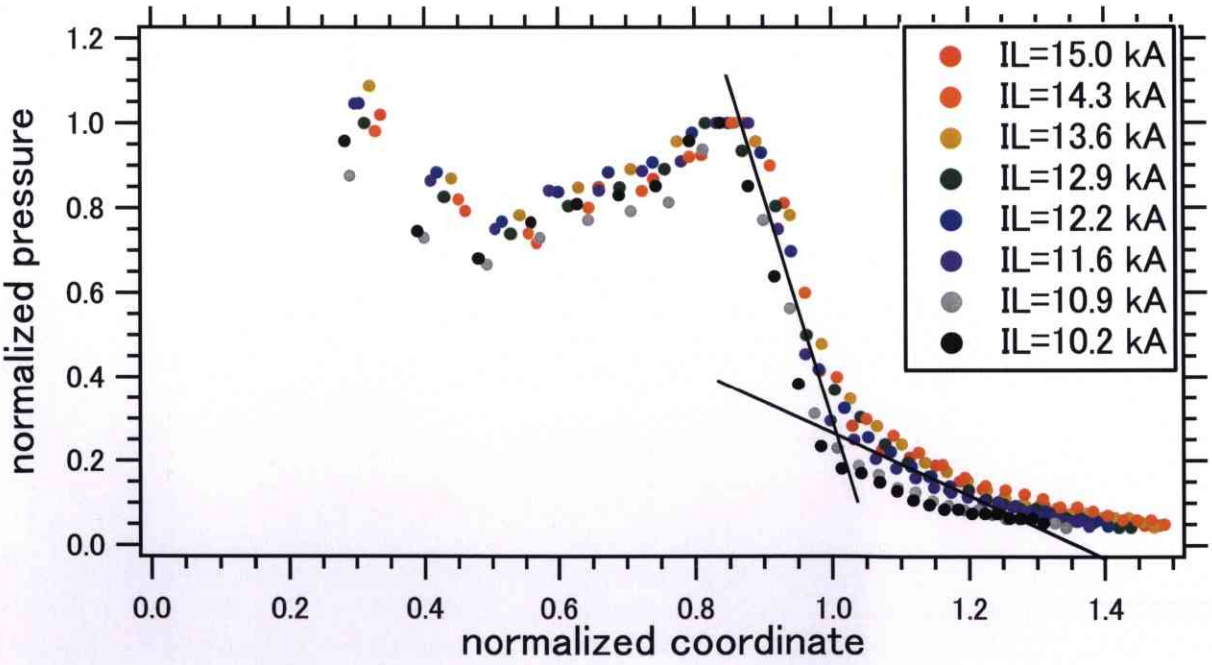

Figure 5.4: Configuration dependence of a normalized pressure profile with respect to the flux coordinate. The scale lengths of the density gradient are drastically changed at the separatrix, which corresponds to $\tilde{\phi} = 1$.

5.1.2 The Heating Power Dependence

The heating power affects a stored energy in a plasma. Thus one can infer the plasma pressure increases with increasing of a heating power. Figure 5.5-5.7 show the density, temperature and pressure profiles, respectively, where the levitation coil current I_L is 13.6 kA, i.e. the location of the separatrix is $R = 311$ mm at the mid-plane. The filling gas pressure is fixed to 44 mPa. The existence of two discharge modes are suggested like the L and H modes, which has a threshold heating power [77]. Sufficiently high power heating causes the steep density gradient around the separatrix and relatively high density inside of the plasma, whereas the low power heating causes almost flat density profiles. The heating power does not seem to affect electron temperature profiles when a plasma has a steep density gradient around the separatrix. The low density discharge has a relatively high bulk electron temperature. However the pressures are not proportional to a heating power, especially relatively high heating power gets the electron pressure be saturated.

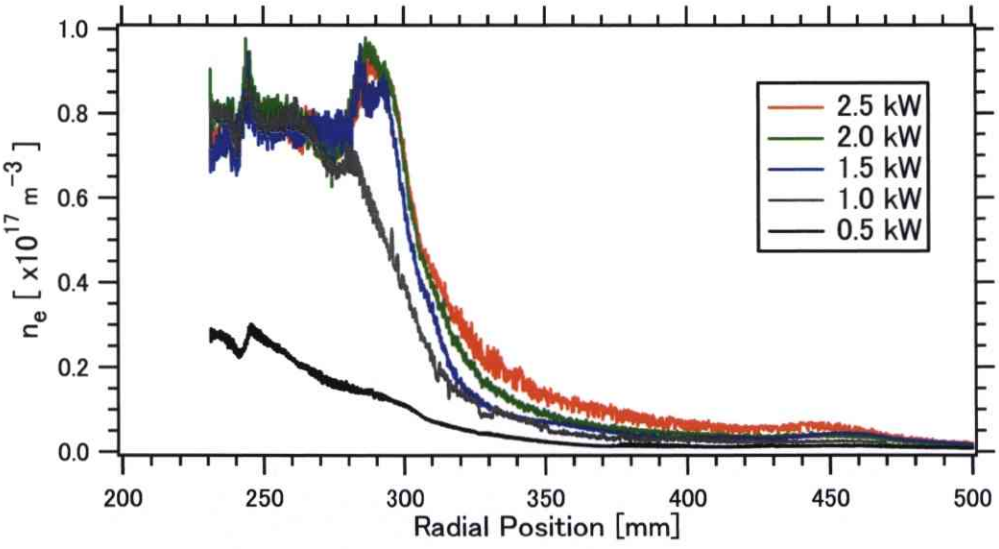

Figure 5.5: ECH power dependence of an electron density profile when the levitation coil current I_L is 13.6 kA.

Similar properties are observed on various magnetic configurations. Figures 5.8 and 5.9 show the density profiles when the levitation coil current I_L is 6.8 kA and 0 kA, respectively. Threshold heating power increases with spreading of the plasma confinement region. Moreover 2.5 kW case in Fig. 5.9 shows the transition between the high density discharge and the low density one during the insertion of a triple probe. In the high density discharge, the electron density triples and electron temperature slightly decreases (approximately halves).

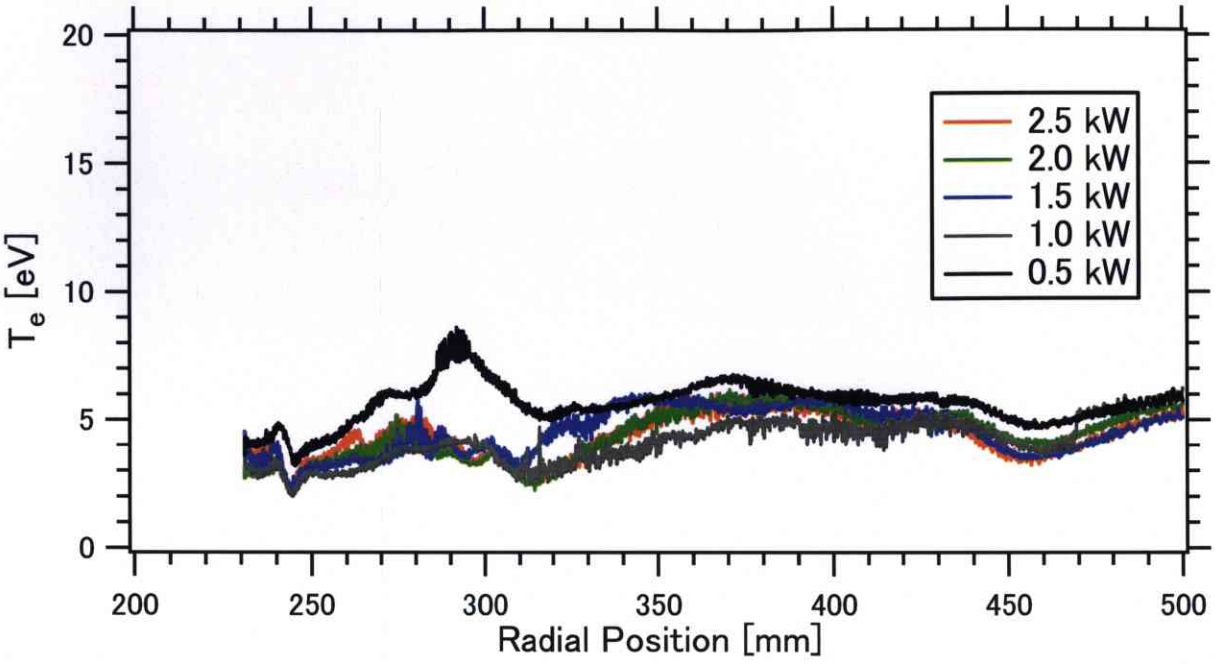

Figure 5.6: ECH power dependence of a bulk electron temperature profile when the levitation coil current I_L is 13.6 kA.

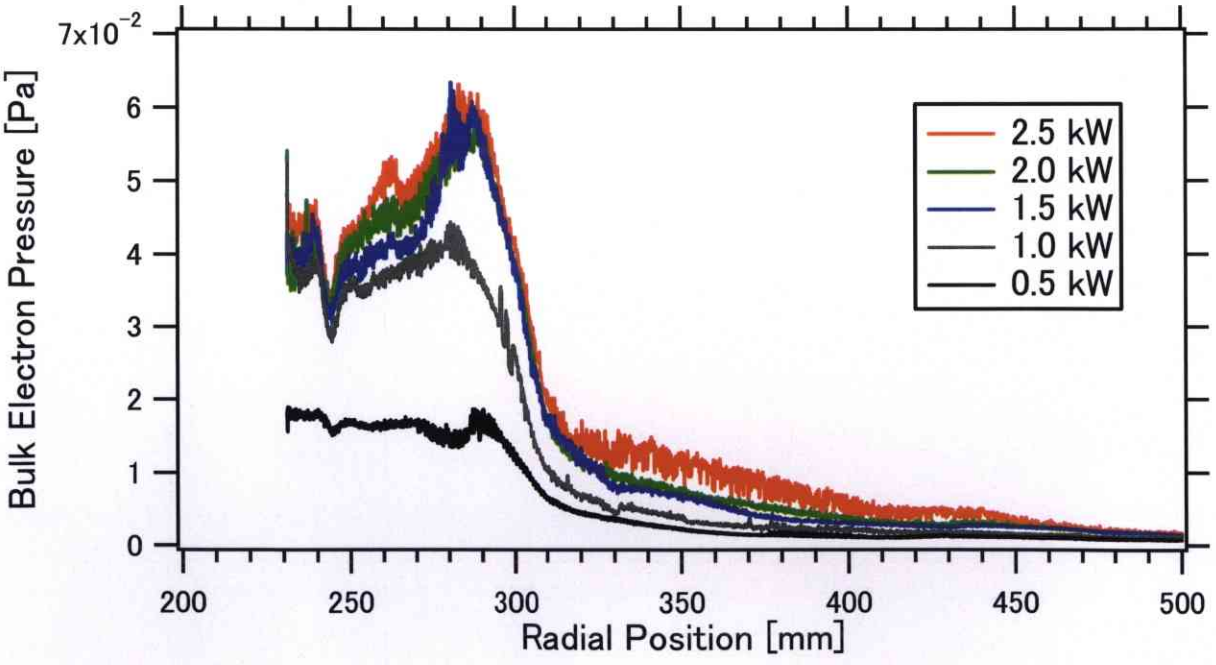

Figure 5.7: ECH power dependence of a bulk electron pressure profiles when the levitation coil current I_L is 13.6 kA.

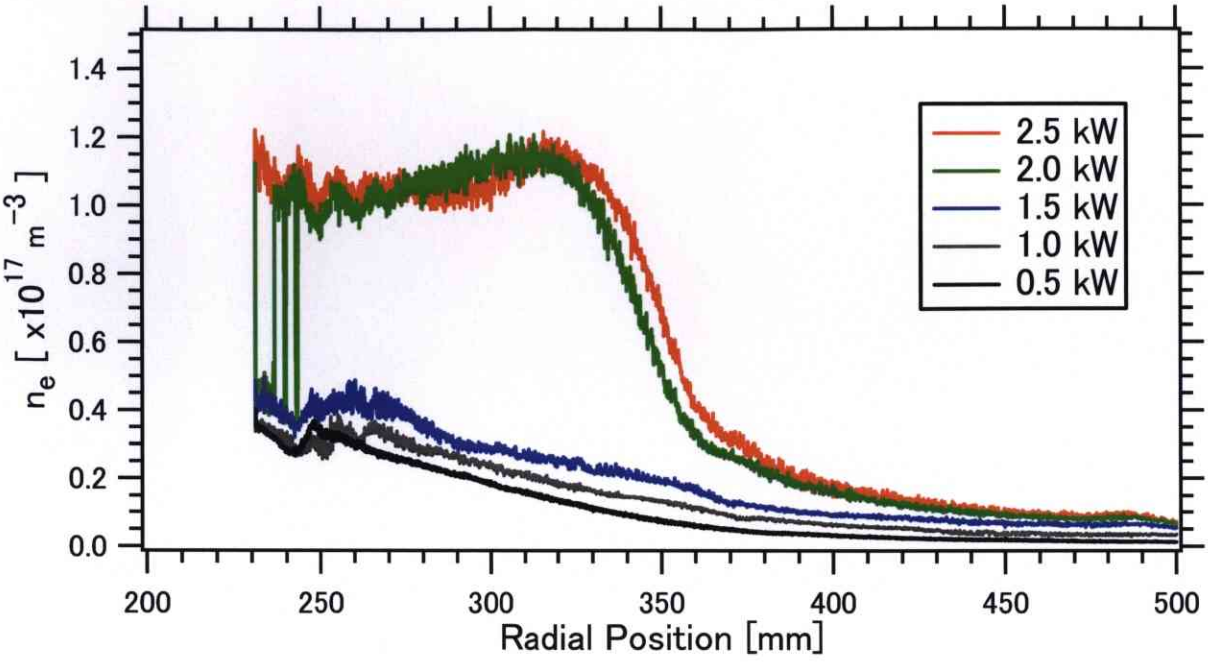

Figure 5.8: ECH power dependence of electron density profiles when the levitation coil current I_L is 6.8 kA.

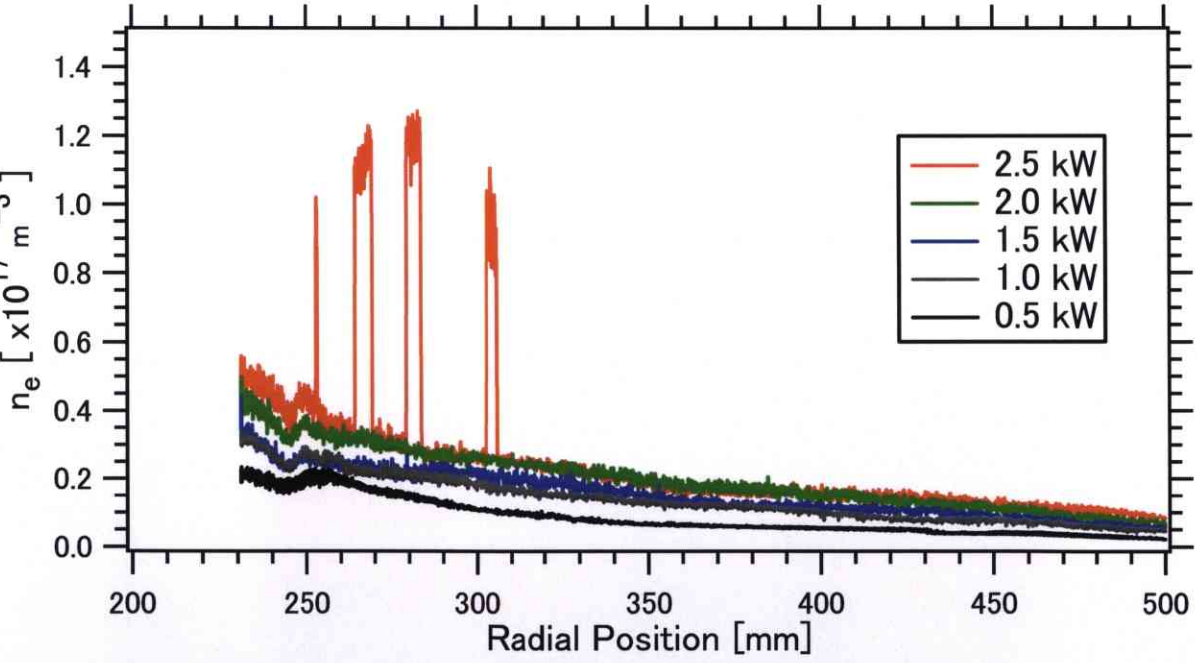

Figure 5.9: ECH power dependence of electron density profiles when the levitation coil current I_L is 0 A.

The density transition were investigated by an interferometer. Figure 5.10 shows a typical discharge of this investigation. The density transition occurs when the injection power goes beyond 2.0 kW. Here currents of the internal coil and the levitation coil are 22 kA and 8.2

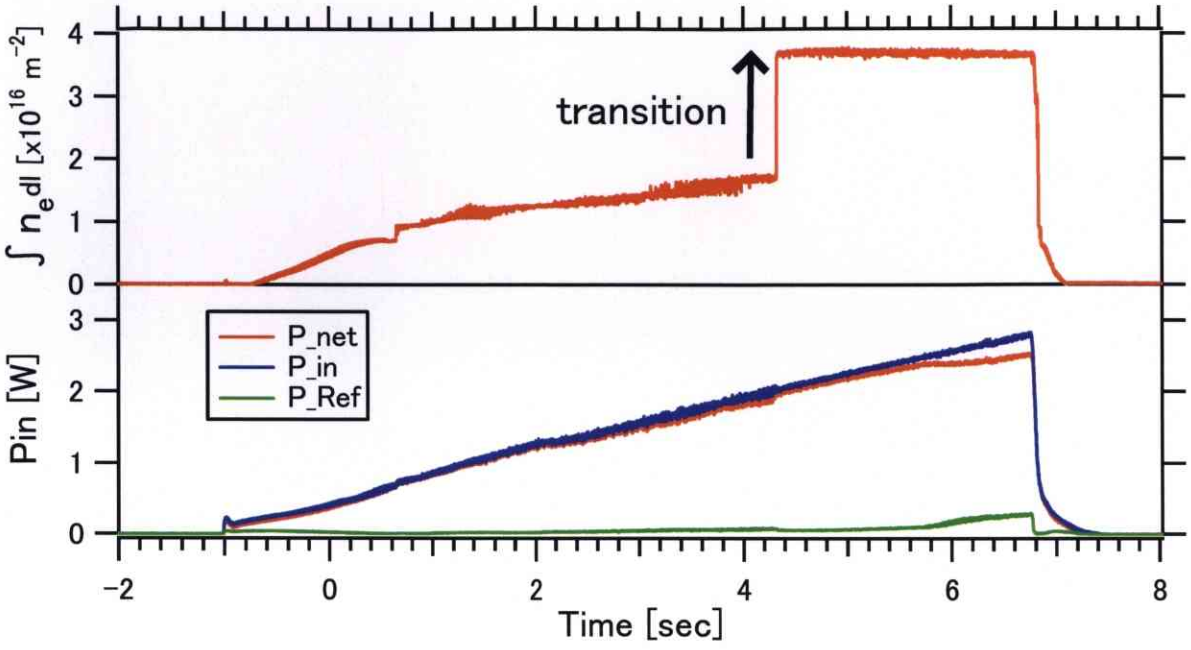

Figure 5.10: Density transition when the injected ECH power goes beyond a threshold value.

kA, respectively. The time constant of the transition is 3 ms. Moreover one can see the line integrated density is saturated after the transition. Details of a transition phenomena is beyond the scope of this research; however, it may be important that the transition, which were observed in many fusion oriented device like a tokamak and a stellarator, was observed in a dipole confined plasma. Figure 5.11 shows the configuration dependence of the density transition. The threshold power increases when a plasma confinement region spreads. Although current of the internal coil in these experiments (22 kA) were smaller than that in experiments of Figs. 5.5 and 5.8 (34 kA), threshold power was not varied so much.

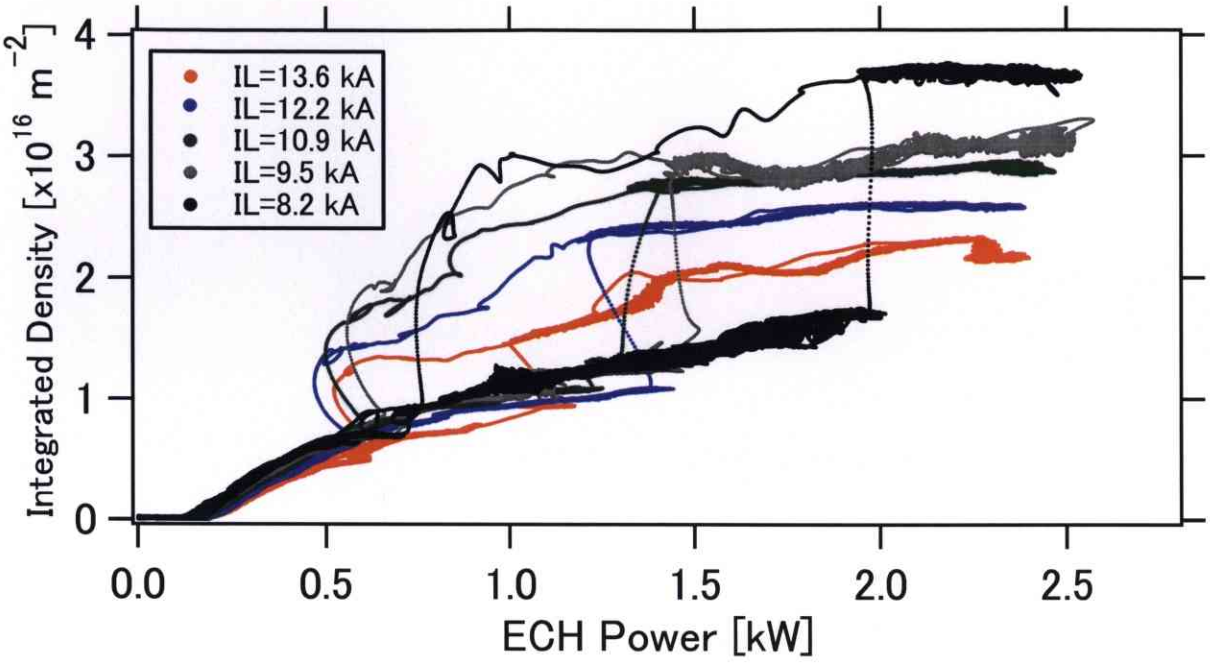

Figure 5.11: Configuration dependence of a transition. Threshold power increases when a plasma confinement region spreads.

5.1.3 Effects of Neutral Gas Pressure

The neutral gas pressure affects the cross section of ionization and recombination. Figures 5.12-5.14 show the profiles of electron density, electron temperature and electron pressure, respectively. The neutral gas pressure is measured by an ionization gage at the upstream of the vacuum pumps. And the levitation coil current I_L and heating power are 13.6 kA and 2.5 kW, respectively. A low neutral pressure causes a centrally peaked density profile. And electron temperature decreases when the neutral pressure is high.

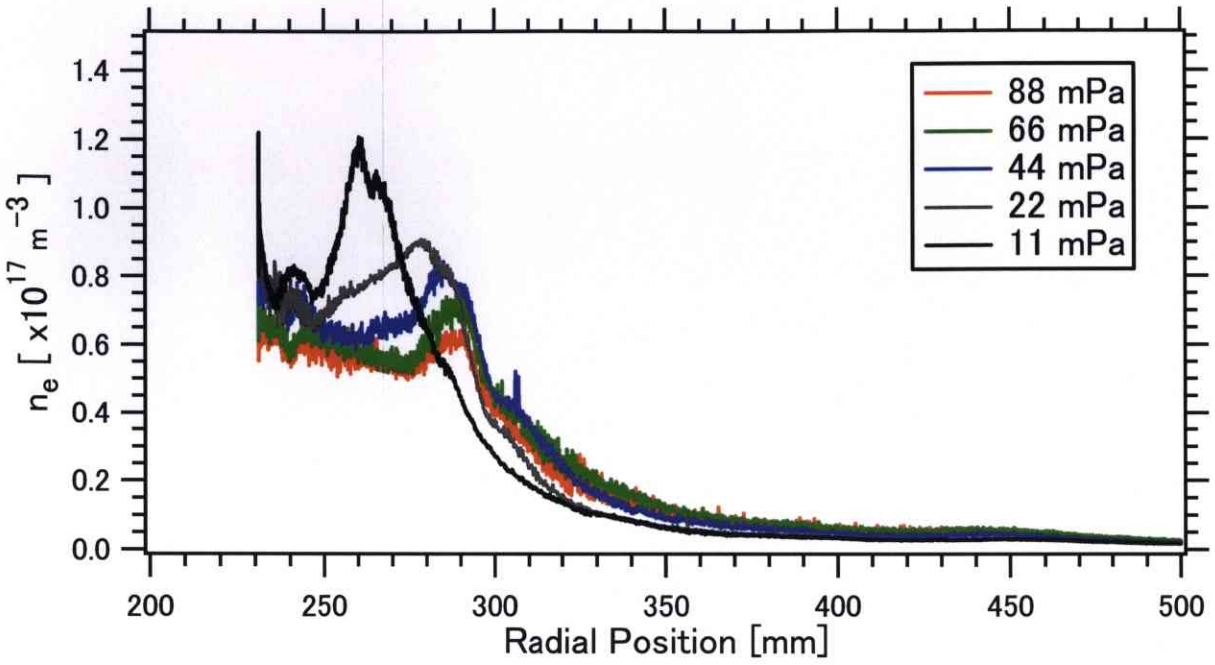

Figure 5.12: Neutral gas pressure dependence of an electron density profile.

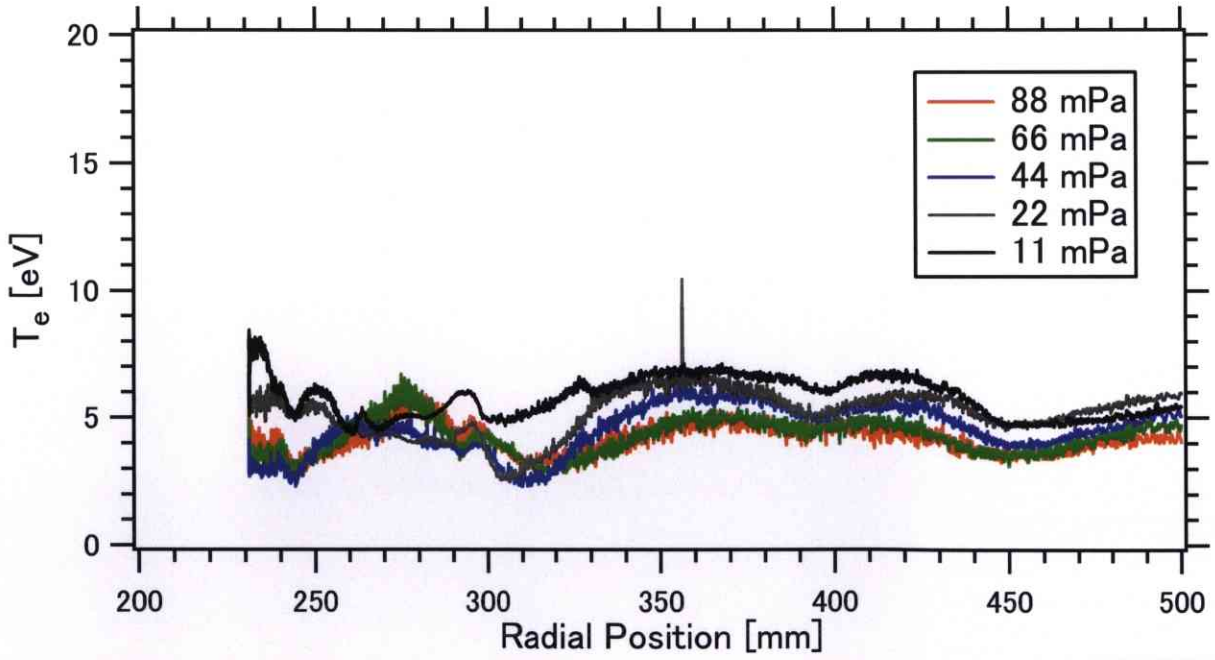

Figure 5.13: Neutral gas pressure dependence of a bulk electron temperature profile.

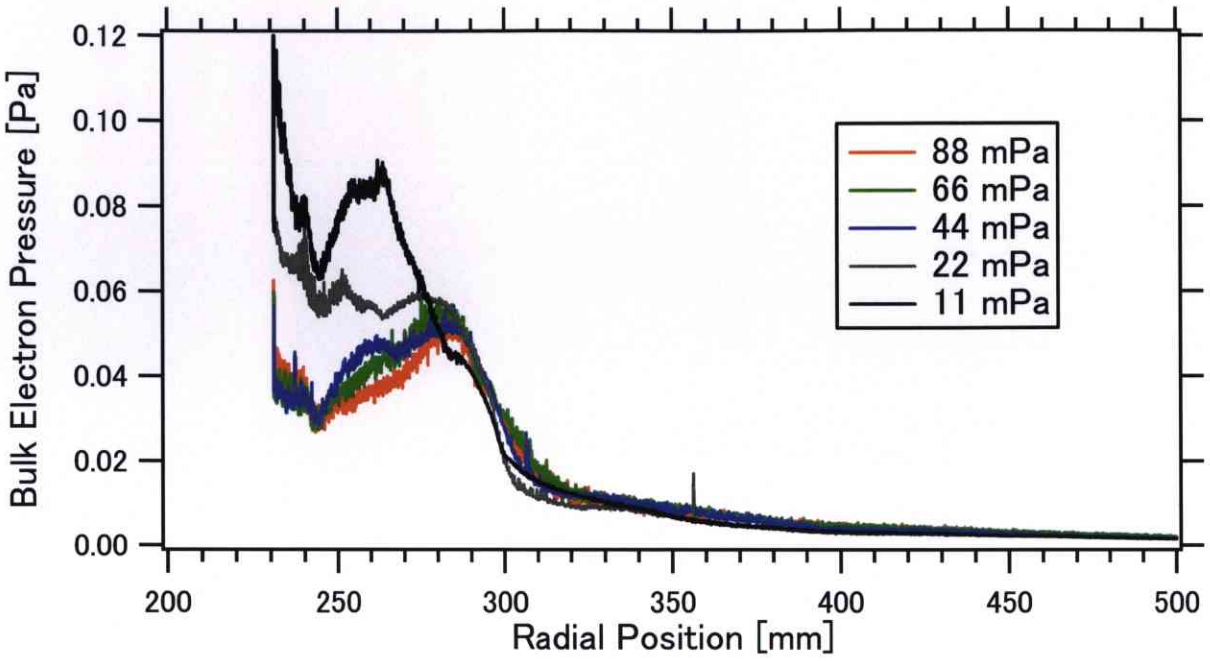

Figure 5.14: Neutral gas pressure dependence of a bulk electron pressure profile.

5.1.4 The Gas Species

Hydrogen and helium show the different properties of atomic processes, so that electron density and temperature profiles may differ. Figures 5.15-5.17 show the profiles of electron density, electron temperature and pressure with different (hydrogen and helium) working gases, respectively. Here we assumed the helium ions contain only the singly-charged ions, i.e. He^{2+} does not exist, that is consistent with the optical measurements of visible lights in Mini-RT by D. Sakata [64]. An electron density profile of a hydrogen plasma tends to be greater than that of a helium plasma. This seems to be due to the high ionization potential of noble gases. On the other hand, an electron temperature profile of a hydrogen plasma tends to be smaller. As the result, an electron pressure profile of a hydrogen plasma is smaller than that of a helium plasma. The reason why there are differences of density and temperature profiles between hydrogen and helium plasmas is beyond the scope of this thesis; however, we can guess an electron temperature is positively correlated with the ionization or dissociating energy in weakly ionized plasmas. The ionization energies of hydrogen and helium atoms are 13.598 eV and 24.587 eV, respectively. Thus one can expect helium plasmas have higher temperature and lower density values than hydrogen plasmas with same discharge conditions.

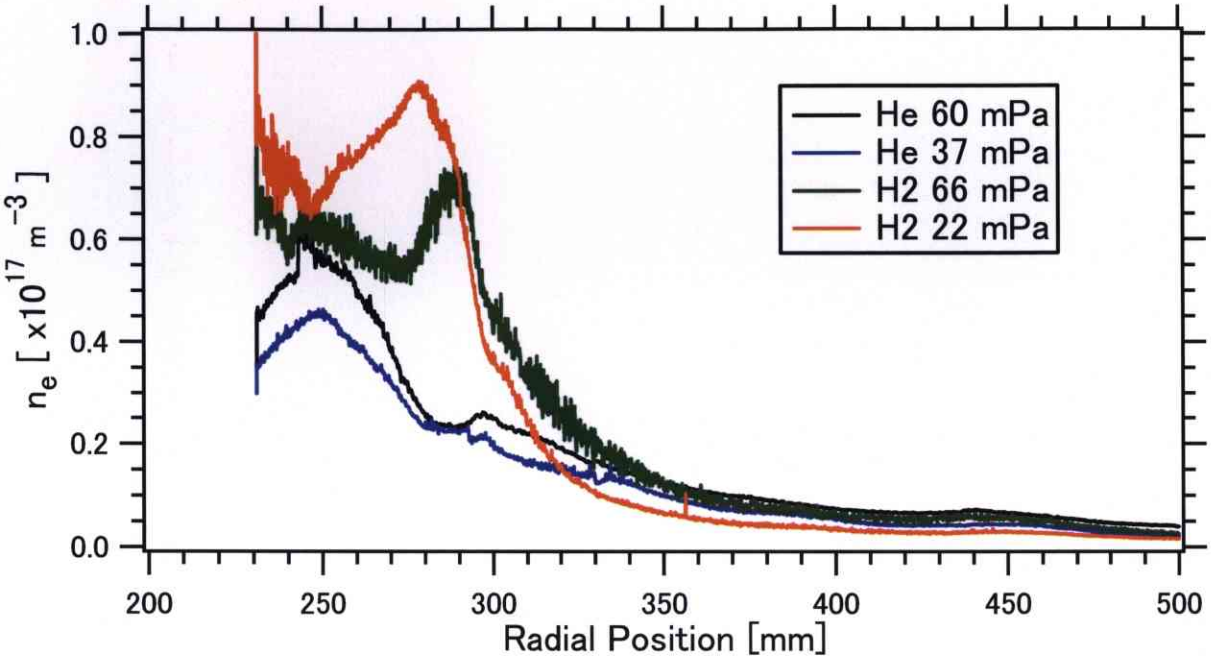

Figure 5.15: Working gas dependence of an electron density profile.

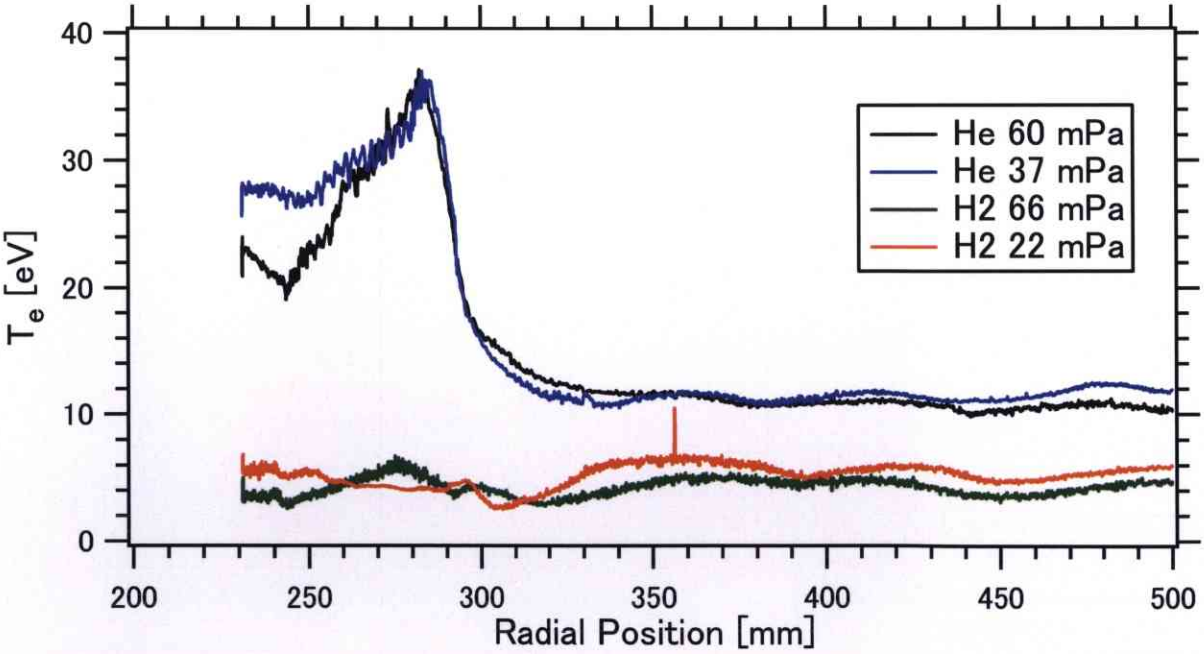

Figure 5.16: Working gas dependence of a bulk electron temperature profile.

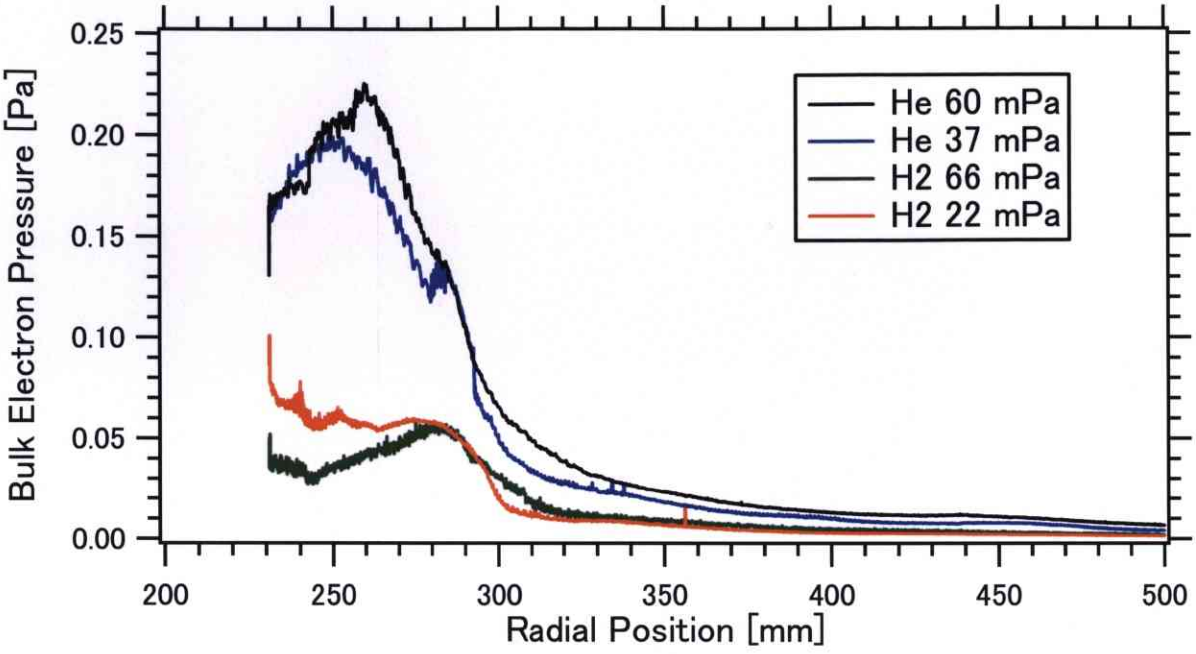

Figure 5.17: Working gas dependence of a bulk electron pressure profile.

5.1.5 An Injection Mode

If the one-path absorption rate is sufficiently high, a direction of polarization of an injected electromagnetic wave is crucial for a plasma heating property, i.e. the electron density and temperature profiles. Figure 5.18-5.20 show the injection mode dependence of the profiles of electron density, electron temperature and electron pressure with the separatrix configuration, respectively. The experimental conditions are slightly different, i.e. currents of the levitation and the internal coil are 15.0 kA and 30.8 kA, respectively, at the O-mode injection, whereas 13.6 kA and 30.4 kA at the X-mode injection, respectively. The density gradient scale lengths are almost same for both injection modes. In addition, a value of an electron densities slightly differ. While, an electron temperature at the O-mode injection approximately doubles it at X-mode injection. As the results, an electron pressure at the O-mode injection tends to be higher than it at X-mode. Moreover, the case when 0.5 kW O-mode injection looks like good confinement discharge that is discussed in Sec. 5.1.2.

In the simple dipole configuration, electron density profiles do not differ between the O-mode injection and the X-mode one except for the experiments when the heating power is 2.5 kW (see Figs. 5.21-5.23). Electron temperature profiles behave like the experiments in the separatrix configuration, i.e. the O-mode injection exhibits relatively high temperature

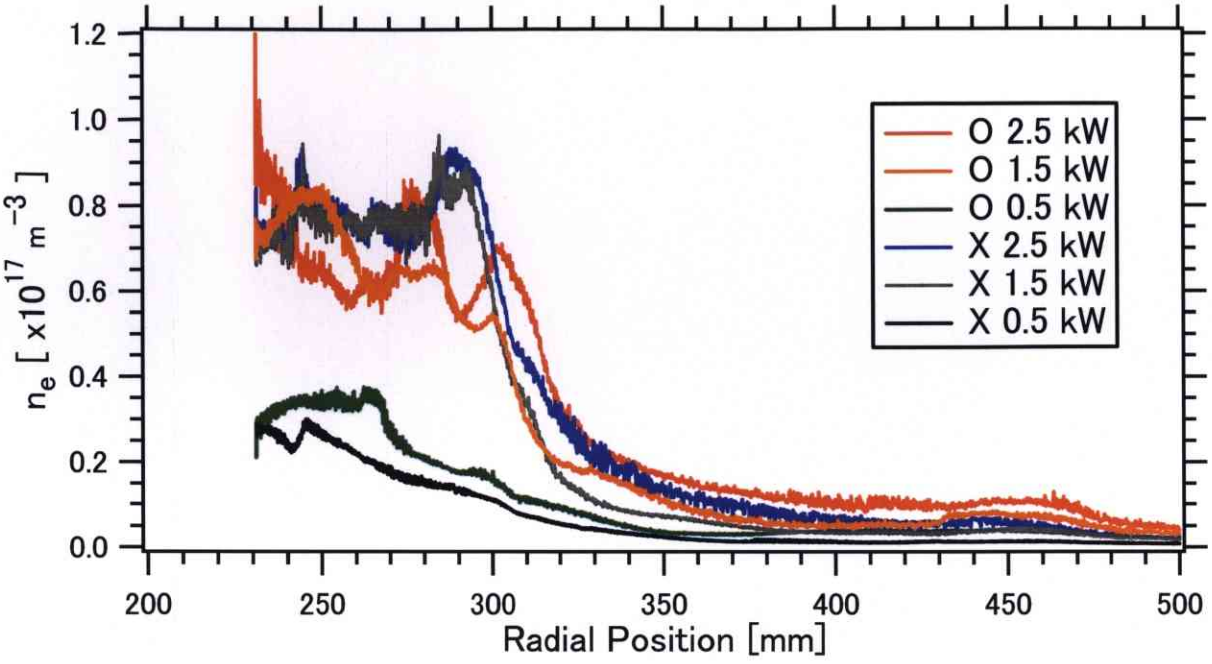

Figure 5.18: Injection mode dependence of an electron density profile with the separatrix configuration.

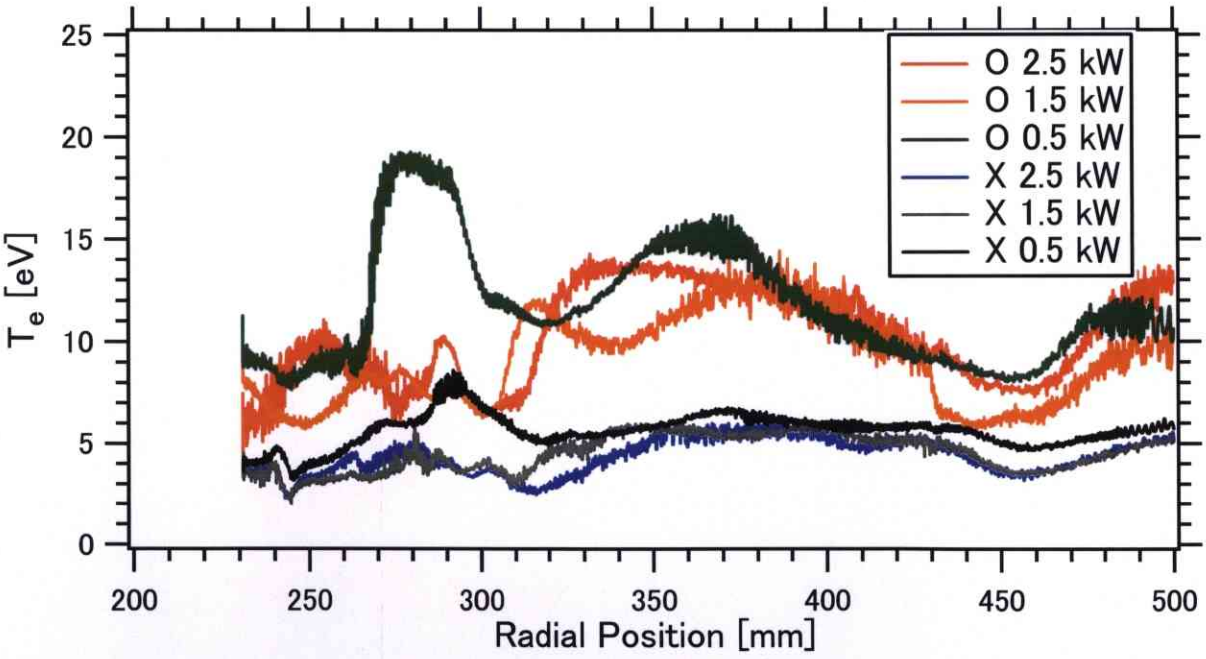

Figure 5.19: Injection mode dependence of a bulk electron temperature profile with the separatrix configuration.

plasma, so that electron pressure profiles with the O-mode injection are greater than that of the X-mode injection. However, note that the floating coil current, i.e. the magnetic field strength for plasma confinement, differs. For the O-mode injection it was 31.7 kA, whereas

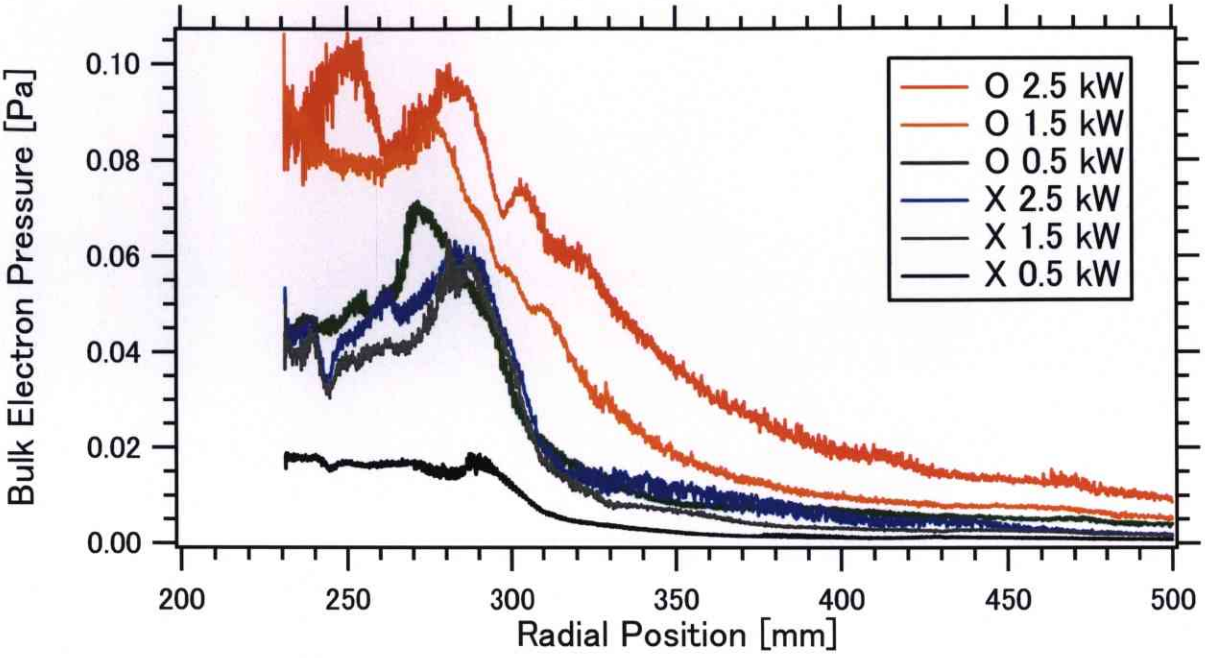

Figure 5.20: Injection mode dependence of a bulk electron pressure profile with the separatrix configuration.

27.0 kA for the X-mode injection, this 15% of difference might cause the differences of some profiles.

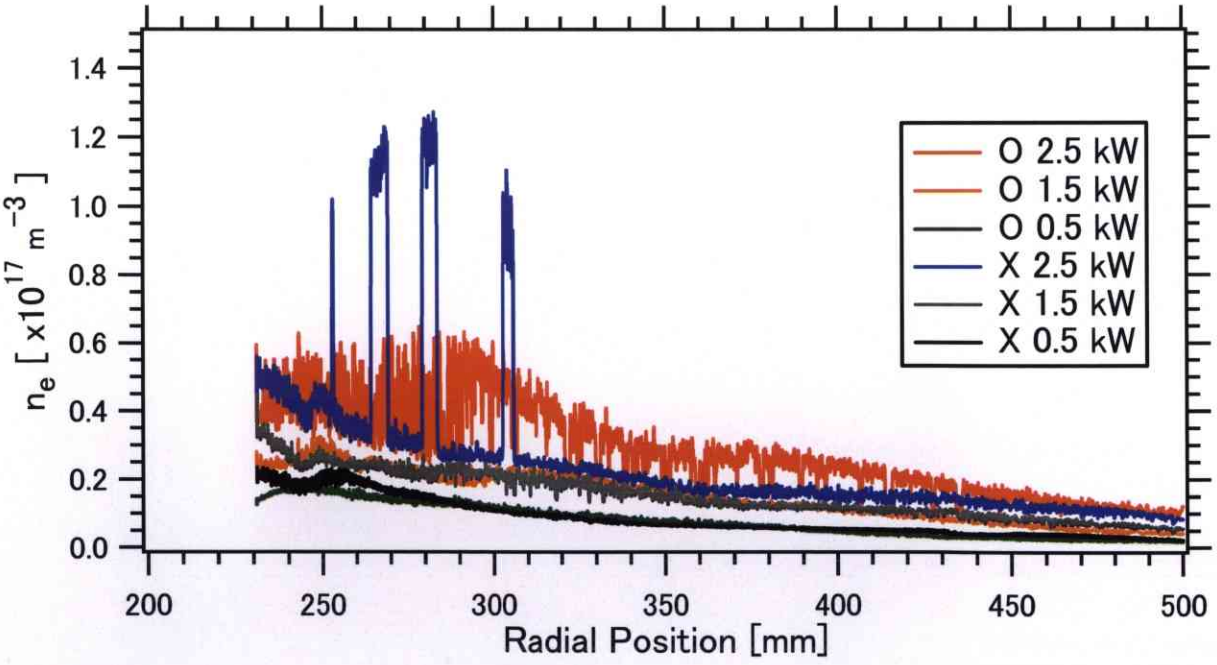

Figure 5.21: Injection mode dependence of an electron density profile with the simple dipole configuration.

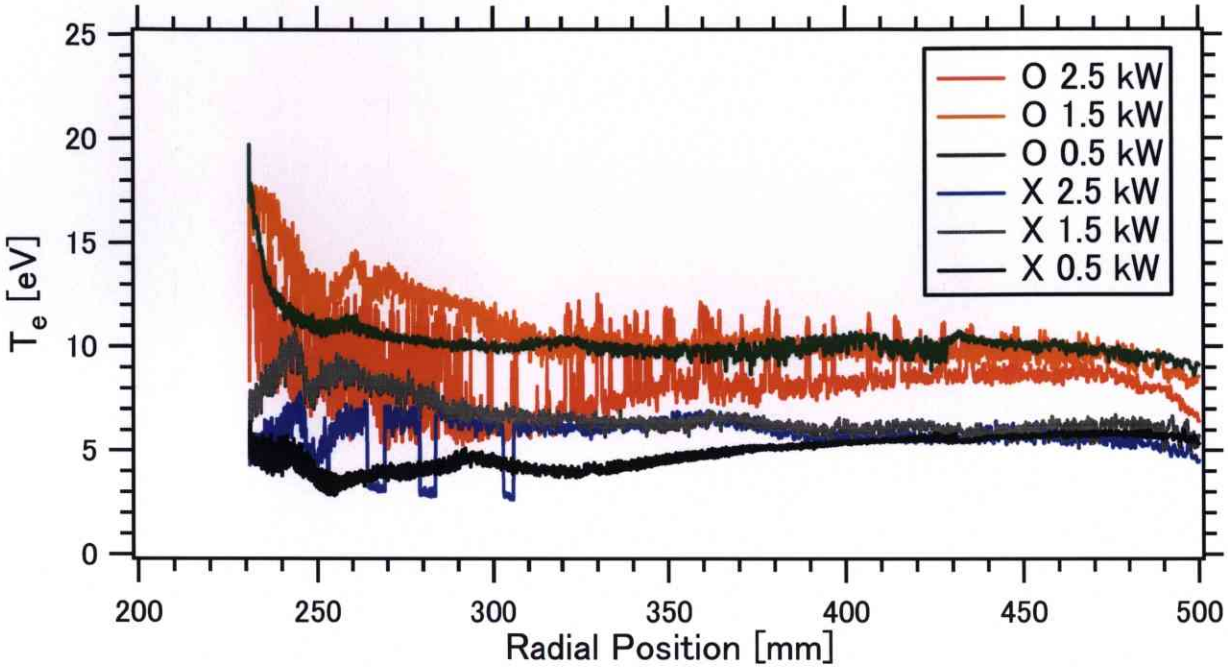

Figure 5.22: Injection mode dependence of a bulk electron temperature profile with the simple dipole configuration.

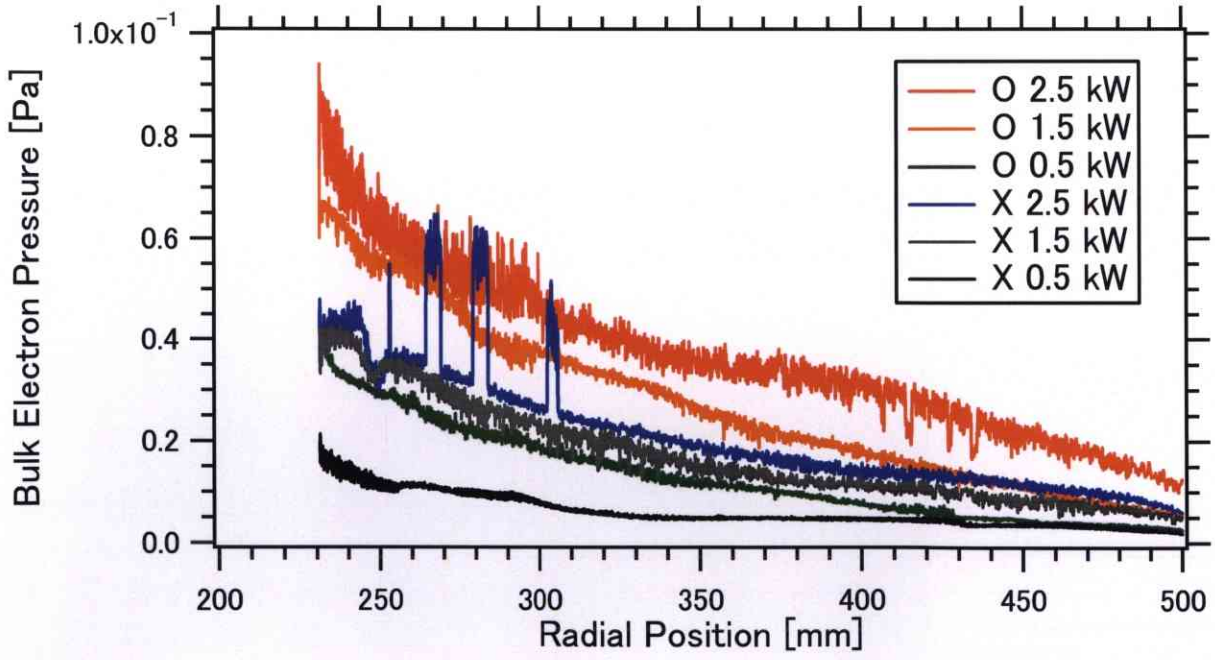

Figure 5.23: Injection mode dependence of a bulk electron pressure profile with the simple dipole configuration.

The one-path absorption can be evaluated by the optical thickness. The optical thicknesses of the electron cyclotron resonances for the ordinary and extraordinary wave which propagate perpendicular to the magnetic field are written as

$$\tau_n^O = \frac{\pi^2 n^{2(n-1)}}{2^{n-1}(n-1)!}\left(\frac{\omega_{pe}}{\Omega_e}\right)^2\left(\frac{\kappa T_e}{m_e c^2}\right)^n\left(1-\frac{\omega_{pe}^2}{n^2\Omega_e^2}\right)^{n-1/2}\frac{L_B}{\lambda_0} \quad (n \geq 1), \tag{5.3}$$

$$\tau_n^X = 5\sqrt{2}\pi^2\left(\frac{\omega_{pe}}{\Omega_e}\right)^2\left(\frac{\kappa T_e}{m_e c^2}\right)^2\left(1-\frac{\omega_{pe}^2}{2\Omega_e^2}\right)^{3/2}\frac{L_B}{\lambda_0} \quad (n = 1), \tag{5.4}$$

$$\tau_n^X = \frac{\pi^2 n^{2(n-1)}}{2^{n-1}(n-1)!}\left(\frac{\omega_{pe}}{\Omega_e}\right)^2\left(\frac{\kappa T_e}{m_e c^2}\right)^{n-1}\left(1-\frac{\omega_{pe}^2}{n^2\Omega_e^2}\right)^{n-1/2}\frac{L_B}{\lambda_0} \quad (n \geq 2), \tag{5.5}$$

where L_B and λ_0 denote the characteristic length of the magnetic field and wavelength in vacuum, respectively [8]. Table 5.1 shows the optical thickness of cold waves on a typical experiment in Mini-RT. In order to estimate the order of the optical thickness, we assumed electron density, electron temperature and the scale length of magnetic field are 5×10^{16} m^{-3}, 10 eV and 50 mm, respectively.

Table 5.1: Optical thickness of cold waves

	1st	2nd	3rd
O-mode	3×10^{-5}	3×10^{-9}	3×10^{-13}
X-mode	4×10^{-9}	2×10^{-5}	6×10^{-9}

If the one-path absorption rate is much less than unity, the O- and X-waves pass through a plasma, so that they are reflected at the wall of the vacuum vessel. As the result, the reflected wave may change its polarization. Therefore injected polarization no longer play an important role. In Mini-RT, the one-path absorption coefficient is quite small, so that the absorption of cold waves into bulk electrons do not gives a significant difference of a plasma characteristic.

5.2 Effects of Levitation of the Internal Coil

5.2.1 High Density (Overdense) Plasma Production

Figures 5.24 and 5.25 show the profiles of an electron density and an electron temperature for various experimental conditions, respectively. Note that the floating coil located at $z = 20$ mm when it was levitated (see Fig. 5.26), whereas it located on the mid-plane when it was supported. Peak electron densities more than doubly exceeded the cutoff density of the 2.45 GHz O-mode wave, i.e. $7.4 \times 10^{16}\mathrm{m}^{-3}$. Electron temperature profiles slightly greater than that of supported case.

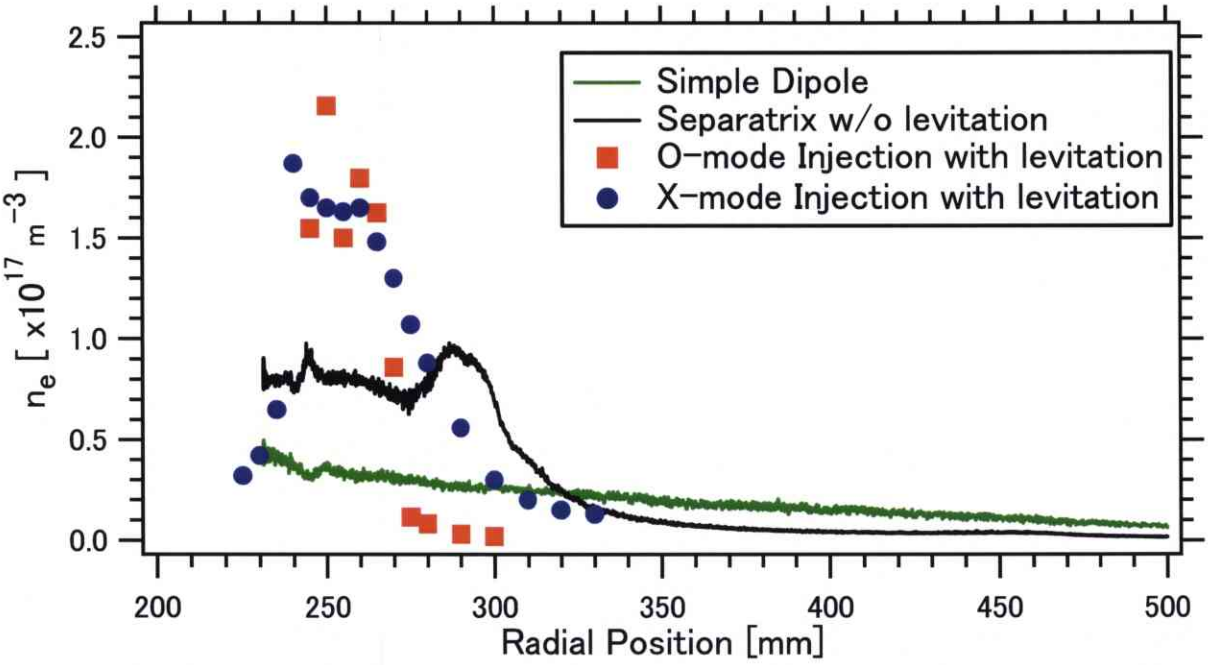

Figure 5.24: Comparison of electron density profiles when the internal coil is levitated and mechanically supported.

Figures 5.27 and 5.28 show the waveforms of decay of an electron density with the internal coil supported and levitated, respectively. Measurements were carried out by the 75GHz microwave interferometer. When the internal coil is supported, an electron density decays with an output of a microwave or faster. On the other hand, when the internal coil is levitated, an electron density decays with two time constants. One of these is comparable with time constant of microwave output and the other is approximately 300 ms. On the other hand, the longer time constant of microwave is approximately 200 ms. By estimating magnetic field strength $B \sim 0.05$ T, an electron temperature $T_e \sim 10$ eV and characteristic system size

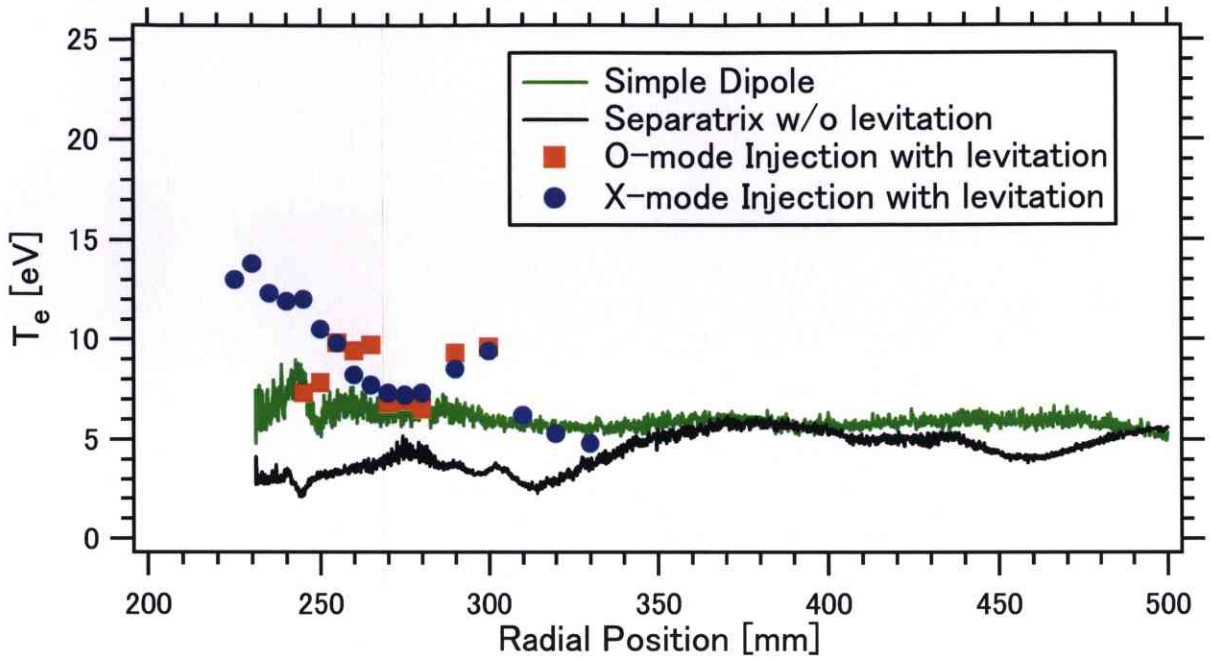

Figure 5.25: Comparison of electron temperature profiles when the internal coil is levitated and mechanically supported.

$L \sim 300$ mm, which corresponds to the distance between outer diameter of the internal coil and vacuum vessel, respectively, the Bohm diffusion time $\tau_B = \dfrac{L^2}{D_B} = \dfrac{16BL^2}{T_e}$ ~7.2 ms where T_e is in eV. When the internal coil is levitated, particle confinement time is sufficiently longer than the Bohm diffusion time.

5.2.2 The Plasma Production with Low Working Gas Pressure

The levitation of the internal coil enables one to product a plasma with a low filling gas pressure [22]. Figure 5.29 shows the working gas pressure dependence of electron density, which is measured by a double probe, at radial position $R = 240$ mm. When the floating coil is levitated, plasma production can be achieved under the 1×10^{-3} Pa of a filling gas pressure, whereas around 1×10^{-2} Pa is the threshold of a production of plasma when the floating coil is mechanically supported.

It is obvious that the mechanical support structure causes the plasma energy loss and prevents plasma production under the low filling gas conditions. Figure 5.30 shows the relationship between the levitation distance from the mechanical structure, i.e. gap means levitation distance. In this experiments, the vertical location of the internal coil is fixed, and mechanical structure is removed from a plasma. The averaged electron density increases with the removal

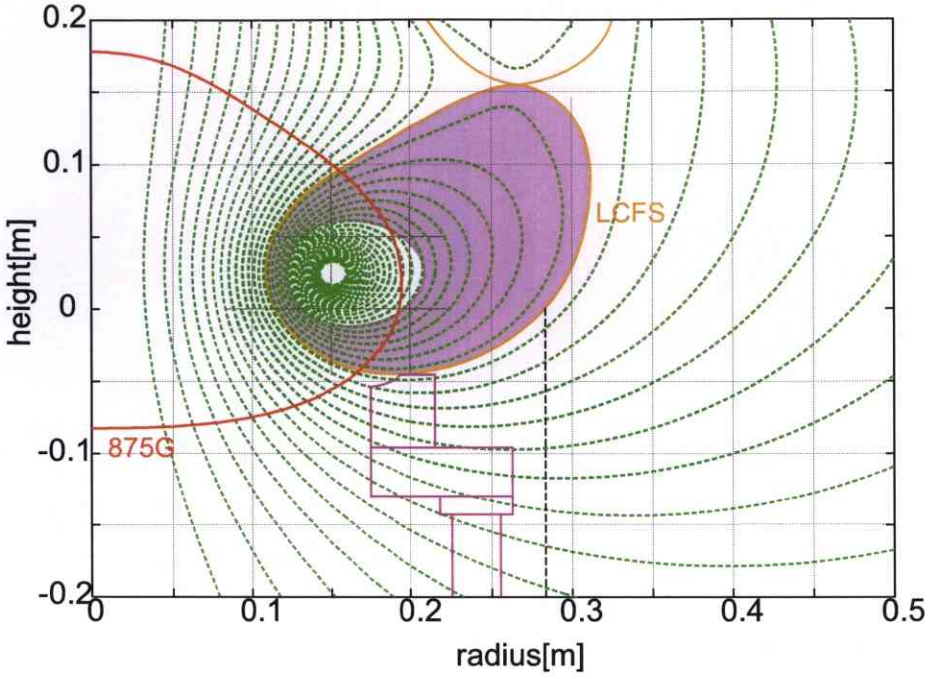

Figure 5.26: The calculated shape of the magnetic configuration and the separatrix in the experiment with the levitated internal coil.

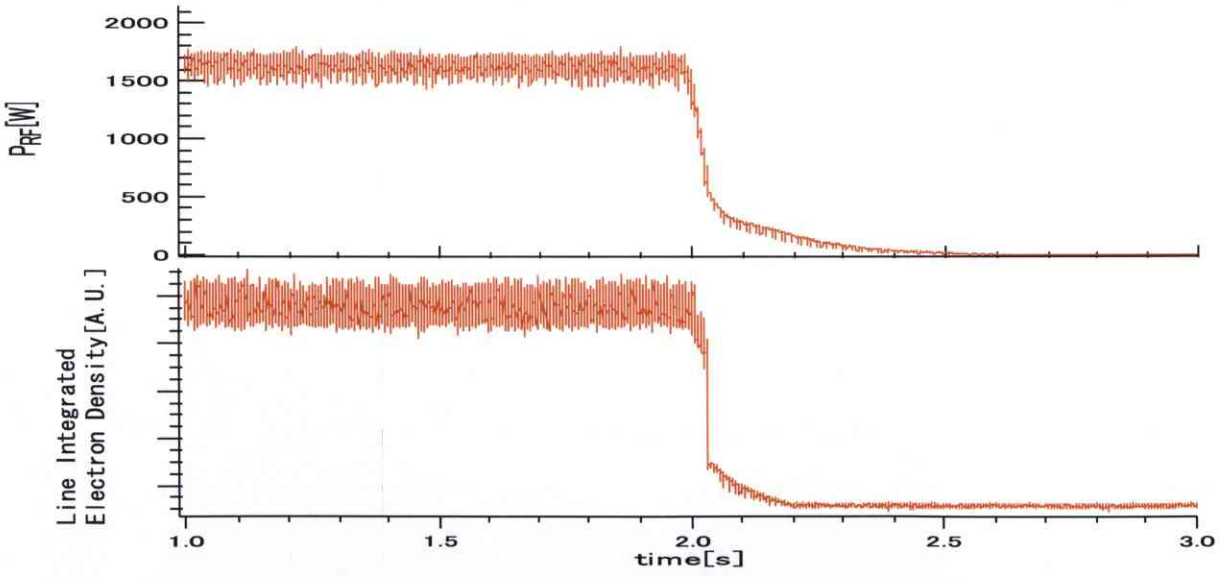

Figure 5.27: Decay of an electron density when the internal coil is supported.

of the mechanical structure. The 40 mm levitation corresponds to almost completely removal of the mechanical structure. A plasma cannot be produced when the gap is less than 15 mm under the working pressure of around 10^{-3} Pa.

Although it is not measured experimentally, the electric field in the Mini-RT device is

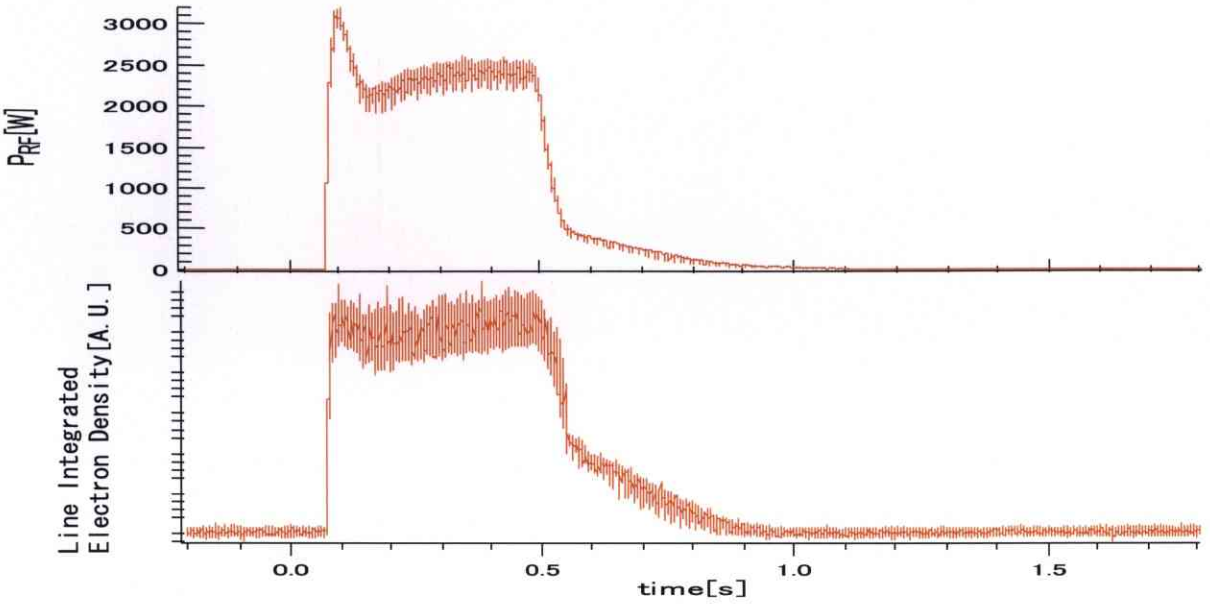

Figure 5.28: Decay of an electron density when the internal coil is levitated.

assumed to be negligible. So the velocity of a guiding center velocity is probably determined by the ∇B drift velocity

$$\mathbf{v}_{\nabla B} = \frac{W_\perp \mathbf{B} \times \nabla B}{qB^2} = \frac{\frac{1}{2} m {v_\perp}^2 \mathbf{B} \times \nabla B}{qB^2} \ . \tag{5.6}$$

If we assume $v_\perp \approx v_{th,e}$, the ∇B drift velocity can be written as

$$v_{\nabla B} = \frac{\frac{1}{2} m_e v_{th,e}^2}{eBL}, \tag{5.7}$$

where $v_{th,e}$ and L denote the electron thermal velocity and the characteristic length of the magnetic field strength, i.e. $L = \left| \frac{B}{\nabla B} \right|$, respectively.

The ionization cross-section of hydrogen by an electron σ_{en} is the function of the electron energy, and it has maximum for the electron of which temperature is around 100 eV [30] (see Fig.5.31). Now we consider the electron with the temperature of 100eV, which corresponds to the thermal velocity of $v_{th,e} = 7.26 \times 10^6$ m/sec. Since the magnetic field strength B and characteristic length L are 0.04 T and 0.1 m, respectively, the ∇B drift velocity of the electron is $v_{\nabla B} = 4 \times 10^4$ m/sec. The ionization cross-section by the electron σ_{en} with the energy of 100 eV is known to be 9×10^{-21} m^2 by experiments. So the collision time τ_{en} and mean free path $\lambda_{en} = v_{th,e} \tau_{en}$ of the electron in the H_2 gas of 4.0×10^{-2} Pa, which corresponds to the neutral density of 8×10^{18} m^{-3}, are 2×10^{-6} sec and 14 m, respectively. Since the number of

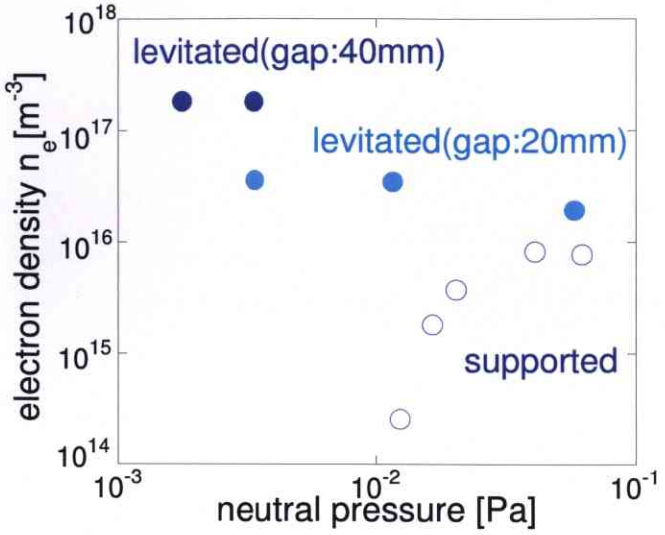

Figure 5.29: Working gas pressure dependence of electron density measured by double probe. Probe position is R=0.24m.

the support structure is three and they locate equiangular on the radius of $R = 0.25$ m, the maximum distance between them is $2 \times 0.25\pi/3 = 0.42$ m (see Fig. 5.32). Then the time within which the electron hit to the support structure by ∇B drift is 2×10^{-5} sec at maximum. Since it is assumed the parallel component of the electron velocity $v_{//}$ is almost equal to the thermal velocity, the electron moves 140 m before hitting to the support structure. Therefore, the electron collides averagely with 10 neutral gas molecules and ionizes them before it collides with the support structure and is lost. If the neutral gas pressure becomes less than 4×10^{-3} Pa, the electron is lost before it ionize neutral gas molecules, which means the disability of plasma production. This value agrees in the order with the experimental results; however, note that this model is quite qualitative hypothesis.

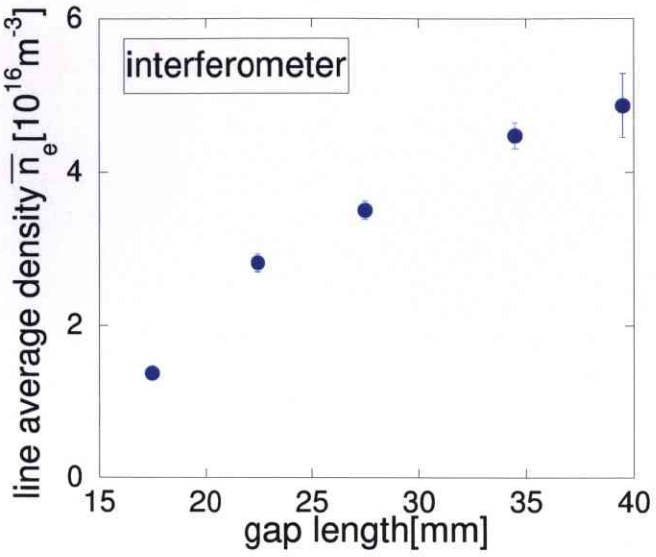

Figure 5.30: Variation of line-averaged electron density for several gap length between floating internal coil and support structure.

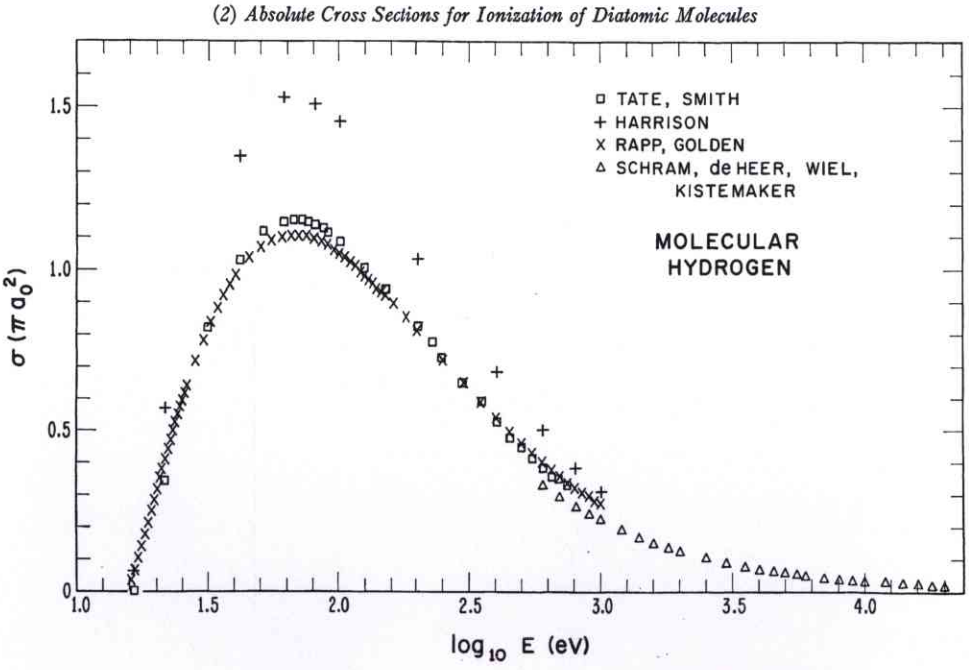

Figure 5.31: Total cross sections for the ionization of molecular hydrogen [30]. The cross-section of the vertical axis is normalized by $\pi {a_0}^2 (= 8.797 \times 10^{-21} \mathrm{m}^2)$, where a_0 is Bohr radius.

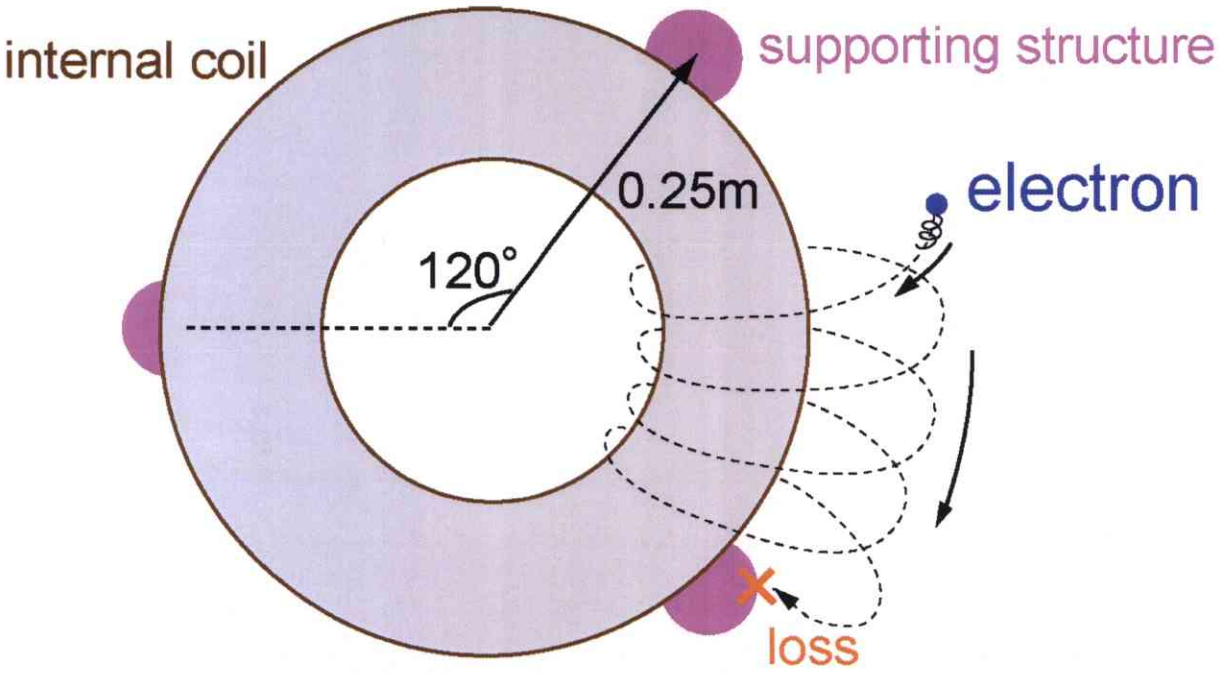

Figure 5.32: Electrons hit to support structure owing to the ∇ B drift.